

**Measurement of the Relative
Branching Ratio of $D^+ \rightarrow \pi^- \pi^+ \pi^+$
to $D^+ \rightarrow K^- \pi^+ \pi^+$**

A Dissertation

Presented to

The Faculty of the Graduate School of Arts and Sciences

Brandeis University

Department of Physics

Professor Craig Blocker, Advisor

In Partial Fulfillment

of the Requirements for the Degree

Doctor of Philosophy

by

Nataša Kravchenko

May, 2008

This dissertation, directed and approved by Nataša Kravchenko's committee, has been accepted and approved by the Graduate Faculty of Brandeis University in partial fulfillment of the requirements for the degree of:

DOCTOR OF PHILOSOPHY

Professor Adam B. Jaffe, Dean of Arts and Sciences

Dissertation Committee:

Professor Craig Blocker, Chair

Professor Albion Lawrence

Professor Stéphane Willocq

©Copyright by
Nataša Kravchenko
2008

Abstract

Measurement of the Relative Branching Ratio of $D^+ \rightarrow \pi^- \pi^+ \pi^+$ to $D^+ \rightarrow K^- \pi^+ \pi^+$

A dissertation presented to the Faculty of
the Graduate School of Arts and Sciences of
Brandeis University, Waltham, Massachusetts

by Nataša Kravchenko

We present a measurement of the relative branching ratio of the Cabibbo-suppressed D^+ meson decay into three charged pions using 193 pb^{-1} of data collected by CDF II detector at Fermilab's Tevatron. We determine $BR(D^+ \rightarrow \pi^- \pi^+ \pi^+)/BR(D^+ \rightarrow K^- \pi^+ \pi^+) = (3.461 \pm 0.038(stat) \pm 0.040(syst))\%$. This value agrees with the present world average and is about three times more precise than any current measurement. Using the world average branching ratio $BR(D^+ \rightarrow K^- \pi^+ \pi^+) = (9.51 \pm 0.34)\%$, we find $BR(D^+ \rightarrow \pi^- \pi^+ \pi^+) = (3.29 \pm 0.11) \times 10^{-3}$.

Contents

Abstract	iv
1 Introduction	1
1.1 The Focus of This Measurement	4
1.2 Charm Measurements - Past and Present	7
1.3 Charm at the Collider Detector at Fermilab	9
2 Theoretical Background	11
2.1 Standard Model: A Brief Summary	11
2.2 Flavor Changing Interactions	14
2.3 Dalitz Structure of Three Body Decays	18
3 Experimental Apparatus	23
3.1 Tevatron - The Source of $p\bar{p}$ Collisions	23
3.2 CDF II Detector	29
3.3 Trigger System	51
3.4 Detector Operation and Off-line Data Processing	62
4 Overview of the Measurement	64
4.1 General Issues of Data Analysis	64
4.2 Roadmap for This Analysis	66
5 Data Samples	72
5.1 Data Sample	72
6 Monte Carlo Samples	80
6.1 Monte Carlo Samples	81
6.2 Dalitz Structure of the Signal Modes	86
7 Event Selection and Candidate Reconstruction	92
7.1 Track Preparation	93
7.2 Track matching to SVT	95

CONTENTS

7.3	Trigger Confirmation	97
7.4	Candidate Reconstruction	98
7.5	Optimization of Selection Requirements	99
8	Yields Analysis	111
8.1	General Fit Model	111
8.2	Reflections Fits	111
8.3	Signal Shape	118
8.4	Data Fit	122
8.5	Systematic Uncertainties	124
9	Relative Efficiencies	133
9.1	Trigger Prescale Factors	134
9.2	Dalitz Structure	136
9.3	XFT efficiencies	137
9.4	D^+ Lifetime Correction	143
9.5	$P_T(D^+)$ Spectrum Correction	144
9.6	Systematic Uncertainties of Relative Efficiency	145
10	Result and Conclusions	159

List of Tables

3.1	Tevatron system Run II parameters.	29
3.2	Basic parameters of the CDF II calorimetry.	47
3.3	Design parameters of the CDF muon system. Numbers of pion interaction lengths and multiple scattering resolution are given for reference angles: $\theta=90^\circ$ for CMU and CMP/CSP, and $\theta=55^\circ$ for CMX/CSX.	51
5.1	Discrete data periods and corresponding luminosities, as defined by detector and trigger configuration changes. The luminosity is approximate, calculated with the good run script.	75
5.2	Definition of the trigger requirements applied to three different versions of the B_CHARM trigger. The column 'Level' indicates the trigger level at which this requirement is applied for the first time. In general, trigger requirements at Level 1 and Level 2 are repeated at higher trigger levels with the same values. An exception is made for the requirement on the impact parameter, which is looser at Level 3 than at Level 2.	78
6.1	Monte Carlo samples used for this analysis. For the excited charm states the decays are forced to have a charged pion, but the charm states themselves are decayed inclusively.	85
7.1	Summary of selection criteria for $D^+ \rightarrow \pi^- \pi^+ \pi^+$ and $D^+ \rightarrow K^- \pi^+ \pi^+$ decays. The "Loose" requirements are used for efficiency studies, and are meaningful only for $K\pi\pi$ channel; for $\pi\pi\pi$ they allow too much background. The tight criteria are used for signal extraction.	108
8.1	Fit parameters from the signal shape template, for $D^+ \rightarrow \pi^- \pi^+ \pi^+$, $D^+ \rightarrow K^- \pi^+ \pi^+$ and $D_s \rightarrow \pi^- \pi^+ \pi^+$ decays.	122
8.2	Fit parameters for the signal peaks, $D^+ \rightarrow \pi^- \pi^+ \pi^+$ and $D^+ \rightarrow K^- \pi^+ \pi^+$ decays. The errors are statistical. The numbers that are left out are fixed from Monte Carlo; see Table 8.1.	123
8.3	Systematic uncertainties associated with fixing and releasing $D^+ \rightarrow K^- \pi^+ \pi^+$ signal $\frac{\sigma_W}{\sigma_N}$ and f_w	125

LIST OF TABLES

8.4	Systematic uncertainties associated with the size of the signal peaks' radiative tails.	126
9.1	Prescale factors for the two prescaled triggers, averaged over time for each of the data-taking time periods. The first two periods are trivial because there was only one BCHARM trigger employed at the time, and it was not prescaled.	135
9.2	Relative efficiencies before and after Dalitz reweighting, sorted by the trigger sample.	137
9.3	Absolute efficiency of the $\pi\pi\pi$ channel before and after Dalitz reweighting, sorted by the trigger sample.	137
9.4	Absolute efficiency of the $K\pi\pi$ channel before and after Dalitz reweighting, sorted by the trigger sample.	139
9.5	Systematic uncertainty assigned to $D^+ \rightarrow \pi^-\pi^+\pi^+$ Dalitz structure modeling.	146
9.6	Systematic uncertainty assigned to $D^+ \rightarrow K^-\pi^+\pi^+$ Dalitz structure modeling.	149
9.7	Systematic uncertainty associated with correcting XFT efficiencies of tracks: sideband subtraction is performed using left or right sideband, not both as in the rest of the analysis.	150
9.8	Systematic uncertainty associated with the choice of procedure for correcting XFT efficiencies of tracks.	151
9.9	Systematic uncertainty associated with the different Monte Carlo $p_T(D)$ spectra corrections.	151
9.10	Systematic uncertainty associated with the uncertainty on D^+ lifetime	153
9.11	Probability of charm daughters to undergo hadronic interactions inside the tracking volume (first three rows) and efficiency for not having any of the three daughters interact (last two rows)	157
9.12	Summary of the relative systematic uncertainties.	158

List of Figures

2.1	Feynman diagram for mixing of D^0 mesons.	16
2.2	Cabibbo suppressed tree (left) and penguin (right) diagrams of the $D^+ \rightarrow \pi^- \pi^+ \pi^+$ decay.	18
2.3	Dalitz plots of our $D^+ \rightarrow \pi^- \pi^+ \pi^+$ (left) and $D^+ \rightarrow K^- \pi^+ \pi^+$ (right) decays. The high mass corners and the low mass band are cut off due to kinematic constraints to suppress background.	20
3.1	Diagram of the Tevatron accelerator complex.	28
3.2	A 3D drawing of the CDF II detector with primary subsystems indicated.	32
3.3	The $r - Z$ view of the CDF II detector illustrating pseudo-rapidity coverage of the tracking system.	33
3.4	The transverse view of several cells from the superlayer 2 of the COT. The arrow shows the radial direction.	38
3.5	The design and coverage of the silicon subdetectors SVX, ISL and L00 in $r - z$ projection. The z coordinate is compressed.	42
3.6	The $r - \phi$ view of the CDF silicon detectors, including SVX bulkhead and ISL support structure.	43
3.7	Block diagram of the CDF trigger system.	53
3.8	EXtra Fast Tracker functional diagram.	58
3.9	Block diagram of the SVT trigger.	60
3.10	Distribution of impact parameters for SVT tracks and tracks produced by offline reconstruction for charged particles with $p_T > 2 \text{ GeV}/c$	61
6.1	Dalitz plots of the $D^+ \rightarrow K^- \pi^+ \pi^+$ decay made with our data (top left); Monte Carlo (top right) is generated flat and reweighted using E791 resonances fitted to the data. The agreement between data (points with error bars) and Monte Carlo (histogram) after reweighting can be seen on the plots of the low and high invariant masses, on the bottom.	88

LIST OF FIGURES

6.2	Dalitz plots of the $D^+ \rightarrow \pi^- \pi^+ \pi^+$ decay: data(top left) and Monte Carlo (top right). Monte Carlo is generated flat and reweighted using E791 resonances fitted to our data. Plots of the low (bottom left) and high (bottom right) invariant masses show the agreement between data (points with error bars) and Monte Carlo (histogram) after reweighting. The high mass corners are cut off due to a kinematic constraint to suppress background, introduced in next Chapter. Similarly, the low mass band cut-out is due to a constraint to suppress K_S two-body decays.	89
6.3	Comparison of the low-mass(left) and high-mass(right) combination in $D^+ \rightarrow K^- \pi^+ \pi^+$ decays between E791 model A (top), model B (middle) and model C (bottom), as compared with our data (points with error bars).	90
6.4	Comparison of the low-mass(left) and high-mass(right) combination in $D^+ \rightarrow \pi^- \pi^+ \pi^+$ decays between E791 model 1 (top) and model 2 (bottom), as compared with our data (points with error bars).	91
7.1	Mass spectra of $D^+ \rightarrow K^- \pi^+ \pi^+$ (left) and $D^+ \rightarrow \pi^- \pi^+ \pi^+$ (right) decays, made with loose set of selection requirements used in studies.	100
7.2	Data - Monte Carlo comparison of six kinematic variables, used for extracting the $D^+ \rightarrow K^- \pi^+ \pi^+$ signal. Dots with (tiny) error bars are data points, and histogram represents Monte Carlo.	103
7.3	Data - Monte Carlo comparison of six kinematic variables, used for extracting the $D^+ \rightarrow \pi^- \pi^+ \pi^+$ signal. Dots with error bars are data points, histogram represents Monte Carlo.	104
7.4	Cut-scan of the significance (black line) with respect to selection criteria values, for $D^+ \rightarrow \pi^- \pi^+ \pi^+$ decay. The signal yields, blue, are taken from the Monte Carlo, the background (red) from sidebands of the data.	106
7.5	Mass spectrum of $D^+ \rightarrow K^- \pi^+ \pi^+$ decay (above) and $D^+ \rightarrow \pi^- \pi^+ \pi^+$ decay (below), obtained with the $\pi\pi\pi$ -optimized tracks.	107
7.6	$D^+ \rightarrow \pi^- \pi^+ \pi^+$ mass, with $ct \geq 250 \mu\text{m}$; the wide structure under the D_s^+ peak is diminished when the requirement is tightened to $350 \mu\text{m}$.	109
8.1	Reflections from inclusive D^+ and D_s^+ decays, reconstructed as $D^+ \rightarrow K^- \pi^+ \pi^+$ (left) and $D^+ \rightarrow \pi^- \pi^+ \pi^+$ (right), after applying the signal extraction requirements.	113
8.2	Reflections from inclusive D^* decays, reconstructed as $D^+ \rightarrow K^- \pi^+ \pi^+$ (left) and $D^+ \rightarrow \pi^- \pi^+ \pi^+$ (right), after applying the signal extraction requirements.	114
8.3	Individually fitted reflections contributing to $D^+ \rightarrow K^- \pi^+ \pi^+$ background. <i>Continued on next page</i>	115

LIST OF FIGURES

8.4	Individually fitted reflections contributing to $D^+ \rightarrow K^-\pi^+\pi^+$ background, from D^+ and D_s^+ decays. Contributions from decays that are not shown are negligible.	116
8.5	Individually fitted reflections contributing to $D^+ \rightarrow \pi^-\pi^+\pi^+$ background, from D^+ and D_s^+ decays. Contributions that are not shown are negligible.	117
8.6	Signal shapes: $D^+ \rightarrow K^-\pi^+\pi^+$ (top) and $D^+ \rightarrow \pi^-\pi^+\pi^+$ (bottom).	120
8.7	$D_s \rightarrow \pi^-\pi^+\pi^+$ peak fit template.	121
8.8	$D^+ \rightarrow K^-\pi^+\pi^+$ data fit.	127
8.9	$D^+ \rightarrow \pi^-\pi^+\pi^+$ data fit.	128
8.10	Residuals of the $D^+ \rightarrow K^-\pi^+\pi^+$ data fit. No systematic trends are observed, and the largest residuals tend to occur in the regions far from the signal peak.	129
8.11	Residuals of the $D^+ \rightarrow \pi^-\pi^+\pi^+$ data fit. No systematic trends are observed, and the largest residuals tend to occur in the regions far from the signal peak.	130
8.12	$D^+ \rightarrow K^-\pi^+\pi^+$ data fit, with reflections contributions emphasized. All the contributions add up to form the area under the topmost green line.	131
8.13	$D^+ \rightarrow \pi^-\pi^+\pi^+$ data fit, with reflections contributions emphasized. All the contributions add up to form the area under the topmost red line.	132
9.1	Trigger sculpting of the Dalitz space, $\pi\pi\pi$ on top and $K\pi\pi$ on bottom, for the opposite charge BCHARM_HIGHPT trigger (left side) and for BCHARM_LOWPT trigger (right side). The Monte Carlo used here is uniformly distributed over the phase space, but the triggers have different acceptance rate for different regions of the phase space.	138
9.2	XFT efficiency dependence on the track variables p_T , ϕ_0 and $\cot(\theta)$, for kaons (red) and pions (blue), recorded during data-taking period 7. Data plots are on the left and Monte Carlo on the right.	140
9.3	XFT efficiency dependence on $E_{loss} = \ln(p/m)/\sin(\theta)$ variable, for kaons (red) and pions (blue), periods 3 to 7.	141
9.4	Data - Monte Carlo comparison of transverse momentum of the D^+ in $K^-\pi^+\pi^+$ (left) and $\pi^-\pi^+\pi^+$ (right) decays. Plots indicate that, even after the correction, Monte Carlo deviates from data by being generally shifted toward lower p_T values.	145
9.5	Ratio of data and Monte Carlo p_T spectra of the D meson, as derived from $D^+ \rightarrow K^-\pi^+\pi^+$ decay, and fitted to an exponential plus a first order polynomial.	146

LIST OF FIGURES

9.6	Invariant mass projections of Dalitz plots of the $D^+ \rightarrow \pi^- \pi^+ \pi^+$ decay for central value (top) and the assigned systematic uncertainty (bottom). Shown is the agreement between data and Monte Carlo. The latter is generated flat and reweighted using E791 resonances fitted to the data.	147
9.7	Invariant mass projections of Dalitz plots of the $D^+ \rightarrow K^- \pi^+ \pi^+$ decay for central value (top) and the assigned systematic uncertainty (bottom). Shown is the agreement between data and Monte Carlo. The latter is generated flat and reweighted using E791 resonances fitted to the data.	148
9.8	Pion and kaon XFT efficiency fitted as a function of p_T^{-1} (only period 7 shown; other periods are similar), as an estimate of systematic uncertainty of Monte Carlo XFT efficiency reweighting.	150
9.9	Data - Monte Carlo comparison of transverse momentum of the D^+ in $K^- \pi^+ \pi^+$ (left) and $\pi^- \pi^+ \pi^+$ (right) decays, after applying the $\pi\pi\pi$ -derived correction to estimate the systematic uncertainty.	152
9.10	Ratio of data and Monte Carlo p_T spectra of the D meson, as derived from $D^+ \rightarrow \pi^- \pi^+ \pi^+$ decay, and fitted to an exponential plus a first order polynomial. This is then used to assign an uncertainty.	152
9.11	Overlay of data and Monte Carlo p_T spectra of the D^+ daughter tracks. $D^+ \rightarrow K^- \pi^+ \pi^+$ plots are on the left and $D^+ \rightarrow \pi^- \pi^+ \pi^+$ on the right. Track 1 corresponds to the track of the charge opposite to that of the D^+ meson. Track 2 and 3 are ordered such that $m_{12} > m_{13}$	155
9.12	Hadronic interaction probabilities using simulated single particle events.	156
10.1	PDG plot comparing measurements of $\frac{BR(D^+ \rightarrow \pi^- \pi^+ \pi^+)}{BR(D^+ \rightarrow K^- \pi^+ \pi^+)}$ performed by several collaborations.	160

Chapter 1

Introduction

This dissertation presents another brush stroke in painting the picture of the elementary constituents of the universe. The current working model of the elementary particles and their electromagnetic, weak, and strong interactions, known as the standard model, is remarkably effective in describing the experimental data on fundamental constituents of matter. In the theory, matter is composed of fundamental fermion (spin- $\frac{1}{2}$) particles, quarks and leptons. These building blocks interact by exchanging bosons, the integral spin particles.

The standard model arranges the quarks and leptons in three generations in order of increasing mass. Within each generation of quarks there is one “up-type” quark with the electric charge $+\frac{2}{3}e$, where e is the charge of the proton, and one “down-type” quark with the electric charge $-\frac{1}{3}e$. The three up-type quarks are called up, charm, and top and are denoted u , c and t . The down-type quarks are down, strange and bottom denoted d , s and b . Similarly, each of the lepton generations contains an electrically charged lepton and the corresponding neutral neutrino. The leptons are called electron, muon and tau and are denoted e , μ and τ ; neutrinos are named by

CHAPTER 1. INTRODUCTION

the charged lepton of their generation: ν_e , ν_μ and ν_τ .

This grouping by families of the fundamental fermions can be denoted in the following commonly accepted way:

$$\text{Quarks:} \quad \begin{pmatrix} u \\ d \end{pmatrix} \begin{pmatrix} c \\ s \end{pmatrix} \begin{pmatrix} t \\ b \end{pmatrix}$$

$$\text{Leptons:} \quad \begin{pmatrix} e \\ \nu_e \end{pmatrix} \begin{pmatrix} \mu \\ \nu_\mu \end{pmatrix} \begin{pmatrix} \tau \\ \nu_\tau \end{pmatrix}$$

For each of the fermions there exists an anti-fermion that has opposite value of all its charges (electric charge, color, and flavor). The masses of quarks, leptons, and gauge bosons are free parameters of the model, which is a major shortcoming of the theory.

Fermions can interact through four types of interactions: gravity, electromagnetism, weak, and strong interactions. Gravity is by far the weakest of the forces and has negligible effect on elementary particles. It is therefore ignored in experimental high energy physics, and is not mentioned in the standard model. Electromagnetic interactions, long-ranged and responsible for most extranuclear phenomena, are mediated by massless photons. Strong and weak interactions have very short ranges, acting at the sub-nuclear scales under one fermi (10^{-15} m). The weak interactions are mediated by the massive W^\pm and Z bosons and the strong by massless gluons.

Exchanges of photons, that is, electromagnetic interactions, take place only between electrically charged particles, whereas any fermion can engage in weak interaction by exchanging one of the heavy vector bosons. In the framework of the standard

model, electromagnetic and weak interactions acquired a unified description of the single “electroweak” interaction. The theory of strong interactions is called quantum chromodynamics. All quarks, but not leptons, are subject to the strong force, which is mediated by massless gluons that carry color charge. Quantum chromodynamics is based on principles similar to the electroweak theory, but the fact that the strength of the strong interaction depends on the scale of the interaction introduces complexities in the formalism. Perturbation theory is often not applicable, and as a result the numerical calculations of strong processes are extremely difficult.

One of the most interesting problems of the standard model, and one tied to the motivation for this measurement, is the problem of CP symmetry violation. If a system is invariant with respect to the charge conjugation (C) and parity (P) transformations applied in succession, the system possesses CP-symmetry. CP is an exact symmetry of gravitational, electromagnetic, and strong interactions, though not of weak interaction. It is often assumed in cosmology that the universe started with equal amount of matter and antimatter. However, all available experimental data point to this no longer being the case. Matter dominates, and little of anti-matter is found. For our world to exist as it is, having started as symmetric, significant CP-violating effects have to be at play [1]. The standard model does incorporate CP-violating processes naturally; these happen during quark-quark transitions between members of different quark generations. It is believed that the amount of CP-violation predicted by the standard model is not sufficient to explain the observed asymmetry of matter and anti-matter, and other, as yet undiscovered effects may be at play.

While the standard model has been remarkably successful in describing and predicting experimental observations to date, a number of its properties lead us to believe that there are physics laws which are still outside of the scope of our knowledge. One

of the main deficiencies of the standard model is its lack of parsimony. The theory is based on gauge symmetry, but has a large number of free parameters that are not explained within its framework. Such are, as mentioned above, the masses of all elementary fermions. The lack of appropriate model of unification of the electroweak and the strong interactions, and also lack of a model for gravity, add to the expectation that there must be physics phenomena beyond those described by the standard model. These new physics phenomena, to be described one day by a better theory, are commonly referred to as new physics. Experimental high energy physics today is primarily focused on measuring parameters of the standard model and probing for inconsistencies among them that might point to the new physics. The measurement presented in this dissertation is part of this trend.

1.1 The Focus of This Measurement

We study the decays of the D^+ meson. Like all mesons, D^+ is a bound state of a quark and an antiquark, in this case a charm quark (c) and a down antiquark (\bar{d}), in short, $c\bar{d}$. Similarly, D_s is a bound state of a charm quark (c) and a strange antiquark (\bar{s}), D^{*+} is an excited D^+ state, ($c\bar{d}$), and D^{*0} is an excited D^0 state, ($c\bar{u}$).

Here and throughout this dissertation, the charge conjugate states and decays are implicitly included. For example, $D^+ \rightarrow \pi^- \pi^+ \pi^+$ refers to both $D^+ \rightarrow \pi^- \pi^+ \pi^+$ and $D^- \rightarrow \pi^+ \pi^- \pi^-$. We consistently order the D^+ daughter particles so that the first daughter is the one with charge opposite to the D^+ meson. This convention enables us to omit the charges of D meson daughters; we do this often to simplify the text.

We measure the rate of D^+ meson decay into three charged pions ($D^+ \rightarrow \pi^- \pi^+ \pi^+$), relative to the rate of the D^+ decay into two charged pions and an oppositely charged

kaon. The $D^+ \rightarrow \pi^- \pi^+ \pi^+$ decay occurs relatively infrequently. Experimental data are limited regarding the rate of this decay, the intermediate resonant structure, and other properties including, for example, CP violation in this decay. Measuring the $D^+ \rightarrow \pi^- \pi^+ \pi^+$ decay rate by itself necessitates high-precision measurements of many parameters that are difficult to extract, such as the total number of D^+ mesons produced in $p\bar{p}$ collisions (called production cross section), or the absolute probability for recording and reconstructing these decays (acceptance rate and reconstruction efficiency). To avoid these complications, we measure the rate of this decay relative to the rate of another D^+ decay, into a topologically similar and much more probable final state: $D^+ \rightarrow K^- \pi^+ \pi^+$; this relative decay rate is called relative branching ratio. In order to measure the ratio it is not necessary to know the total amount of data in our sample and the total number of D^+ mesons produced. Furthermore, many systematic biases affect $D^+ \rightarrow \pi^- \pi^+ \pi^+$ and $D^+ \rightarrow K^- \pi^+ \pi^+$ in the same manner. They can be ignored when measuring relative branching fraction, as they cancel each other in the ratio. Finally, because the rate of the $D^+ \rightarrow K^- \pi^+ \pi^+$ decay can be well measured due to its abundance, the precision of this measurement of the branching ratio is higher than it would be in a stand-alone measurement of the $D^+ \rightarrow \pi^- \pi^+ \pi^+$ rate after all systematic uncertainties and biases are accounted for.

We determine the branching ratio of the two modes as follows:

$$\frac{BR(D^+ \rightarrow \pi^- \pi^+ \pi^+)}{BR(D^+ \rightarrow K^- \pi^+ \pi^+)} = \frac{N_{\pi^- \pi^+ \pi^+}}{N_{K^- \pi^+ \pi^+}} \cdot \frac{\varepsilon(K^- \pi^+ \pi^+)}{\varepsilon(\pi^- \pi^+ \pi^+)}. \quad (1.1)$$

The ingredients of the formula above include the yields and the efficiencies. The yields $N_{\pi^- \pi^+ \pi^+}$ and $N_{K^- \pi^+ \pi^+}$ are the numbers of D^+ mesons reconstructed in our sample for the $\pi^- \pi^+ \pi^+$ and $K^- \pi^+ \pi^+$ decay channels respectively. We measure

them by analyzing the invariant mass spectra of the D^+ candidates. The efficiencies $\varepsilon(\pi^-\pi^+\pi^+)$ and $\varepsilon(K^-\pi^+\pi^+)$ reflect the probability to record an event with the desired D^+ decay in a $p\bar{p}$ collision as well as to select it from the multitude of others in the data sample and reconstruct the D^+ candidate in it. These efficiencies are primarily determined from Monte Carlo simulation. We only need a relative efficiency of the two.

The decay $D^+ \rightarrow \pi^-\pi^+\pi^+$ involves charm to down quark ($c \rightarrow d$) transition. This decay at the tree level is simple and straightforward to calculate. It is not expected to violate the CP symmetry. However, subtle effects may be introduced by higher-order diagrams and the strong interactions in the final state. This may result in the decay violating the CP symmetry. The CP violation would be of interest as no CP asymmetry has been found so far in charm decays.

This branching ratio measurement is a technical prerequisite for the measurement of the CP asymmetry in the $D^+ \rightarrow \pi^-\pi^+\pi^+$ decay. It develops the tools and points to the major effects to be taken into account. By looking at the resonant substructure of the decay, we open the door to the measurement of CP violation in the individual resonant modes. This is important, because CP violation could take place in individual resonant modes, yet even substantial effects may wash out in the sum of all modes that lead to the same final state, giving the zero net asymmetry. The standard model does predict a small non-zero CP violation in charm decays. A substantial CP asymmetry would signal the presence of new physics.

1.2 Charm Measurements - Past and Present

The existence of the charm quark was predicted before its discovery, as were its basic properties, such as the abundance of kaons in the decay final state and small but finite lifetime. A candidate event for the decay of charm was first seen in 1971 in an emulsion exposed to cosmic rays [2]. The new quark was not widely accepted until the 1974 discovery of the J/ψ [3, 4], a $c\bar{c}$ bound state.

The discovery of the charm quark has completed the picture of the two generations of the fundamental constituents of matter, adding to the u , d and s quarks as well as all leptons of the first two generations already known. The existence of the fourth quark brought numerous predictions that were followed by discoveries of new baryons (such as Λ_c consisting of (udc)) and mesons (such as D^+ made of $(c\bar{d})$). Such a neat picture with two generations of quarks and leptons and abundance of confirmed predictions was instrumental in convincing physicists of the validity of the quark model and served as the predecessor of the standard model that came into being years later.

The first experimental evidence of weakly decaying charm was obtained in photographic emulsion. At the time, only this technique had good enough spatial resolution (about 1 micron) to detect particles with lifetimes as short as 10^{-13} s. Charm discovery prompted a development in detectors, most importantly the microvertex detectors. These were a giant step forward in both bottom and charm physics: they were essential in the discovery of top quark through b -flavor tagging and may prove important for the discovery of the Higgs. Indeed, the replacement of emulsions and bubble chambers with electronic imaging devices represented a major transition for particle physics, from relying on imaging to conduct measurements, to using more

complex methods [5]. The measurement presented here, performed with the Collider Detector at Fermilab (described in Section 3), relies heavily on its silicon microstrip detector.

Properties of charm mesons and baryons and their decays have been studied extensively at e^+e^- and $p\bar{p}$ colliders and other high energy physics experiments. As technology opens new possibilities for experiment - particle detectors become capable of resolving finer and finer details, number of recorded events grows by orders of magnitude, trigger capabilities allow collection of specific data of interest and therefore significant reduction of backgrounds - formerly inaccessible interesting and rare processes come within experimental reach. At present, studies of charm are conducted both within and beyond the standard model framework. They provide useful insights for measurements of the bottom quark properties and have the potential to reveal new physics on their own.

One of the most interesting phenomena that charm quark may be in position to illuminate is the CP violation. The standard model predicts a fairly small CP violation in charm (of order 10^{-3} , though even 10^{-2} is not excluded), and only for singly Cabibbo suppressed decays, such as the $D^+ \rightarrow \pi^-\pi^+\pi^+$. These small effects have not been measured yet but may now be within experimental reach. As mentioned earlier, the analysis of resonant substructure of this decay, using the technique called Dalitz analysis, is a promising approach to this question. The charm decay we focus on here, $D^+ \rightarrow \pi^-\pi^+\pi^+$, has a particularly rich resonant (Dalitz) structure, and hence the potential for interesting results. Once the Dalitz structure of the decay is understood with all intermediate resonances and their interference, we will have acquired a powerful tool for studying CP violation.

1.3 Charm at the Collider Detector at Fermilab

Hadron colliders at large center-of-mass energies are copious sources of charmed hadrons. At colliders such as the Tevatron the charm cross section is roughly $\frac{1}{500}$ of the total production cross section [5]. This high production cross-section paired with the large luminosity of $p\bar{p}$ collisions allows the Tevatron experiments to collect large charm samples. These samples allow precision measurements in the charm system, even for decays with very small branching ratios, such as $D^+ \rightarrow \pi^-\pi^+\pi^+$.

The final state in hadron-hadron collisions is quite complex, and the ability to distinguish signal from the large QCD background is imperative for any measurement. CDF has developed a powerful mechanism for triggering on charm events. The electronics of the silicon vertex tracker reconstructs parameters of tracks left by charged particles. This reconstruction is performed on-line, thereby allowing a decision on accepting or rejecting an event in real time. Particularly useful is the ability of the trigger system to make the decision based on the geometry of the track relative to the position of the $p\bar{p}$ interaction (the latter is called primary vertex). This allows triggering on displaced vertices and therefore collecting the events that contain decays of long-lived particles. The D^+ studied here, with the lifetime of the order of 10^{-12} s, is one such long-lived heavy flavor hadron. The details of the CDF's tracking and triggering system are described in the Chapter 3.

The measurement we present in this dissertation is a prerequisite for precision CP measurements and the first step for CDF in that direction. Presently, the most precise measurement of the branching ratio of $D^+ \rightarrow \pi^-\pi^+\pi^+$ decay relative to $D^+ \rightarrow K^-\pi^+\pi^+$ comes from CLEO-c, $(3.52 \pm 0.11 \pm 0.12)\%$ [6] and E791, $(3.11 \pm 0.18^{+0.16}_{-0.26})\%$ [7]. The Particle Data Group [8] lists $(3.48 \pm 0.19)\%$ as the world

average. We take upon us the task of significantly improving this knowledge and paving the way for the future CDF precision measurements of CP violation in charm.

Chapter 2

Theoretical Background

2.1 Standard Model: A Brief Summary

The standard model of particle physics is a theory that describes the strong, weak, and electromagnetic forces between fundamental (that is, structureless) particles. The advent of the standard model was the development of the electroweak theory in the late 1960's and early 1970's [9, 10, 11, 12].

The term “standard model” was coined in the late 1970s to include both electroweak theory and the theory of strong interactions known as quantum chromodynamics (QCD). The description for each interaction is built within the framework of quantum field theories, with the theory structure fixed by gauge symmetries. The standard model provides the description for all physics processes accessible to experiments to date. These descriptions match observations to an unprecedented accuracy.

While the theoretical framework was largely finalized throughout 1970s, a number of fundamental fermions and gauge bosons were yet to be seen. Their discoveries were made at the new experimental facilities around the world such as CERN Large

Electron Proton Collider, e^+e^- collider at SLAC or Tevatron, $p\bar{p}$ collider at FNAL, among others. After the discovery of the c quark in 1974, the discoveries of the b quark in 1977 [13] and t quark in 1995 [14, 15] completed the three generations of quarks in the standard model. The third generation lepton, the τ , has been found in 1975 [16]; the presence of its neutrino was inferred soon after. All fundamental fermions were thus observed, in agreement with the standard model predictions. The discovery of the W and the Z bosons in 1983 by the UA1 and UA2 collaborations at the CERN $p\bar{p}$ collider provided a direct confirmation of the unification of the weak and electromagnetic interactions [17, 18, 19, 20]. The final fundamental constituent of the standard model, the Higgs boson, a scalar particle that is responsible for the mechanism of mass generation in the standard model remains unobserved at this time.

The Standard Model is a relativistic gauge quantum field theory that is based on the symmetry group $SU(3) \times SU(2) \times U(1)$. The $SU(3)$ symmetry describes the color field of the quantum chromodynamics. The description of the electroweak interaction is implemented through $SU(2) \times U(1)$ symmetry, where $SU(2)$ symmetry describes the weak interaction, and $U(1)$ describes the electromagnetic field. Under $SU(2)$ the left-handed fermion fields transform as doublets, whereas the right-handed fields are $SU(2)$ singlets.

As a quantum field theory, the standard model uses the Lagrangian formalism to completely describe the system of particles and their interactions. The fundamental Lagrangian is constructed from the principles of gauge symmetry groups. Local gauge invariance in field theories is required for the theory to be renormalizable.

All the interactions are described by the Lagrangian terms that couple fermionic fields to the gauge bosons. For the first generation of fermions, the lagrangian has

the following form:

$$\begin{aligned}
 \mathcal{L} = & e \sum_{f=\nu,e,u,d} Q_f (\bar{f} \gamma^\mu f) A_\mu + \frac{g_2}{\cos \theta_w} \left\{ \sum_{f=\nu,e,u,d} (\bar{f}_L \gamma^\mu f_L) [T_f^3 - Q_f \sin^2 \theta_w] \right. \\
 & \left. + (\bar{f}_R \gamma^\mu f_R) [-Q_f \sin^2 \theta_w] \right\} Z_\mu \\
 & + \frac{g_2}{\sqrt{2}} [((\bar{u}_L \gamma^\mu d_L) + (\bar{\nu}_L \gamma^\mu e_L)) W_\mu^+ + ((\bar{d}'_L \gamma^\mu u_L) + (\bar{e}_L \gamma^\mu \nu_L)) W_\mu^-] \\
 & + \frac{g_3}{2} \sum_{q=u,d} (\bar{q}_\alpha \gamma^\mu \lambda_{\alpha\beta}^a q_\beta G_\mu^a), \tag{2.1}
 \end{aligned}$$

where e is the charge of the proton, A_μ is the photon field, W_μ^\pm and Z_μ are the charged and neutral weak boson fields, and G_μ^a are the gluon fields. The f_L , u_L , e_L and ν_L are the quark and lepton spinors. The subscripts L and R denote left-handedness and right-handedness. The Q_f and the T_f^3 are the operators of the $U(1)$ and $SU(2)$ groups. The first sum of the equation represents the electromagnetic interaction mediated by the photon field, the second and the third parts represent the weak interactions mediated by the neutral and the charged currents respectively, and the last part describes the strong interactions. The factors multiplying each sum (e , g_2 , g_3) are coupling constants. They characterize the strength of the interactions. The angle θ_w is the weak mixing angle, a parameter relating the strengths of the electromagnetic and weak interactions by $e = g_2 \sin \theta_w$.

By setting $\hbar = c = 1$, we can express the value of the coupling constants in natural units:

$$\alpha = \frac{e^2}{4\pi} \approx \frac{1}{137}, \alpha_w = \frac{g_2^2}{4\pi} = \frac{\sqrt{2} G_F M_W^2}{\pi} \approx \frac{1}{30}, \alpha_s = \frac{g_3^2}{4\pi} \approx \frac{1}{10}, \tag{2.2}$$

where G_F is the Fermi constant and M_W is the mass of the W boson. The coupling constants α (electromagnetic), α_w (weak), and α_s (strong) may be treated as effective running coupling constants, because they depend on the interaction energy. The electromagnetic and weak coupling constants, α and α_w , increase with the interaction energy, whereas the strong coupling, α_s , decreases.

2.2 Flavor Changing Interactions

The weak eigenstates of the quark fields are not the mass eigenstates. The quark fields d' that appear in the electroweak Lagrangian are related to the mass eigenstates of the QCD Lagrangian by

$$d'_i = V_{ij}d_j, \tag{2.3}$$

where V_{ij} is the 3×3 Cabibbo-Kobayashi-Maskawa (CKM) matrix, and the Einstein summation convention is employed. The CKM matrix describes the flavor changing charged current transitions. Flavor changing neutral currents corresponding to the transitions among the up-type or down-type quarks are, at the lowest order of the perturbation theory, absent. The CKM elements are among the standard model's parameters which, though fundamental, are not predicted by the theory. They must be extracted experimentally.

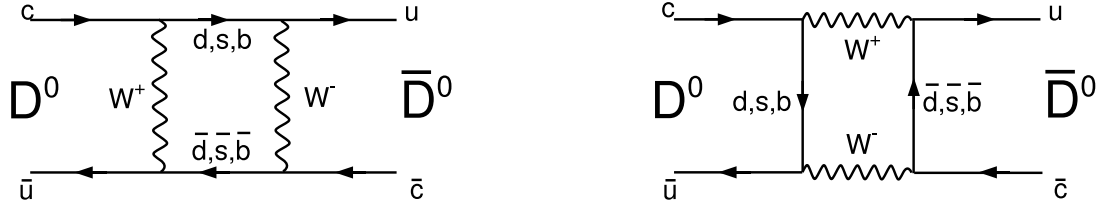
A general 3×3 unitary matrix has nine parameters. Three of these are the rotation parameters, that is, Euler angles, and of the remaining six phases, five can be absorbed by phase rotations of the quark fields. The one phase common to all

quarks remains. The CKM matrix contains four real parameters: three angles and one phase. The physical phase is important, because it is the only part of the standard model that allows for violation of CP symmetry by flavor-changing interactions.

The invariance with respect to sequential transformation of charge conjugation (C), parity (P), and time reversal (T), the so called CPT invariance, is the intrinsic property of any quantum field theory. As such, CPT is a symmetry of the standard model. The CPT invariance restricts the ways CP violation can be introduced in the standard model. It is possible to implement CP violation only through a complex phase in some effective couplings. For it to become observable, two different yet coherent amplitudes have to contribute to an observable. There are two types of scenarios for implementing this requirement. The first one is called direct CP violation, which can occur when two different amplitudes of fixed ratio exist leading coherently to the same final state. This may occur in the decays of the charged and neutral charm mesons and baryons, such as $D^+ \rightarrow \pi^- \pi^+ \pi^+$. (Recall that the charge conjugate mode is implicitly included.

The second possible scenario for CP violation is that of oscillations. Some neutral mesons may undergo transformations from particle to antiparticle and back. That is, the probability to observe a given meson as a particle or as an antiparticle may oscillate in time. The conversion between particles and antiparticles is possible through the weak processes with box diagrams, shown in Figure 2.1 for the D^0 meson. For such mesons, the presence of oscillations provides alternative paths to a final state contributing the second interfering amplitude that varies in time.

The direct CP violation is the process that concerns us here. Consider a final state f that can be reached coherently via two different quark level transition amplitudes, \mathcal{M}_1 and \mathcal{M}_2 :


 Figure 2.1: Feynman diagram for mixing of D^0 mesons.

$$\mathcal{T}(D \rightarrow f) = \lambda_1 \mathcal{M}_1 + \lambda_2 \mathcal{M}_2. \quad (2.4)$$

We have factored out the weak couplings $\lambda_{1,2}$ while allowing the amplitudes $\mathcal{M}_{1,2}$ to be complex due to strong or electromagnetic final state interactions (FSI). For the CP conjugate reaction one gets:

$$\mathcal{T}(\bar{D} \rightarrow \bar{f}) = \lambda_1^* \mathcal{M}_1 + \lambda_2^* \mathcal{M}_2. \quad (2.5)$$

The reduced amplitudes $\mathcal{M}_{1,2}$ remain unchanged because strong and electromagnetic forces conserve CP symmetry. For the particle and antiparticle decay rates, we find

$$\frac{\Gamma(\bar{D} \rightarrow \bar{f}) - \Gamma(D \rightarrow f)}{\Gamma(\bar{D} \rightarrow \bar{f}) + \Gamma(D \rightarrow f)} = \frac{2Im\lambda_1\lambda_2^*Im\mathcal{M}_1\mathcal{M}_2^*}{|\lambda_1|^2|\mathcal{M}_1|^2 + |\lambda_2|^2|\mathcal{M}_2|^2 + 2Re\lambda_1\lambda_2^*Re\mathcal{M}_1\mathcal{M}_2^*}. \quad (2.6)$$

CP symmetry implies that laws of nature are the same for particles and antiparticles. Therefore, if the rates of the two decays are not the same, that is, if $\Gamma(\bar{D} \rightarrow \bar{f}) - \Gamma(D \rightarrow f)$ is not zero, we have CP violation. According to the above equation, two conditions need to be satisfied in order for direct CP violation to occur. First, there has to be a relative phase between the weak couplings $\lambda_{1,2}$ (that is,

$Im\lambda_1\lambda_2^*$ must be non-zero). This means that, within the standard model, such effect can occur in singly Cabibbo suppressed decays but not in Cabibbo allowed or doubly suppressed decays. Here, Cabibbo suppression refers to the reduced cross section of processes that involve a vertex with up-like and down-like quarks of different generations. A vertex containing a $c \rightarrow s$ transition is Cabibbo favored, whereas one containing $c \rightarrow d$ transition is Cabibbo suppressed. Consequently, processes without any suppressed vertices are Cabibbo favored, processes containing one vertex between quarks of different generations are singly Cabibbo suppressed, and processes containing two such vertices are doubly Cabibbo suppressed. The second condition that must be satisfied for the direct CP violation to occur, according to the above formula, is that there be a nontrivial final state interaction (FSI), inducing a phase shift between $\mathcal{M}_{1,2}$ such that $Im\mathcal{M}_1\mathcal{M}_2^*$ is non-zero. These are present in the charm sector and lead to sizable phase shifts.

If we are to look for CP violation in charm sector, then, singly Cabibbo suppressed decays of D mesons provide good candidates. The $D^+ \rightarrow \pi^-\pi^+\pi^+$ decay is singly Cabibbo suppressed, while $D^+ \rightarrow K^-\pi^+\pi^+$, and $D_s \rightarrow K^-\pi^+\pi^+$ are not. The $D^+ \rightarrow \pi^-\pi^+\pi^+$ decay provides a good candidate for CP violating flavor-changing interaction because it can proceed not only through the Cabibbo suppressed tree diagram, but also through the Cabibbo allowed penguin diagram (see Figure 2.2). Interference between tree diagram contribution and the penguin diagram contribution calls for CP asymmetry at the 10^{-3} level, within the standard model. Present experimental limits on direct CP violation in charm decays do not exclude direct CP variation at the 10^{-2} level [5]. A CP asymmetry this large would provide evidence for new physics.

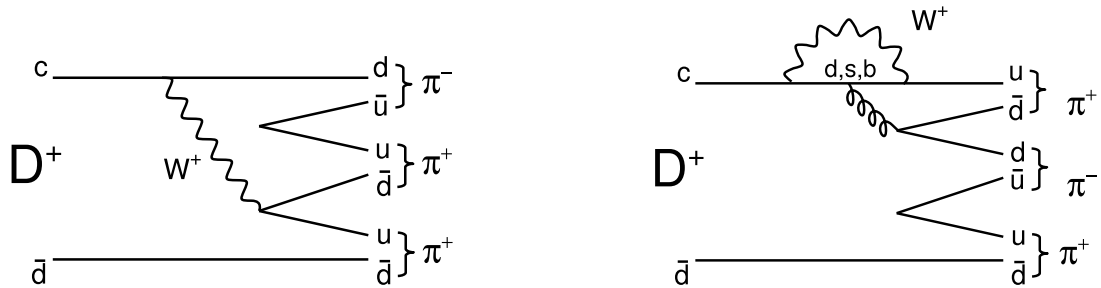


Figure 2.2: Cabibbo suppressed tree (left) and penguin (right) diagrams of the $D^+ \rightarrow \pi^- \pi^+ \pi^+$ decay.

2.3 Dalitz Structure of Three Body Decays

Decays of a parent particle into several daughter particles often proceed through very short-lived intermediate states. These states have well defined quantum numbers but live for such a short interval of time that they can not be observed directly. These intermediate particle states are called resonances. Examples of resonances include ρ and K^* mesons. Understanding the properties of any multi-body decay involves studying the resonant structure of the decay: establishing presence of the resonant states, determining contributions to the final state made through the resonances, and the degree of interference among amplitudes of the different resonant decays. Among the interesting decay properties of multi body decays is the possibility of direct CP violation that may not be visible when looking only at the final products of the decay. As the CPT invariance of physics laws implies equal lifetimes for particles and antiparticles, it must be that $\Sigma\Gamma(D \rightarrow f) = \Sigma\Gamma(\bar{D} \rightarrow \bar{f})$. CP violation in one decay mode therefore implies CP violation in another mode. One possible scenario is that a sizable CP violation washes out in the sum of all decay paths, but is present and observable in decay probabilities of individual paths that proceed through different

resonances.

The method of Dalitz analysis is often employed for studies of resonance structure. Let us consider a decay of a heavy particle into three lighter charged particles, as is the case in $D^+ \rightarrow \pi^- \pi^+ \pi^+$. For a sample of such decays the Dalitz plot can be obtained by calculating the invariant mass of the pairs of daughter particles, squaring them, and adding an entry point for each decay on the plane of squared two-body invariant masses. In our case, we deal with the invariant masses of pairs of oppositely charged daughter particles, m_{12} and m_{13} . Due to their opposite charge, these particles can form neutral resonances which are much more likely than charged resonances. A two-body intermediate resonance which decays into a pair of oppositely charged particles can be observed on the Dalitz plot as a band parallel to the horizontal or vertical axis, as in Figure 2.3. The density distribution of the Dalitz plot also allows study of the interferences between the different amplitudes producing the same 3-particle final state.

This dissertation does not aim to precisely determine the resonant structure of the $D^+ \rightarrow \pi^- \pi^+ \pi^+$ decays. However, understanding of the decay Dalitz structure at good enough level is necessary to obtain a measurement of the branching fractions measured here. The resonant states are abundant in our target D^+ decays, especially in $D^+ \rightarrow \pi^- \pi^+ \pi^+$. They shape the decay kinematics and thereby affect the mass spectra shapes and the efficiency rates. We therefore introduce here the basic quantities of the formalism of Dalitz analysis. Although we do not perform the full Dalitz analysis of our data, we use the formalism to adjust Monte Carlo simulation procedure of $D^+ \rightarrow \pi^- \pi^+ \pi^+$ decays so that they closely mimic the resonant structure in the data (Section 6.2).

The invariant masses of the three combinations of daughter particles pairs (12,

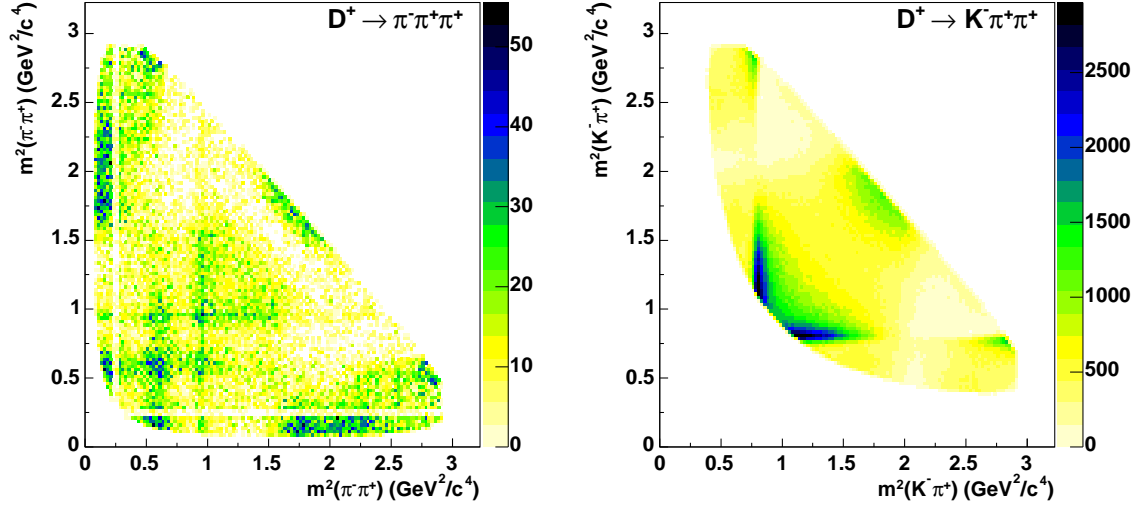


Figure 2.3: Dalitz plots of our $D^+ \rightarrow \pi^- \pi^+ \pi^+$ (left) and $D^+ \rightarrow K^- \pi^+ \pi^+$ (right) decays. The high mass corners and the low mass band are cut off due to kinematic constraints to suppress background.

13, and 23) are related by:

$$m_D^2 = m_{12}^2 + m_{13}^2 + m_{23}^2 - m_1^2 - m_2^2 - m_3^2 \quad (2.7)$$

where m_D is the mass of the D^+ , m_1 is the mass of its oppositely charged daughter (pion in $D^+ \rightarrow \pi^- \pi^+ \pi^+$ decay, kaon in $D^+ \rightarrow K^- \pi^+ \pi^+$ decay), and m_2 and m_3 are masses of the other two daughters (pions in either of the D^+ decays). The decay width is a squared magnitude of the sum of resonant contributions and the non-resonant contribution:

$$\Gamma(m_{12}^2, m_{13}^2) = \left| a_0 e^{i\delta_0} + \sum_{n=1}^N a_n e^{i\delta_n} A_n(m_{12}^2, m_{13}^2) \right|^2, \quad (2.8)$$

where a_n indicates the amplitude of each resonance ($n = 0$ corresponds to non-resonant contribution) and δ_n the complex phase.

The amplitude of each resonance is the product of a relativistic Breit-Wigner function

$$BW_n = \frac{1}{m_{12}^2 - m_r^2 - im_r\Gamma(m_{12})} \quad (2.9)$$

where m_R is the resonance mass and $\Gamma(m_{12})$ the width the resonance would have if its mass were m_{12} , and an angular factor that depends on the spin:

$${}^J M_n = 1 \quad \text{for } J = 0, \quad (2.10)$$

$${}^J M_n = -2|p_2||p_3| \cos \theta \quad \text{for } J = 1, \quad (2.11)$$

$${}^J M_n = -\frac{4}{3}(|p_2||p_3|)^2(3 \cos^2 \theta - 1) \quad \text{for } J = 2, \quad (2.12)$$

where p_2 and p_3 are the momenta of particles 2 and 3 in the 12 rest frame and θ the angle between particles 2 and 3 in the 12 rest frame.

The mass-dependent width in the Breit-Wigner is defined as:

$$\Gamma(m_{12}) = \Gamma_0 \frac{m_{12}}{m_r} \left(\frac{p^*}{p_0^*} \right)^{2J+1}, \quad (2.13)$$

where p^* is the momentum of particles 1 and 2 in the 12 rest frame, and p_0^* the momentum of particles 1 and 2 in the 12 rest frame for $m_{12} = m_r$.

Resonant fit fraction f_n is defined as

$$f_n = \frac{\int |a_n A_n(m_{12}^2, m_{13})|^2 dm_{12}^2 dm_{13}^2}{\int \Gamma(m_{12}^2, m_{13}) dm_{12}^2 dm_{13}^2}. \quad (2.14)$$

Note that, for $D^+ \rightarrow K^- \pi^+ \pi^+$ and $D^+ \rightarrow \pi^- \pi^+ \pi^+$ decays, every resonance

CHAPTER 2. THEORETICAL BACKGROUND

appears twice, once between daughter 1 and 2 and once between daughter 1 and 3.

Chapter 3

Experimental Apparatus

This measurement is performed on collisions data provided by the Tevatron accelerator at the Fermi National Accelerator Laboratory. The data was collected by the Collider Detector at Fermilab (CDF), which is one of the two detectors positioned at the interaction points along Tevatron's circumference. This chapter sketches the process of producing and accelerating proton and antiproton beams and then describes the CDF detector, a 5000 ton structure designed to deal with more than million high energy particle interactions per second. The trigger system, tracking, vertexing, and data set creation are described in detail.

3.1 Tevatron - The Source of $p\bar{p}$ Collisions

Particle acceleration at the Tevatron takes place in a complex accelerator system and proceeds through several stages. Figure 3.1 shows the diagram of the accelerator complex.

Proton Production

The Cockroft-Walton pre-accelerator is the first stage of the process - production and preparation of protons. In the Cocroft-Walton, hydrogen atoms are ionized to H^- ions, which are then accelerated by a positive voltage to kinetic energies of 750 keV. In the second stage of acceleration, the hydrogen ions go through a 150 m long linear accelerator called the Linac. There, electric fields oscillating at a radio frequency (RF) of about 800MHz accelerate them to energies of 400 MeV. The H^- beam is then directed through a carbon foil which strips the ions of the electrons. The resulting protons are inserted into the Booster, a circular synchrotron with a diameter of about 150 meters. In the Booster, the protons get injected onto the orbit of the protons already circulating in the machine. This overlaying of the existing beam with new particles builds the intensity of the beam. After about 20,000 revolutions, protons leave the Booster with 8 GeV of energy, grouped into 84 bunches of 6×10^{10} particles and spaced 18.9 ns apart. They are then injected into the Main Injector.

Main Injector

The Main Injector, a synchrotron with the diameter seven times that of Booster, operating at the frequency of 53 MHz, performs several functions. It receives both protons (from Booster) and antiprotons (from Antiproton Source, see below) with 8 GeV of energy, accelerates them up to 150 GeV and groups them into 36 bunches, after which they are ready for injection into the Tevatron. It also delivers 120 GeV proton beams to the fixed target and neutrino experiments, and to the Antiproton Source, where they are used for antiproton production.

A major advantage of a $p\bar{p}$ collider is that both proton and antiproton beams can

be circulated in the opposite directions using the same magnet and vacuum system.

Antiproton Production

Being antimatter, antiprotons are much harder to produce than protons; indeed, the most important limiting factor on the luminosity of a $p\bar{p}$ collider is the delivery of large enough stack of antiprotons.

To produce antiprotons, 120 GeV protons from the Main Injector are smashed into a nickel target. For every million incident protons, inelastic collisions yield about 20 antiprotons, with mean kinetic energy of 8 GeV. These are collected, focused, and separated from the other products of the proton-nickel scattering by a bending magnet.

At this stage of the process, the antiprotons' momenta vary widely in both longitudinal and transverse directions. Before further acceleration, their phase space volume is reduced. Because this thermodynamically corresponds to lower temperature state, the process is referred to as beam cooling. For protons, which are much more available, particles outside of the desired phase space volume can be dropped; for antiprotons this would be significant loss, and the more complex procedure is needed. The method used is known as stochastic cooling, a sophisticated, feedback-based method in which the particles' motion is sampled using sensors around the beam and corrected accordingly by kicker electrodes and magnets, reducing the beam size and momentum spread of the antiprotons. The stacking of antiprotons in the Accumulator ring takes up to a day.

For transfer to the Tevatron, the antiprotons in the stack get bunched into a configuration identical to that of protons and sent to the Main Injector. There they are accelerated to 150 GeV and then sent to the Tevatron.

The time interval of stable circulation of the beams in the Tevatron is referred to as store. Not all of the antiprotons from the stack are used during a single store. The ones not used, about 75% of the initially stacked particles, are sent to the Recycler, a Main Injector enclosure that functions as an antiproton storage ring. The antiprotons are set aside for future use, thus significantly reducing stacking time.

Tevatron

The final acceleration and collision of the beams occurs in the Tevatron. Protons and antiprotons are received at 150 GeV. Protons are loaded first, and antiprotons follow in the opposite direction in a separate trajectory. A set of electrostatic separators create two non-intersecting orbits, with protons traveling along one orbit and antiprotons along the other. Thus, as the beam bunches pass each other at the four crossing points other than B0 and DØ (the sites of the detectors), they are separated in the transverse plane and do not interact. The beams circulate in three trains of 12 bunches. The trains are separated by about $2.6 \mu\text{s}$, and the bunches of one train by 396 ns. The protons and antiprotons are accelerated to their final energy of 980 GeV. The fully accelerated beams circle the 6.28 km ring at nearly the speed of light. The beams are then focused further at the sites of the detectors, from about 1 mm to about $25 \mu\text{m}$ in diameter, to increase the probability of collision.

The rate of collisions is proportional to instantaneous luminosity. In the absence of a beam crossing angle or position offset, this is approximately given by

$$L = \frac{f N_B N_p N_{\bar{p}}}{2\pi(\delta_p^2 + \delta_{\bar{p}}^2)} F\left(\frac{\delta_l}{\beta^*}\right). \quad (3.1)$$

Here f is the bunch revolution frequency, N_B is the number of bunches, $N_{p(\bar{p})}$ is the number of protons (antiprotons) in a bunch, and $\delta_{p(\bar{p})}$ is the root-mean-squared proton (antiproton) transverse beam size at the interaction point. F is a form factor of the bunch shape. It depends on the ratio of the bunch length δ_l and the beta function, β^* , the latter being a measure of beam focusing. The design parameters for the Run II at the Tevatron that go into this formula are listed in Table 3.1.

The rate of $p\bar{p}$ collisions is directly proportional to luminosity. Clearly, decreasing the beam size $\delta_{p(\bar{p})}$ and increasing the number of particles in one bunch $N_{p(\bar{p})}$, results in a larger collision rate.

Of more meaning for physics analyses is the integrated luminosity, defined as instantaneous luminosity integrated over time:

$$\mathcal{L} = \int L dt [cm^{-2}]. \quad (3.2)$$

The probability of interaction is also proportional to the cross section of the process, σ . Though cross sections are by definition expressed in cm^2 , in high energy physics the more often used unit is the barn, ($1b = 10^{-24} cm^2$). Luminosity is then usually expressed in inverse barns, or in case of CDF, inverse picobarns, pb^{-1} .

The instantaneous luminosity degrades during a store due to particle losses and beam heat-up. Meanwhile, antiprotons are being stored in the Accumulator. After about 15 hours of running, it becomes beneficial to terminate the store and start a new acceleration cycle.

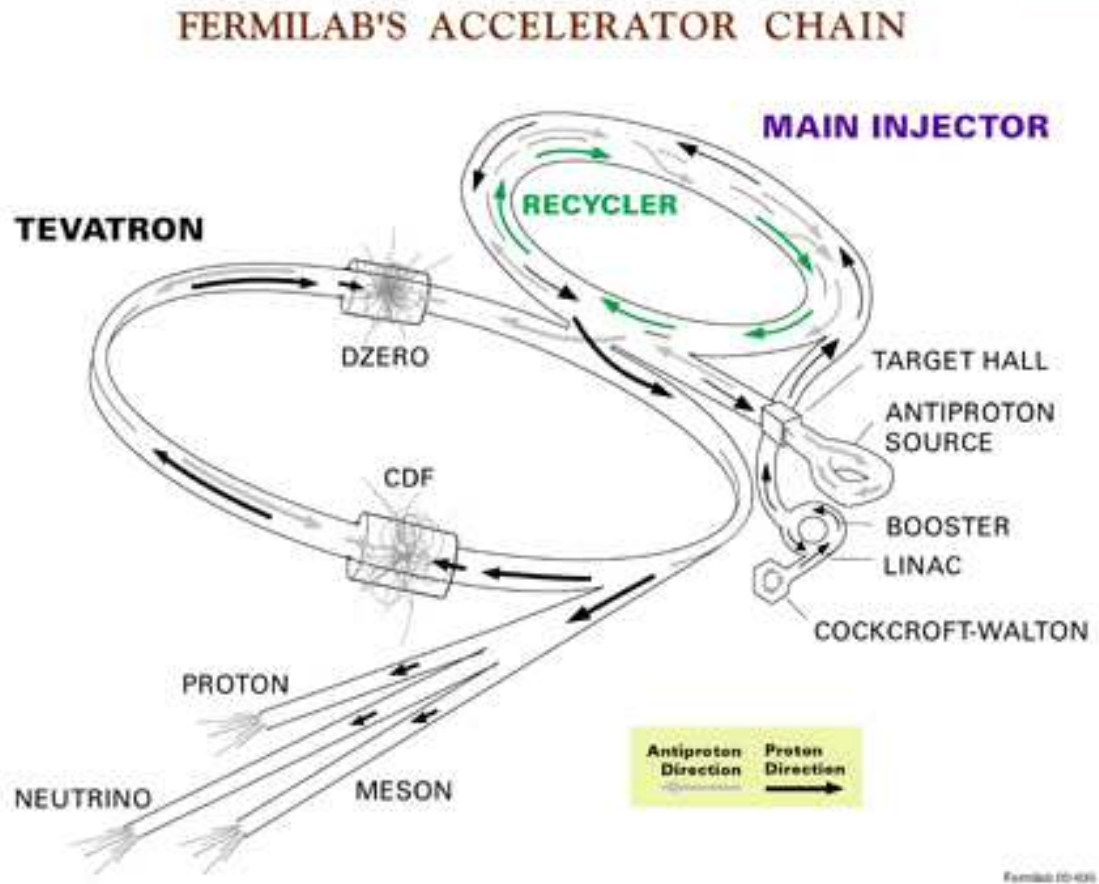


Figure 3.1: Diagram of the Tevatron accelerator complex.

Parameter	Value
number of bunches (N_B)	36
bunch rms size [m]	0.37
bunch spacing [ns]	396
protons/bunch (N_p)	2.7×10^{11}
antiprotons/bunch ($N_{\bar{p}}$)	3.0×10^{10}
total antiprotons	1.1×10^{12}
β^* [cm]	35
interactions/crossing	2.3
peak luminosity [$cm^{-2}s^{-1}$]	1.2×10^{32}

Table 3.1: Tevatron system Run II parameters.

3.2 CDF II Detector

The Collider Detector at Fermilab (CDF) is a general purpose particle detector designed to study $p\bar{p}$ collisions. It was built at one of the two Tevatron's interaction points and is azimuthally and forward-backward symmetric with respect to the collision axis. Rather than specializing for a specific class of physics measurements, the detector is optimized to capture properties of all kinds of particles coming out of $p\bar{p}$ collisions. The basic layout is common for such detectors and is outlined in Figure 3.2.

Charged particles are detected by the tracking system, the innermost part of the detector, which has cylindrical geometry concentric with the beam. The system consists of the silicon microstrip detector and a multi-wire drift chamber. These are immersed into a solenoidal magnetic field of 1.4T parallel to the beam axis. The system detects charged particles, records their trajectories, and measures their momenta. The reconstructed particle trajectories are referred to as tracks (hence the expression tracking system). Track reconstruction allows the identification of vertices. A vertex indicates the location of either $p\bar{p}$ interaction (primary vertex) or decay of a long lived particle resulting from the collision (secondary vertex).

Surrounding the tracking system is the Time of Flight (TOF) detector, designed to provide particle identification for low momentum charged particles. Together with the tracking system, it is lodged inside the superconducting coil which generates the magnetic field for measuring particle momenta. Around the coil is the calorimeter, the detector subsystem designed to measure energy of particles which shower when interacting with matter. The calorimeter consists of electromagnetic and hadronic parts, corresponding to the different interactions of the particle species with matter. The outermost component of the detector is the muon system, a set of drift chambers. Muons are, at energies in question, minimally ionizing particles. They do not interact with the calorimeter system, by virtue of its design. Therefore, muons deposit only a small fraction of their energy into the detector and pass largely unaffected through most of it. They are identified by the tracks they leave in the muon drift chambers.

The tracking system is the primary sub-detector system used in this analysis and will therefore be described in more detail.

To understand the observed events, we must keep in mind the energy balance of $p\bar{p}$ collisions. Only a fraction of the $p\bar{p}$ system's center of mass energy is carried by the partons - valence or sea quarks and gluons - which participate in the interactions we observe. Since the two interacting partons may have different momenta in opposite directions along the beamline, the resulting events often have large boosts along the beam (longitudinal) directions. The picture looks entirely different in the transverse plane, which is perpendicular to the beamline. Partons have negligible momenta in this plane, so the sum of all momenta of the outgoing particles in the transverse plane must be zero. This fact is used to infer presence of the particles that are not detected, such as neutrinos.

The origin of the CDF coordinate system is the geometrical center of the Central

Outer Tracker. This point represents the center of the CDF detector and roughly coincides with the center of the beam crossing region. The Cartesian x axis lies in the horizontal plane of the detector and points radially outward. The y axis points vertically upward. The z axis is the axis of the central tracker's cylinder. It is approximately parallel to the beam direction, with protons traveling in the positive z direction, making the coordinate system right-handed. CDF's barrel-like shape makes it convenient to use cylindrical (r, ϕ, z) or polar (r, ϕ, θ) coordinate systems. The correspondence between the Cartesian and cylindrical or polar systems is standard. The $r - \phi$ plane coincides with the $x - y$ plane. The polar angle θ is measured from the positive z axis.

Another angular variable, called pseudorapidity, is often used in place of the polar angle. It is defined as

$$\eta = -\ln \tan \frac{\theta}{2}. \quad (3.3)$$

Detector components are uniformly segmented in η and ϕ wherever appropriate, and pseudorapidity is then used to specify the geometrical coverage of the detector subsystems. This helps simplify the data analyses. The variable

$$\Delta R = \sqrt{\Delta\phi^2 + \Delta\eta^2}. \quad (3.4)$$

is often used for expressing coverage in terms of distance from the detector center.

Positions of other detector components are measured with respect to the tracker, either mechanically, usually by optical survey methods, or with data, where higher

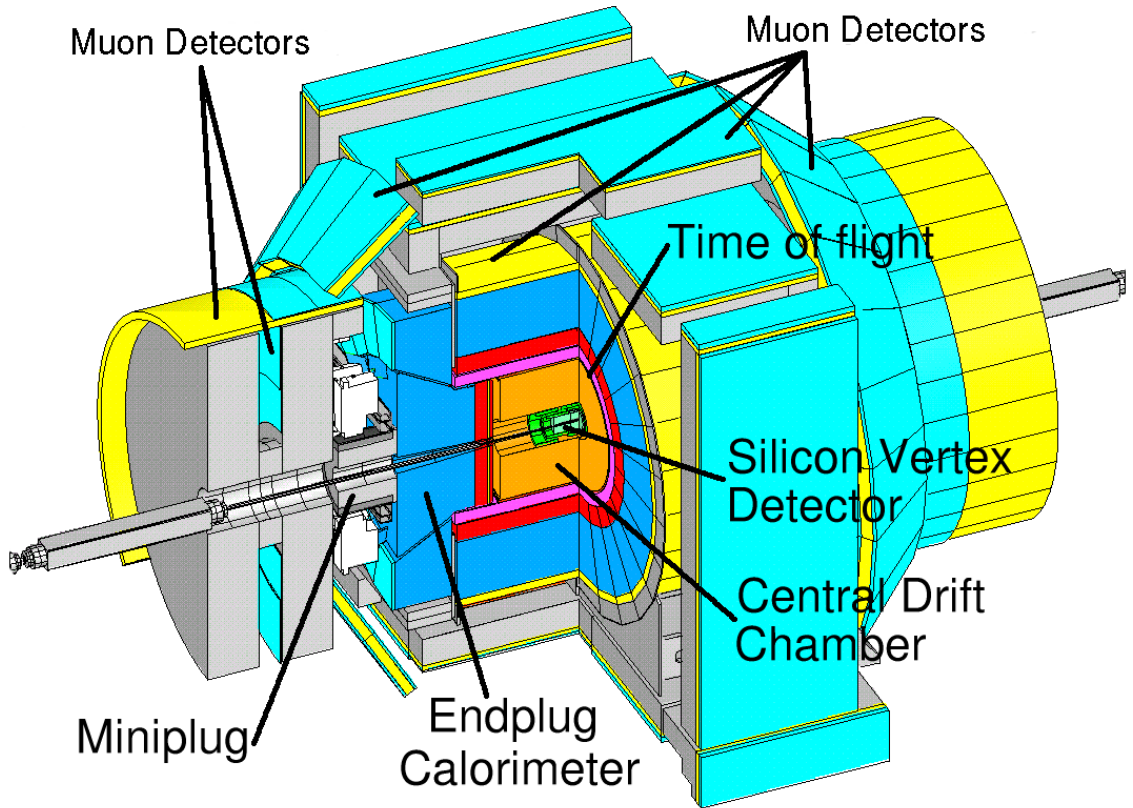


Figure 3.2: A 3D drawing of the CDF II detector with primary subsystems indicated.

precision is necessary. They are entered into alignment tables. A spatial measurement performed by a system other than the central tracker is usually done in the local reference system and converted into the global coordinates with the aid of alignment tables.

A more detailed description of the major detector subsystems follows. Unless otherwise specified, all descriptions refer to the CDF II detector, that is, the detector configuration during Run II when the data for this measurement were recorded.

For an even more thorough description of all CDF subsystems, refer to the Reference [21].

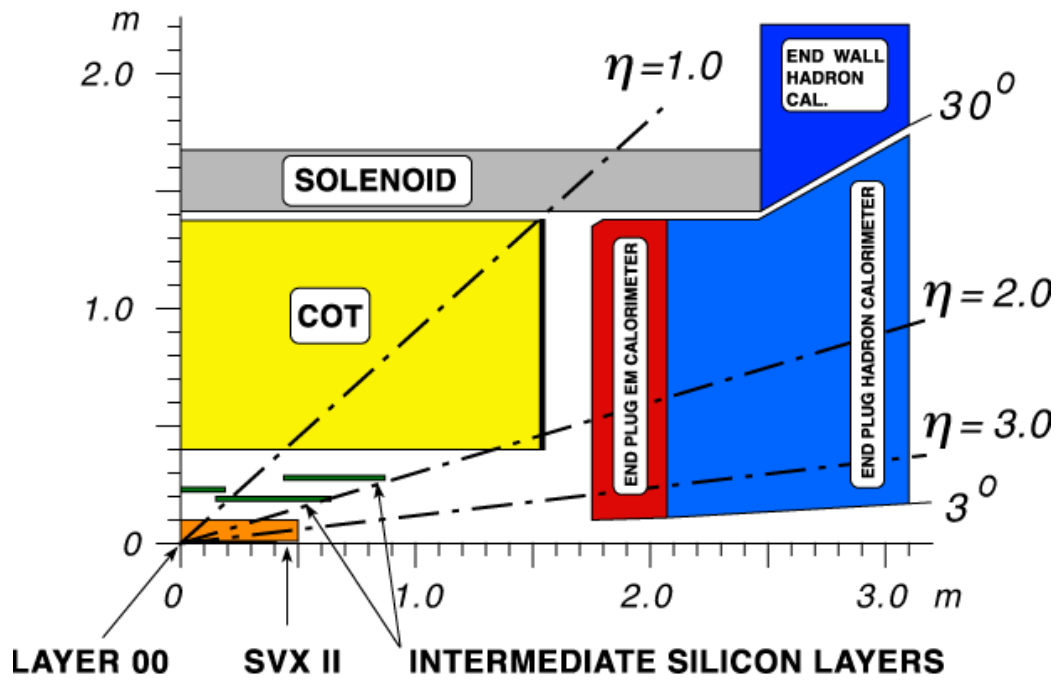


Figure 3.3: The $r-Z$ view of the CDF II detector illustrating pseudo-rapidity coverage of the tracking system.

3.2.1 Tracking and Vertexing

As they pass through matter, charged particles ionize it, leaving behind trails of charge and energy clusters. In the detector tracking system, these clusters are called hits. Detected hits are used to reconstruct trajectories (tracks); this process is accordingly called tracking. Intersections of multiple reconstructed tracks may indicate a vertex; the process of extrapolating reconstructed tracks to the point of intersection is called vertexing.

The CDF tracking system has two major components. The inner tracking device is a silicon microstrip vertex detector. It consists of three concentric systems. Installed directly on the vacuum beam pipe is Layer 00 (L00), a layer of silicon sensors at radii 1.35 and 1.62 cm from the beam. Five concentric layers of silicon sensors follow, composing the Silicon Vertex Detector (SVX) and covering radii between 2.45 and 10.6 cm. The SVX is the main part of the silicon tracking system. The Intermediate Silicon Layers, ISL, are the outermost silicon tracker component. They consist of one layer at $r = 22\text{ cm}$ in the central detector region and two layers at $r = 20\text{ cm}$ and $r = 28\text{ cm}$ in the forward regions. L00 detects hits in the transverse plane, thus yielding only r and ϕ coordinates, while the SVX and ISL also provide the z coordinate of the hits.

The Central Outer Tracker (COT), the largest coverage tracking system, is mounted outside of the silicon system. It is a 3.1 m long open-cell drift chamber covering radii between 40 and 137 cm. Layers of wire at a small stereo angle give z position for each hit. The $r - z$ map of the whole tracking system is shown on Figure 3.3.

In the solenoidal magnetic field of the tracking volume, charged particles' trajectories are helices. These are uniquely parametrized by five parameters. The CDF

coordinate system makes it convenient to choose the five parameters so that three of these parameters describe a position - the point of closest approach of the helix to the beam line - and two more to describe the momentum vector at that position. These parameters are

z_0 - z coordinate of the point of closest approach to the z axis,

d_0 - impact parameter: distance between the point of closest approach and the z axis,

ϕ_0 - ϕ coordinate of the transverse momentum of the particle, at the point of closest approach to the z axis,

$\cot \theta$ - helix pitch: the ratio of the helix step to its diameter,

C - helix curvature.

Both curvature and impact parameter are signed quantities. They are defined by:

$$C = \frac{q}{2R}, \quad (3.5)$$

$$d_0 = q(\sqrt{x_c^2 + y_c^2} - R), \quad (3.6)$$

where q is the charge of the particle, (x_c, y_c) is the location of the center of the helix as projected on the $x - y$ plane, and R is the helix radius.

The transverse and longitudinal components of a particle's momentum are determined from its track parameters:

$$p_T = \frac{cB}{2|C|}, \quad (3.7)$$

$$p_z = p_T \cot \theta, \quad (3.8)$$

To reconstruct the track and determine its parameters, a track fit is performed on the hits. The set of hits to be fitted is preselected by the pattern recognition algorithm. A helix is fit through the hits, and each hit is assigned an uncertainty, as determined in dedicated studies. The output of the fit is a set of track parameters and the error matrix, which includes the inter-parameter correlations. More about track reconstruction is given below.

Once the track is reconstructed, its point of creation, that is, production vertex, is sought. This is done by looking for an intersection between the track in question and at least one other track, under the assumption that the two particles originated in the decay of the same parent particle. The kinematic fitting program that does this determines the spatial coordinates of the intersection point and their uncertainties. Based on the track parameters and masses of the daughter particles, the program can also determine the mass of the parent and the associated uncertainty.

Central Outer Tracker

In the region of $|z| < 155 \text{ cm}$ and between radii of 44 and 132 cm, position measurements are made by the Central Outer Tracker, COT. The COT is a cylindrical multi-wire open-cell drift chamber filled with argon-ethane gas 50:50 mixture as the active medium for ionization. As they travel through the gas, charged particles leave a trail of ionization electrons. These electrons drift toward the sense wires, forced by the electric field created by cathode field wires and potential wires of the cell they are in. The drift time is used to precisely measure the spatial position. The drift is not in the direction of the electric field, because of the magnetic field parallel to the z axis. The crossed fields move the electrons in the plane perpendicular to the magnetic field, at angle α with respect to the electric field lines. This angle, known as the Lorentz angle, depends on the fields' magnitudes and the properties of the gas. In the COT, the Lorentz angle is 35° .

The best resolution is obtained if the drift is perpendicular to the particle trajectory. This is optimized for the high p_T tracks, which are almost radial. All cells are tilted by 35° away from the radial direction. The ionization electrons then drift along the ϕ direction. As they approach the sense wires, the local field accelerates them, making them source of secondary ionization. The avalanche of secondary ionization electrons produce a signal (hit) on the sense wire, which is further amplified and shaped by the electronics at the wire end. The $r - \phi$ position of the hit with respect to the sense wire is inferred from the arrival time of the signal. Note that, in order for a hit to be registered, the amount of charge arriving to the sense wire must be over a certain threshold: particles that deposit less ionization will have lower chance to register a hit.

A charged particle traveling radially and traversing the entire tracker ideally has 96 position measurements (hits). The cells are arranged in eight radially spaced superlayers, each including 12 sense wires. Figure 3.4 illustrates the geometrical arrangement of wires in one of the superlayers. The superlayers alternate between axial alignment (cell plane parallel to the z axis) and small angle stereo alignment (cell planes rotated by about $\pm 2^\circ$ around the radial direction). The stereo layers allow extracting the z axis coordinate of a hit. The $r - \phi$ track projection allows the measurement of curvature, impact parameter, and ϕ direction of the track. The hits from stereo layers appear to be offset from the reconstructed helix projection, in proportion to the z coordinate of the hit. Matching of the stereo hits to the existing $r - \phi$ track projection gives z coordinate information at four different radii, and the polar angle and z coordinate of the track can be determined.

The resolution of a single tracker hit has been measured to be about $140\mu\text{m}$. This corresponds to the transverse momentum resolution $\frac{\delta_{p_T}}{p_T} \approx 0.15\% \frac{p_T}{[GeV/c]}$. As the track momentum increases and the track becomes more radial, the uncertainty of the curvature measurement increases, and with it the uncertainty of the transverse momentum.

Silicon Vertex Detectors

The Silicon Vertex detector, SVX, allows high precision position measurements close to the beampipe. In this way, the resolution of the impact parameter is greatly improved, along with the ability to identify secondary vertices coming from decays of long lived particles. The latter property is essential for heavy flavor physics measurements.

Because it is positioned very close to the beampipe, the detector must be able to withstand high doses of radiation. A silicon microstrip detector such as the SVX has this ability to do high precision position measurements in a high radiation environment. The design of a silicon tracker in a hadron collider environment was pioneered by the CDF in Run I.

The basic principle of operation of a silicon tracker is not unlike that of the drift chamber tracker. The difference is that the position is not determined based on the drift time of ionization electrons, but rather on the knowledge of the coordinates of the very small volume in which the ionization occurred.

In a typical silicon microstrip detector, finely spaced strips of strongly doped p -type silicon (p^+) are implanted on a lightly doped n -type silicon (n^-) substrate, about $300\ \mu\text{m}$ thick. On the opposite side of the substrate a thin layer of strongly doped n -type silicon (n^+) is made. Positive voltage applied to the (n^+) side depletes the (n^-) volume of free electrons and creates an electric field. A charged particle crossing the substrate leaves a trail of electron-hole pairs as a result of ionization. In the electric field, the holes drift to the (p^+) strips and produce a well localized signal in the $r - \phi$ plane. The (n^+) side can also be built in the form of orthogonal electron-collecting strips and thus used to measure the $r - z$ coordinate of the hit.

Usually the signal is detected on a small cluster of strips, rather than just one. The hit position is derived by weighting the strip positions by the amount of charge collected. The accuracy achieved for the individual position measurement is about $12\ \mu\text{m}$.

The CDF Silicon VerteX Detector is built as three cylindrical barrels, each 29 cm long (see Figures 3.5-3.6). Each barrel supports five layers of double-sided silicon microstrip detectors covering radii between 2.5 cm and 10.7 cm. Layers are numbered

from zero (innermost) to four (outermost). Layers zero, one, and three combine an $r - \phi$ position measurement on one side with a 90° stereo ($r - z$) measurement on the other. Layers two and four combine the $r - \phi$ measurement with a small angle stereo measurement at 1.2° .

The actual silicon crystals, also called sensors or wafers, are supported by lightweight substrates in assemblies called ladders. Four wafers are housed in one ladder, and twelve ladders compose one silicon layer. Sixty ladders (five layers) are mounted between two precision machined beryllium bulkheads, and this structure is called a silicon vertex detector barrel.

Each ladder is read out at both its ends. Due to the large number of channels (405,504) and the nature of the signal, much of the electronics is mounted directly on the detector rather than housed outside of the detector and connected to it by cables. Having half a million cables coming out of the detector is impractical; besides, the signal would be lost in the noise unless amplified right away. However, the extra material inside the tracking volume has some negative side effects. One of them is extra Coulomb scattering of charged particles. Another is the heat dissipated by the electronics, which necessitates a cooling system. Cooling channels are incorporated into the bulkheads.

Because many triggers rely on the impact parameter as measured by the silicon vertex detector, it is essential that the beamline and the SVX axis coincide, lest the impact parameter becomes ϕ dependent. Thus, the SVX axis is offset from the central tracker (detector z) axis by the same amount as the beamline.

Silicon hit positions are initially obtained with respect to the individual ladders, and then translated to the detector global reference frame, so that they can be combined with the central tracker hits to obtain the best possible helical track fit. The

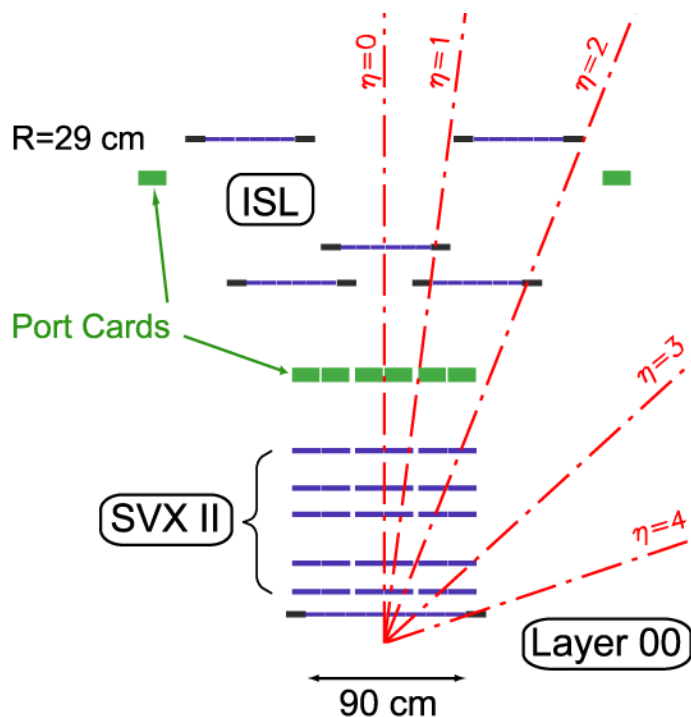


Figure 3.5: The design and coverage of the silicon subdetectors SVX, ISL and L00 in $r - z$ projection. The z coordinate is compressed.

conversion into the detector reference frame is done with the help of alignment tables, the quality of which is essential for the process.

Performance of the silicon vertex detector is measured by its impact parameter resolution. This is presently about $40 \mu\text{m}$, including the contribution of the beam width ($25\text{-}30 \mu\text{m}$). The z_0 resolution is somewhat worse, but at $70 \mu\text{m}$ (for tracks made using the Intermediate Silicon Layer as well as silicon vertex detector) is still quite respectable.

Such precise determination of the track parameters allows distinguishing between primary and secondary vertices, which is essential for identifying the long lived particles of heavy flavor physics.

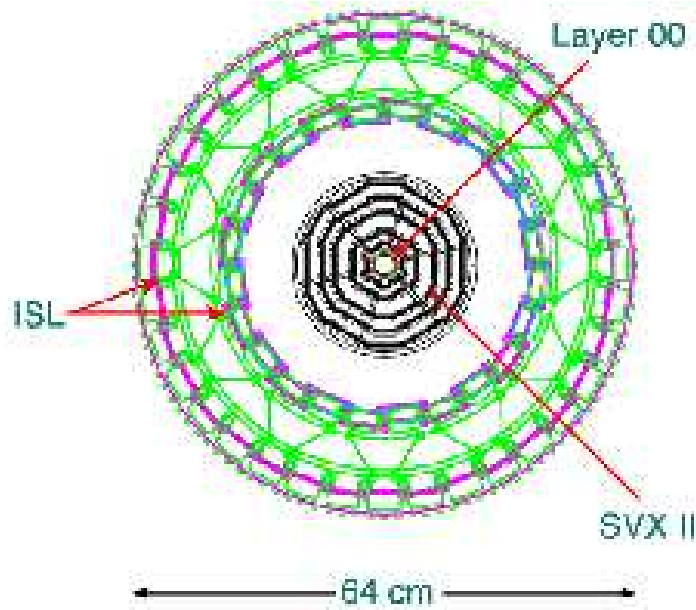


Figure 3.6: The $r - \phi$ view of the CDF silicon detectors, including SVX bulkhead and ISL support structure.

Intermediate Silicon Layer and Layer 00

Compared to other subdetectors, both the Intermediate Silicon Layer and Layer 00 were integrated into the CDF system quite late. Part of the reason for this was that they had no Run I predecessors, and Layer 00 was a “beyond baseline” project, facing many constraints. The detectors nevertheless improve the quality of tracking for the physics analyses. Note that, due to its late integration, Layer 00 is not used in this analysis.

For the Intermediate Silicon Layer, a single silicon layer is placed in the central detector region ($|\eta| < 1.0$), at a radius of 22 cm. In the region $1.0 < |\eta| < 2.0$ two layers of silicon are placed at 20 cm and 28 cm. The arrangement of barrels and layers is shown in Figures 3.5-3.6. Double sided silicon is used on both axial and stereo

sides with a 1.2° stereo angle. Only every other strip is read out, to reduce the total channel count to 268,800. This affects the single hit resolution, which is about $16\ \mu\text{m}$ on the axial side and $23\ \mu\text{m}$ on the stereo side, despite the fact that the ISL ladders are similar to those of the silicon vertex detector. The ISL improves tracking in the central region and for $1.0 < |\eta| < 2.0$ allows stand alone silicon tracking (together with the SVX).

Layer 00 has six narrow (128 channels) and six wide (256 channels) groups in ϕ at radii 1.35 cm and 1.62 cm, respectively, within a total length of 95 cm, mounted on a support structure which also provides cooling (see Figures 3.5-3.6). The sensors are made of light weight radiation hard silicon, different from that used in silicon vertex detector, and are single sided. This design is necessitated by the extreme proximity to the beamline. Layer 00 helps to reduce the multiple scattering for tracks passing through the high density regions of silicon vertex detector, where the bulkheads and the readout electronics are located. It gives impact parameter resolutions as small as $25\ \mu\text{m}$.

Track Reconstruction

To reconstruct tracks, the CDF tracking system uses several pattern recognition algorithms. Most of the tracks are reconstructed using “Outside-In” algorithms, described here. As the name suggests, the track reconstruction progresses from the outside of the tracking system inward.

The helical track, when projected onto the transverse plane, is a circle. The first step of pattern recognition is then to look for circular paths in radial superlayers of the central tracker. Supercells in the radial superlayers are searched for sets of 4 hits

that can be fit onto a straight line. These sets are called segments. The straight line fit for a segment is sufficient to extract a rough measurement of curvature and ϕ_0 . At this point there are two ways to proceed. One approach is to link together the segments with matching curvature and ϕ_0 . The other approach is to improve the curvature and the ϕ_0 of the segment reconstructed in the superlayer 8 by constraining its circular fit to the beamline, and then adding hits consistent with this path. Once a circular path is found in the transverse plane, hits in the stereo superlayers are added by their proximity to the circular fit. The result is a three dimensional track fit. Typically, if one algorithm fails to reconstruct a track, the other one will not. The track reconstruction efficiency in the COT for tracks that pass through all 8 superlayers ($p_T > 400 \text{ MeV}/c^2$) is about 95%. The track reconstruction efficiency depends mostly on how many tracks are present in a given event. In case of many tracks positioned close to each other, hits from one can shadow hits from another, resulting in efficiency loss.

Once a track is reconstructed in the central tracker, it is called a COT-only track and is extrapolated into the silicon vertex detector region. Because the track parameters are measured with uncertainties, this is like a three dimensional road of width σ , where σ is ϕ and z dependent. As the extrapolation proceeds from the outermost silicon layers inward, silicon clusters found inside the road are added to the track. With each added cluster, a track fit is performed, and the road gets narrower based on the improved knowledge of the track parameters. Reducing the width of the road reduces the chance of adding an incorrect hit to the track and reduces computation time. In the first pass of the algorithm, only $r - \phi$ silicon hits are used. In the second pass, the stereo hit information is added to the track. If, at the end of the process, there is more than one track candidate generated from the original COT-only track,

the best one is kept, the criteria again being hit multiplicity (first) and track quality (second).

3.2.2 Other detector systems

This section reviews systems which were not directly used in this analysis. Only brief summaries are given, together with the references to the detailed descriptions.

Calorimetry

CDF calorimetry is a scintillator sampling system of towers segmented in azimuthal angle and pseudorapidity, pointing radially to the interaction region. The radial matching of electromagnetic lead-scintillator (electromagnetic) and steel-scintillator (hadronic) towers allows a precise comparison of the energy deposited in the two, and thus gives good separation of electrons and photons from hadronic particles.

The detectors are divided into three regions in order of increasing pseudorapidity: central, wall and plug regions. In the central region are the Central Electro-Magnetic (CEM) and Central HAdron (CHA) calorimeters, in the wall region is the Wall HAdron (WHA), and in the plug region are the Plug Electro-Magnetic (PEM) and Plug HAdron (PHA) calorimeters. The central calorimeters cover 2π in azimuth and ± 1.1 in pseudorapidity for the EM, and ± 1.3 for the hadron calorimeter. Each tower spans 15° in azimuth and 0.11 in pseudorapidity. The plug calorimeters extend the pseudorapidity coverage to ± 3.6 and use variable segmentation optimized for targeted physics.

The Central and Plug electromagnetic calorimeters use lead sheets interspersed with scintillator as the active medium and photomultiplier tubes for the readout. Both

have shower maximum strip detectors, called CES and PES, embedded at about 6 radiation lengths (X_0) from the inner side. Shower maximum detectors contribute to electron/photon identification by matching the measurement of shower position with tracks. The CES is a gas multiwire proportional chamber, with a position resolution of 2 mm, while the PES is made of scintillating strips allowing for a resolution of about 1 mm.

Hadron calorimeter towers, iron-scintillator sampling devices, are located immediately behind the electromagnetic ones. Major characteristics are given in Table 3.2.

Subsystem	Thickness	Number of layers	Resolution ($E[\text{GeV}]$)
CEM	$19X_0$	20-30 Pb:3mm + Scint.:5mm	$\frac{13.5\%}{\sqrt{(E \sin(\theta))}} \oplus 2\%$
PEM	$21X_0$	22 Pb:4.5mm + Scint.:4mm + Preshower	$\frac{16\%}{\sqrt{(E \sin(\theta))}} \oplus 1\%$
CHA/WHA	$4.7/4.5\lambda_0$	32/15 Fe:25/50mm + Scint.:10mm	$\frac{75\%}{\sqrt{(E \sin(\theta))}} \oplus 3\%$
PHA	$7\lambda_0$	23 Fe:51mm + Scint.:6mm	$\frac{80\%}{\sqrt{(E \sin(\theta))}} \oplus 5\%$

Table 3.2: Basic parameters of the CDF II calorimetry.

More about CDF calorimetry design and usage can be found in references [21], [22], and [23].

Time of Flight

The Time of Flight system, TOF, improves CDF's particle identification capability in the low p_T region. The subdetector measures arrival time of the particle, t , with

respect to the collision time t_0 . The mass m of the particle is then determined from

$$m = \frac{p}{c} \sqrt{\frac{(ct)^2}{L^2} - 1}, \quad (3.9)$$

where L is the path length and p is the momentum, both as measured by the tracking system. The particle identification is then made based on the mass.

The time of flight detector consists of 216 scintillator bars installed at a radius of about 138 cm, in the 4.7 cm thick space between the outer shell of the central tracker and the superconducting solenoid. The bars are approximately 279 cm long and 4×4 cm² in cross section. The cylindrical geometry of the time of flight provides 2π azimuthal coverage and covers $|\eta| < 1$ in pseudorapidity. The specified resolution of the time of flight detector is approximately 100 ps.

Cherenkov Luminosity Counter

The Cherenkov Luminosity Counter, CLC, measures the average number of interactions per accelerator bunch crossing, μ . From this, the instantaneous luminosity L is extracted from interaction rate

$$\mu \cdot f_{bc} = \sigma_{p\bar{p}} \cdot L, \quad (3.10)$$

where $\sigma_{p\bar{p}}$ is the relatively well known total $p\bar{p}$ cross section at center-of-mass energy of 1.96 TeV, and f_{bc} is the bunch crossing rate of the Tevatron.

The luminosity counter utilizes Cherenkov radiation: particles traversing a medium

at a speed higher than the speed of light in this medium radiate light into a cone around the direction of motion. The opening angle of the Cherenkov cone depends on the ratio of the speed of particle to the speed of light in the medium and on the index of refraction of the medium. The counter uses an assembly of long gas Cherenkov counters positioned in the Plug Calorimeter 3° gap, which point toward the interaction point. Particles coming from the interaction point will have the longest flight path through the gas of the counter and will therefore produce the most radiation.

The luminosity counter's timing resolution of around 50 ps allows it to discern multiple interactions within the same bunch crossing and achieve an overall luminosity measurement accuracy of better than 5%.

Muon Detectors

Muons do not lose much of their energy in the detector material. Being 200 times heavier than electrons, they generate 40,000 times less bremsstrahlung radiation. As they travel through the detector, they are not subject to strong interactions with the atomic nuclei either. They are thus the most penetrating among charged particles, and together with neutrinos (which leave no trace in the detector) they are the only species likely to pass essentially undisturbed through the tracking volume and the calorimetry. This fact is exploited in their detection. The muon detectors are placed on the outside of the detector, some of them even behind additional steel absorbers.

While muons are extensively used for W and Z boson physics, semileptonic decays of top and bottom quarks, J/ψ triggers, and detector calibration, they are not used in this analysis. Their detection system will therefore be described very briefly.

CDF uses four systems of scintillators and proportional chambers in the detection

of muons across the region of $|\eta| < 2$. The Central MUon detector, CMU, is located outside of the hadron calorimeter at radial distance of 347 cm. The Central Muon uPgrade, CMP, is a rectangular box around additional steel absorbers, built to reduce contamination from hadronic calorimeter “punch throughs”. The Central Muon eXtension, CMX, designed to cover pseudorapidity range of $0.6 < |\eta| < 1.0$ The Intermediate MUon detector, IMU, covering the pseudorapidity region of $1.0 < |\eta| < 2.0$. Design parameters of these systems are summarized in Table 3.3. Scintillators are placed next to the muon chambers and used to suppress backgrounds from out-of-time interactions in the material of the beam pipe.

Muon candidates are identified by muon stubs, that is, by the track segments they leave in the muon chambers. If a stub can be matched to a track recorded by the central tracker, the two are combined and considered to come from a muon.

The heavy shielding along the path of muons provides for cleaner muons, but it also presents two additional issues. First, it causes muons to loose energy, albeit less so than other particle species. This will prevent those low energy muons with p_T below some threshold (called the rangeout threshold, specific to the muon system, refer to Table 3.3) from reaching the muon detectors. This is not a serious issue, because most of the muons of interest, especially the ones we trigger on, have fairly high transverse momenta. The second issue is the Coulomb scattering in the material, which defects the passing particle from its original path. The resulting point of entry and the muon stub may not match well the naively extrapolated COT track. This complicates the track-to-stub matching, but since the mismatch is fairly narrow and roughly gaussian in shape it does not present a large problem.

Parameter	CMU	CMP +CSP	CMX +CSX	IMU
Pseudo-rapidity ($ \eta $) coverage	0.0–0.6	0.0–0.6	0.6–1.0	0.6–1.0
Drift tube cross-section [cm ²]	2.7×6.4	2.5×15	2.5×15	2.5×8.4
Drift tube length [cm]	226	640	180	363
Maximum drift time [μ s]	0.8	1.4	1.4	0.8
Number of drift tubes	2304	1076	2208	1728
Scint. counter thickness [cm]		2.5	1.5	2.5
Scint. counter width [cm]		30	30-40	17
Scint. counter length [cm]		320	180	180
Number of scint. counters		269	324	864
Pion interaction lengths #	5.5	7.8	6.2	6.2-20
Minimum muon p_T [GeV/ c]	1.4	2.2	1.4	1.4-2.0
Multiple scat. resolution [cm/ p_T]	12	15	13	13-25

Table 3.3: Design parameters of the CDF muon system. Numbers of pion interaction lengths and multiple scattering resolution are given for reference angles: $\theta=90^\circ$ for CMU and CMP/CSP, and $\theta=55^\circ$ for CMX/CSX.

3.3 Trigger System

Proton and antiproton bunches cross in the Tevatron ring every 396 ns. This translates into a collision rate of 2.5 MHz, an enormous rate of events, not all of which can be recorded.

In fact, most of the events will be discarded. One reason is that the amount of data is beyond the current storage and throughput capacities. With an average size of event being of the order of 100 Kb, the required bandwidth would be 250 Gb/s, which is not only difficult and expensive to maintain, but would result in 150 Pb of data recorded after just one week of data taking. Another major impediment to keeping most events is that the readout time for the whole detector is about 2 ms, which is long enough for another 5,000 interactions to happen, and go unrecorded.

However, most processes of interest to us have cross sections of the order of 10 -

$100 \mu\text{b}$ or smaller, that is, at least three orders of magnitude smaller than the total $p\bar{p}$ cross section. This greatly reduces the readout speed and storage size problems, if we can record just the interesting events, selected in real time. But there are clear limitations with this approach as well: it is not possible to make an accurate decision about how interesting an event is within the 396 ns before the next event comes along. The solution in CDF is to stage triggering decisions in three levels, as outlined in the Figure 3.7. The system is designed to have close to zero deadtime, that is, to have specified few or no events unprocessed because the electronic resources are busy with previously entered events.

Each level of the trigger is given a certain amount of time to reach a decision about accepting or rejecting an event. By increasing the time allowed for processing at the increasing trigger levels, the complexity of the reconstruction can be increased with each new level. At the first level of trigger, only very rough and quick pattern recognition and filtering algorithms are used. Level 1 trigger discards the events which do not have any interesting signatures. These represent the vast majority of all events. It can take as long as $5.5 \mu\text{s}$ for the Level 1 to reach its decision. To make time for decision making, detector readout information is stored in a data pipeline. At Level 1, this is 14 bunch crossings, or 42 slots deep. For every Tevatron clock cycle, the event is moved up one slot in the pipeline. By the time it reaches the end of the pipeline, the trigger will have reached the decision whether to accept or reject this event. The total time allocated for reaching the Level 1 decision is about $5.5 \mu\text{s}$, and the trigger accept rate is below 50 kHz.

If the event is accepted by Level 1 trigger, it proceeds to Level 2, which does a more detailed analysis. Level 2 has 4 buffers and hence allows about $20 \mu\text{s}$ for a decision to be reached. The Level 2 accept rate is around 300 Hz. Only if the Level 2 criteria are

RUN II TRIGGER SYSTEM

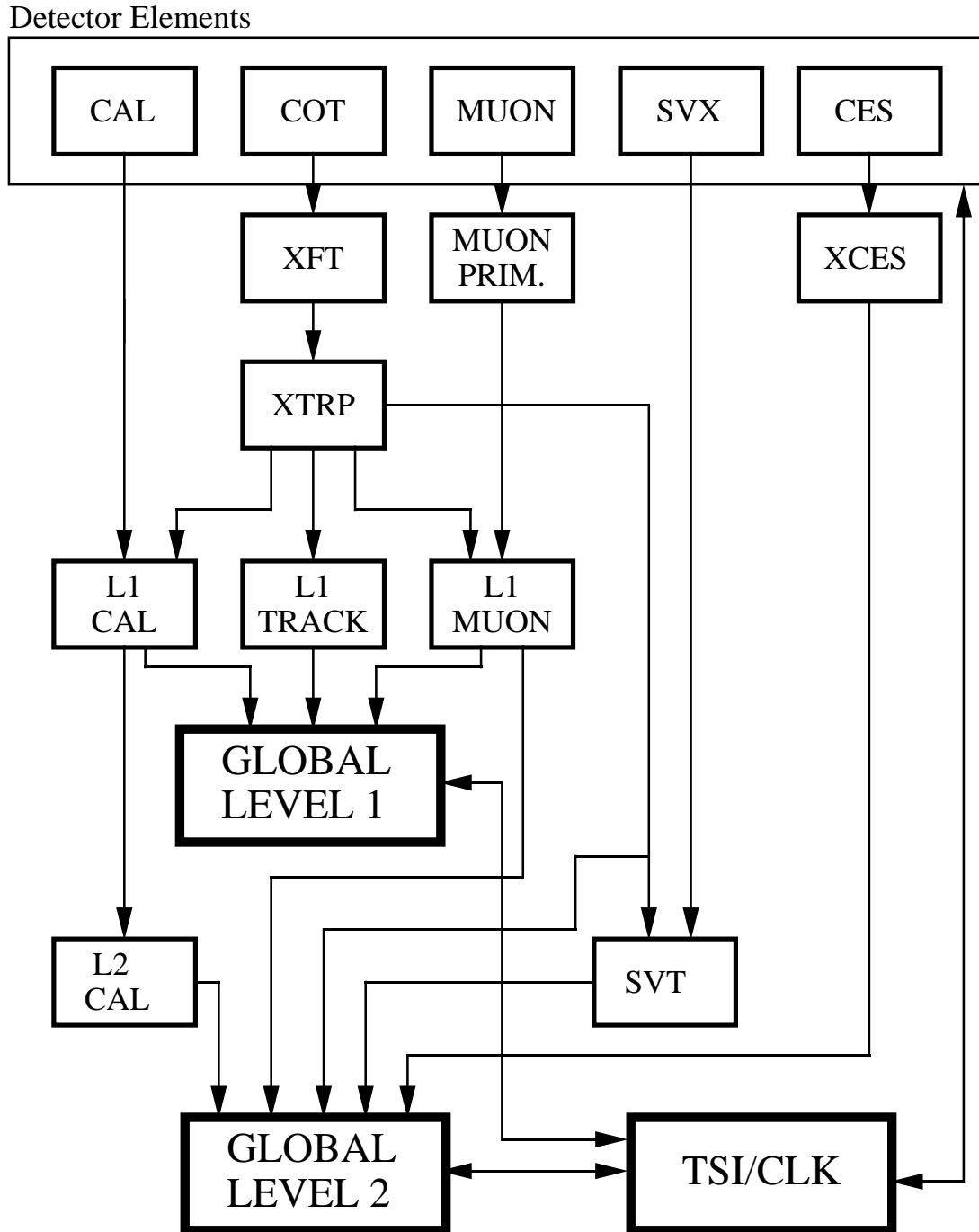


Figure 3.7: Block diagram of the CDF trigger system.

met is the entire detector read out. The digitized output from all detector components is collected and sent to the Event Builder, where the event fragments obtained from different subsystems are organized into an orderly sequence and fed to the Level 3 trigger.

Unlike Level 1 and Level 2 which must reach their decision in a very limited time and therefore are equipped with custom made electronics, Level 3 is implemented with a conventional PC computing farm. Almost every one of the roughly 300 CPUs is used as an event buffer, allowing a whole second to be allocated for a trigger decision. This means that at Level 3 the event undergoes a thorough, near-offline quality reconstruction. After reconstruction, the final trigger requirements are applied. These are satisfied for about 30 events per second. If accepted by the Level 3 trigger, the event gets written to a mass storage device (tape).

A set of requirements that an event has to fulfill at Level 1, Level 2, and Level 3 defines a trigger path. The CDF II trigger system implements about 100 trigger paths. An event will be accepted if it passes the criteria of any of these paths. The set of trigger paths used in this analysis is called the Two Track Trigger.

The Two Track Trigger path is optimized for finding charm and bottom hadrons decaying into hadronic final states. At Level 1, rough measurements of track transverse momenta are available. By requiring tracks above the transverse momentum threshold, most of the inelastic background is eliminated. At Level 2, the additional time available is used to incorporate the silicon vertex detector information to obtain an estimate of the track impact parameters. Requiring non-zero impact parameters ensures that tracks come from displaced vertices, that is, from decays of long-lived particles such as charm and bottom hadrons.

Parts of the CDF trigger and data acquisition system relevant to this analysis are

discussed below in greater detail. More detail can be found in References [21] and [24].

3.3.1 Level 1

The Level 1 is a synchronous system which takes two actions for every bunch crossing: it reads an event, and it makes the accept/reject decision for another, previously read event. The Level 1 decision is based on tracks in the central tracker, transverse energy in the calorimeters, and stubs in the muon chambers. The trigger uses rudimentary versions of these objects, which are made quickly without detailed reconstruction and are called primitives. To ensure the maximum speed, Level 1 uses custom designed hardware.

There are many algorithms (or, equivalently, individual triggers) at Level 1. Some of them combine the tracks primitives with the calorimeter energy or muon stubs to form electron, muon and jet objects, as shown by arrows in Figure 3.7. However, this ability to combine objects from different detector systems is rather limited, due to the strict time constraints imposed on Level 1. The purpose of various algorithms include looking for two high- p_T tracks, looking for a single high energy muon, looking for large missing E_T indicating a neutrino, *etc.*

The rate of events accepted by the Level 1 trigger is of the order of tens of kHz, roughly one hundred times smaller than the input rate of 2.5MHz.

EXtremely Fast Tracker (XFT)

The Two Track Trigger, like many other paths, uses the Level 1 eXtremely Fast Tracker system. The XFT identifies the track primitives in the $r - \phi$ view with $p_T > 1.5 \text{ GeV}/c$, using the four axial superlayers of the central tracker.

The functional diagram of the XFT is shown in Figure 3.8. The track identification is accomplished in two steps: first segment finding and then segment linking. In the

first step all tracker hits are classified as either prompt (drift time < 44 ns) or delayed ($44 \text{ ns} \leq \text{drift time} \leq 132$ ns). Then a set of binary masks - predefined patterns of prompt/delayed hits - is applied in order to find all segments compatible with a valid track passing through a given superlayer. A pixel is set for a successful segment match. The pixel represents the ϕ coordinate of the segment plus slope information in the outermost axial superlayers. The slope information is needed to identify the charge.

In the second, linking step, four pixels appearing to have come from the same track are identified, and based on these a crude estimate of the track parameters p_T and ϕ_6 is made (ϕ_6 is the angle of the transverse momentum vector at the sixth superlayer of the tracker, 106 cm away from the beamline.). Thus found tracks are reported to the EXTRaPolator unit (the XTRP, not used in this analysis), which extrapolates them to the other detector subsystems, such as calorimetry and muon chambers, and a copy of them is recorded for use by the Level 2 trigger.

More information on the XFT can be found in Reference [25]. For the purpose of this analysis, it is important to be aware of the thresholds: for an individual hit to be registered, the charge arriving on the tracker sense wire must be over a threshold. Moreover, for a set of hits to be considered as forming a track, their number must also be large enough.

3.3.2 Level 2

The Level 2 is an asynchronous system which processes events accepted by the Level 1 in time-ordered sequence. It uses Level 1 primitives and also additional data from the $r - \phi$ strips of the silicon vertex detector and the shower maximum detectors

XFT System Block Diagram

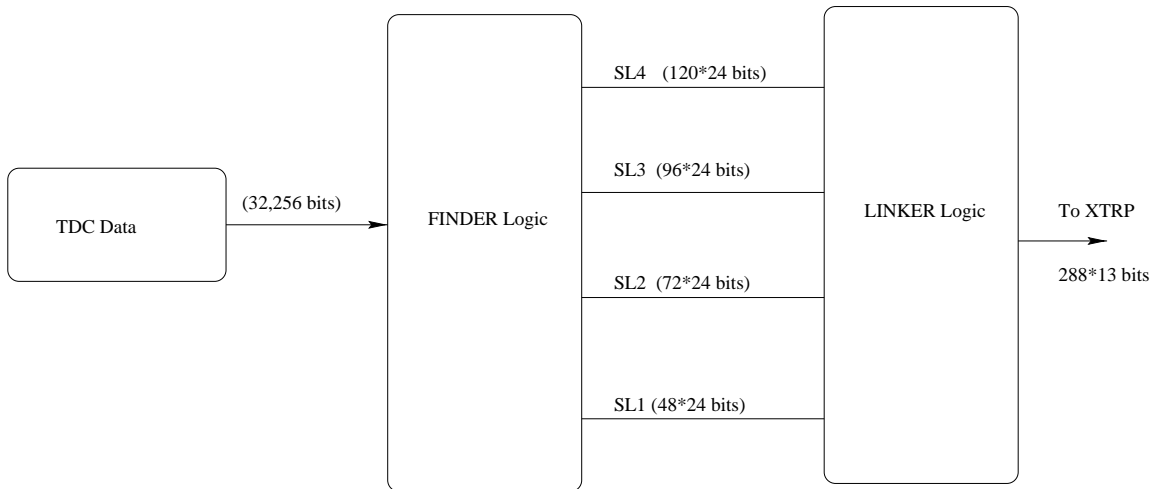


Figure 3.8: EXtra Fast Tracker functional diagram.

in the central calorimeter (Figure 3.7).

The Level2 algorithm path using the silicon tracker is called the Silicon Vertex Trigger, SVT, and is used to select events in this analysis. The architecture of the SVT is illustrated by the diagram in Figure 3.9. The SVT uses silicon vertex detector $r - \phi$ hits to extend the extremely fast tracker's tracks into the SVX volume. In this way it improves the XFT ϕ_0 and p_T resolutions. It also performs the measurement of impact parameter, d_0 . A sizable impact parameter indicates a displaced vertex, which is a powerful, clean signature of long lived particles.

As mentioned in Section 3.2.1, the silicon vertex detector is segmented into 12 wedges in azimuthal angle and three mechanical barrels in the z direction. The silicon vertex trigger makes use of this symmetry and performs separate tracking for each wedge and barrel. An SVT track starts with a two dimensional XFT track measurement called a seed, which is extrapolated into SVX volume to form a road.

Clusters of charge on the inner four $r - \phi$ layers of the wedge are searched for inside this road. If they are found, the silicon cluster information and the XFT segment information are fed into a linearized fitter which returns the measurements of p_T , ϕ_0 , and d_0 of the track.

As shown in the Figure 3.10, the track impact parameter resolution is about $35\mu\text{m}$, for tracks with $p_T > 2\text{ GeV}/c$. The width of the Gaussian fit to this distribution is about $47\mu\text{m}$, because it is a convolution of the intrinsic resolution of the SVT impact parameter measurement and the transverse profile of the beam region. The interaction region is roughly circular in the transverse plane and can be approximated by a Gaussian distribution with a width of roughly $35\mu\text{m}$. The intrinsic SVT resolution is then obtained by subtracting the beamline width in quadrature from the width of the impact parameter distribution.

For the Two Track Trigger, an event passes Level 2 selection if there is a track pair reconstructed in the silicon vertex trigger such that each track has $p_T > 2.0\text{ GeV}/c$ and $120\mu\text{m} < d_0 < 1\text{ mm}$. Some of the paths also require the tracks to be of the opposite charge. The vertex of the track pair has to have $L_{xy} > 200\mu\text{m}$ with respect to the beamline.

3.3.3 Event Builder and Level 3

If an event is accepted by the Level 2 trigger, the entire detector is read out, freeing slots in all of the detector buffers for the next event. The fragments of the just read event are put in order by the switch-based system known as the Event Builder. These event fragments are then channeled to the Level 3.

Level 3 is a farm of conventional PCs running a Linux operating system. The farm

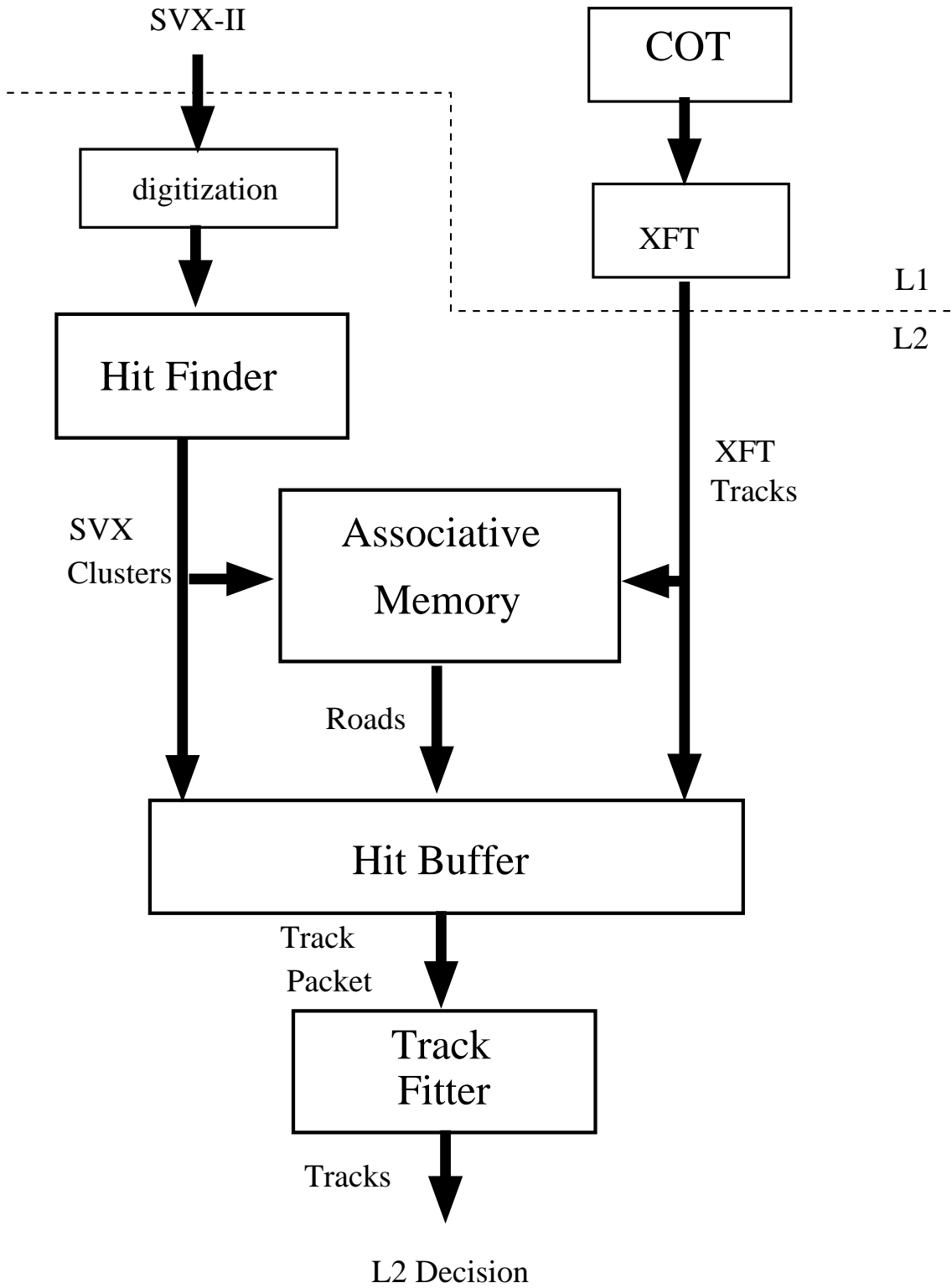


Figure 3.9: Block diagram of the SVT trigger.

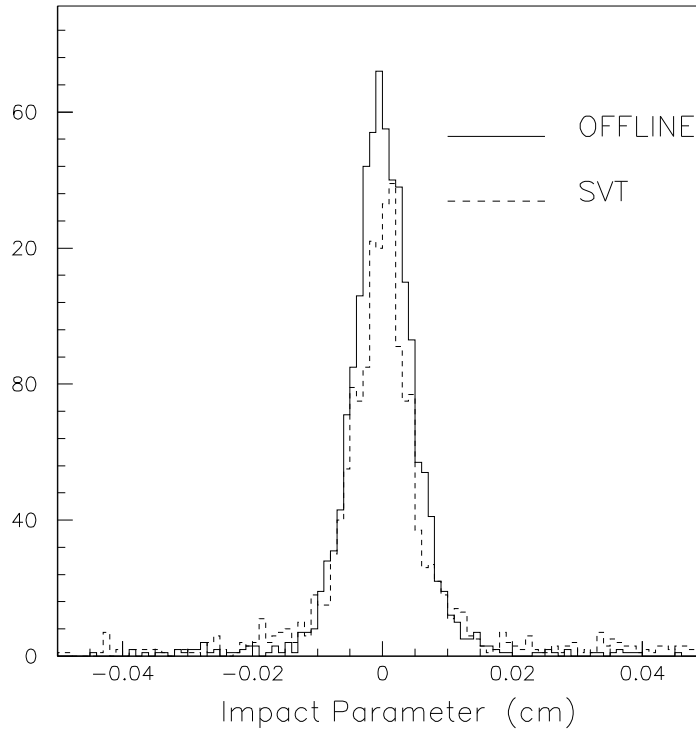


Figure 3.10: Distribution of impact parameters for SVT tracks and tracks produced by offline reconstruction for charged particles with $p_T > 2 \text{ GeV}/c$.

is split into a number of subfarms identical in architecture. Each subfarm consists of a head node and 12 to 16 processor nodes. Level 3 also contains several output nodes, each of which is shared by two subfarms.

The head node receives an ordered sequence of event fragments from the Event Builder. It then assembles them into a block of data known as an event record, which is suitable for analysis by the CDF software. From this point on, the event record is the sole source of information about any particular event.

Each event record is fed to one of the processor nodes of the subfarm, which then performs event reconstruction and applies final trigger requirements. At this stage,

Level3 uses the full detector information and improved resolution not available to the lower level triggers. If an event satisfies Level3 requirements, the event record is passed to the output node which then transfers it to mass storage.

Parallel processing of events by many nodes allows much more time to devote to any particular event, and therefore yields a more accurate trigger decision. Overall, the Level3 reduces the data volume by a factor of about ten, thus bringing the total event rate from 300 Hz down to about 30 Hz.

The data taking is divided into continuous periods of time called runs. These are usually a few to many hours long but cannot exceed duration of the accelerator store, which is typically a day or two. The detector configuration is kept constant during any given run, but can change from one run to another, possibly affecting the data being collected. Because of this, the Level3 stamps all the events with the run number, so that information about the configuration of the detector at the time of taking the event can be accessed from a database.

3.4 Detector Operation and Off-line Data Processing

The data flow from the Level3 is segmented into ten streams, denoted with letters from A to J, depending on the triggers each event satisfied. All streams are written to tape in real time as the data is being taken.

All subsequent data manipulations are referred to as off-line data handling. The most important of these is production, a process in which raw data banks are unpacked and physics objects suitable for analysis, such as tracks, vertices, electrons, muons,

jets, and alike are created. This is similar to processing by the Level 3 trigger but is done more thoroughly by applying the most up-to-date calibrations, such as the best measured beamline position.

The output of data production undergoes further classification. The ten data streams are split into compressed data sets, to be used directly in physics analyses. The compression is done by dropping those event objects which are not used by most analyses. While the uncompressed data sets are also available for analyses, compression greatly reduces necessary storage, enabling disk rather than tape storage. By allowing quicker access to physics objects, it also speeds up analyses. Data input is often the most time consuming part of analysis execution.

Occasionally, it is beneficial to reprocess part or all of the data with a newer version of the production program. Therefore, to fully specify the data used one has to add to the dataset name the production version used.

Chapter 4

Overview of the Measurement

This section gives a very brief overview of the measurement. We first cover some general issues that most high energy particle physics measurements are likely to face. We then go over the specific steps of this analysis.

4.1 General Issues of Data Analysis

To study properties of an elementary particle process, such as the probability of the D^+ meson decay into three pions, we need to select a collection of events that contain this process. This is not a trivial task, as the events containing the desired process are only a small fraction of the total data recorded by the detector. The desired type of event is referred to as signal, and all other events are called background. The signal, however, cannot be perfectly extracted. This is especially true at a hadron collider such as Tevatron, which has a large QCD background. Some amount of background will find its way into the sample of candidate events. A good measurement necessitates a good description of the background, in terms of physics variables such as mass,

impact parameter, proper lifetime, etc.

Too much background, relative to the signal, is likely to make the features of the signal indistinguishable. A major task of an analysis, then, is to separate the signal events from those of the background. This is done by choosing and applying an optimal set of selection criteria that discriminate between the two. The optimal signal selection does not necessarily mean eliminating or even minimizing all background. Rather, the optimal set of criteria is a set which minimizes the uncertainty of the signal parameters being extracted. Using overly tight selection criteria to reduce the amount of background will also lead to the elimination of some of the signal events and will thereby diminish the statistical power of the analysis. Additionally, once some amount of background is present, it may be beneficial to have more of it so that its properties can be correctly modeled.

Detector effects and related uncertainties present another issue common to most data analyses. We witness all physics events as they were captured by the detector. However, no detector is perfect. Detectors not only have finite resolutions, but also may give systematically distorted views of the events they register. These distortions happen on all levels of data processing. To understand and minimize them, all detector subsystems are calibrated and the data correspondingly corrected, starting from the lowest level of raw electronics signals up to the level of physics objects such as tracks of charged particles. By the time a high level analysis is being performed on the data, all gross imperfections have been taken out. Yet, more corrections for systematic effects are likely to be needed. If these corrections cannot be made, the effects must be estimated and included in the uncertainty of the measurement. The final measurements of the properties of particle processes are also subject to effects of the finite resolution of the detector subsystems.

One powerful tool used routinely for CDF data analyses is the Monte Carlo simulation of events of interest. For this measurement, the Monte Carlo is used to understand the detector response to the signal and background events, and to determine expected shapes of distributions of invariant masses and other variables. We generate Monte Carlo events using the current understanding of fundamental interactions and mechanics of a large number of processes. We next simulate the detector response to the Monte Carlo events, based on the detailed knowledge of the detector, including how accurately it detects elementary particle processes and measures their properties.

In the roadmap for this analysis presented below, we introduce the main ideas and issues discussed in this section: the optimal selection of signal and background, the understanding of the properties of the signal and the background from their Monte Carlo simulation, and the statistical analysis of the data distributions.

4.2 Roadmap for This Analysis

Recall that the goal of this analysis is to measure the relative branching ratio of decays of the D^+ meson into the three-body final states $\pi^-\pi^+\pi^+$ and $K^-\pi^+\pi^+$. Measuring a relative branching ratio has two distinct advantages over measuring the absolute branching fraction for the $D^+ \rightarrow \pi^-\pi^+\pi^+$ decay. First, we do not need to know the absolute production cross section of the decay. Second, many systematic uncertainties, for example those related to luminosity, trigger acceptance, reconstruction efficiencies, and alike, fully or partially cancel in the ratio, leaving a manageable set of uncertainties to be estimated.

We choose the $K\pi\pi$ channel for the denominator because of its high statistics

and kinematical similarity to the $\pi\pi\pi$ mode. From the ratio, we can get the absolute branching fraction of the $D^+ \rightarrow \pi^-\pi^+\pi^+$ decay from measurement of $D^+ \rightarrow K^-\pi^+\pi^+$ branching fraction performed elsewhere.

The branching ratio of the two modes is determined as follows:

$$\frac{BR(D^+ \rightarrow \pi^-\pi^+\pi^+)}{BR(D^+ \rightarrow K^-\pi^+\pi^+)} = \frac{N_{\pi^-\pi^+\pi^+}}{N_{K^-\pi^+\pi^+}} \cdot \frac{\varepsilon(K^-\pi^+\pi^+)}{\varepsilon(\pi^-\pi^+\pi^+)}. \quad (4.1)$$

Here, $N_{\pi\pi\pi/K\pi\pi}$ is the yield of the D^+ meson in the $\pi\pi\pi$ or $K\pi\pi$ channel, that is, the number of the decays found in the event sample after applying selection requirements. The relative efficiency, $\frac{\varepsilon(K\pi\pi)}{\varepsilon(\pi\pi\pi)}$, is the ratio of the probabilities for events of the two channels to pass selection criteria and candidate reconstruction. Thus, the task of this analysis is to measure three quantities: two candidate counts and a relative efficiency.

From the full CDF data sample, we derive two candidate samples: one with events containing $D^+ \rightarrow \pi^-\pi^+\pi^+$ candidates, and the other containing $D^+ \rightarrow K^-\pi^+\pi^+$ candidates. In both channels, a candidate is found by combining three good quality tracks which form a secondary vertex, that is, which come from the decay of the same particle. We require that at least two of these three tracks satisfied the trigger criteria. Kaon and pion masses are assigned to the particles based on their charge. For each decay sample, the invariant mass distribution of the candidates shows the signal peak and the contamination of the sample with background events. After applying a set of rather loose selection criteria (described below), a prominent peak is seen in the $D^+ \rightarrow K^-\pi^+\pi^+$ sample, with the signal to background ratio roughly 10:1 (Figure 7.1, left). In the $D^+ \rightarrow \pi^-\pi^+\pi^+$ sample, however, the same selection criteria yield significantly worse signal to background ratio, roughly 1:3 (Figure 7.1, right). This leads to the optimal selection criteria being chosen based on the $D^+ \rightarrow \pi^-\pi^+\pi^+$

channel. Optimal here refers to the ratio between background suppression, achieved better with tighter selection criteria, and retention of the signal, which increases the statistical power of the analysis. We find this optimal set of selection criteria by maximizing statistical significance, $\frac{S}{\sqrt{S+B}}$. Here, S is the expected number of signal events which we take from Monte Carlo, and B is the expected number of background events, which we extract from the data mass spectrum regions close to the signal region, called sidebands. The sidebands contain no signal events, but the background levels approximate those in the signal region. After arriving to the optimal selection for the $D^+ \rightarrow \pi^-\pi^+\pi^+$ channel, the criteria for the $D^+ \rightarrow K^-\pi^+\pi^+$ channel are chosen to be as similar as possible, in order for the systematic biases to cancel in the ratio of the event rates.

Upon applying the optimized selection criteria to our D^+ candidate samples, we obtain the mass distributions seen in Figure 7.5, where the signal is centered around D^+ mass and is roughly normally distributed. We model these mass distributions to extract the yields of the D^+ decays. The mass of the D^+ is well measured: 1869.3 ± 0.5 MeV ([8]). The small uncertainty of this measurement is negligible for our purposes. The finite width of the distributions visible in the plots, of the order of 5 - 10 MeV, is due to the finite precision of our detector, that is, it comes from the effects of the bell-shaped resolution function of the track measurement. In a perfectly calibrated detector, the resolution function is a perfect normal curve, and so is the shape of the mass distribution of a particle with a very small width. In a real-life detector, however, the resolution function has a complicated shape, composed of many gaussians with different widths. Consequently, the mass distributions of particles have bell-like shapes that can be described as convolutions of many gaussians. When modeling such a mass distribution, we aim to find the simplest function, that

is, the minimal number of gaussians, that would describe the shape well enough. In this measurement, the mass peaks of D^+ were satisfactorily described by a double gaussian curve centered on the mass of D^+ . Throughout this dissertation, $\sigma(D)$ refers to this finite width of the D^+ mass distribution; specifically, it is the width of the narrower of the two gaussians, which is sometimes called the core gaussian.

To derive the double gaussian function that describes the signal shape, we employ a realistic signal Monte Carlo generated for this analysis and used in signal optimization and elsewhere. We take care to also simulate the events with final state radiation. Final state radiation occurs when, immediately after its creation, one of the quarks radiates a photon, adding it to the decay final state. Because the photon does not get reconstructed, there is an energy loss to the system, and the reconstructed mass of the candidate is slightly lower than it would otherwise be. By simulating the final state radiation effects, we account for a non-negligible fraction of candidates positioned in the low mass tail of the signal distribution.

In addition to the signal peak, the $D^+ \rightarrow \pi^-\pi^+\pi^+$ and $D^+ \rightarrow K^-\pi^+\pi^+$ mass distributions contain combinatorial background and reflections. (The mass distributions generally contain other fully reconstructed particles, but we suppress them in this analysis, except for the D_s^+ decaying to the $\pi^-\pi^+\pi^+$ state.) Because it is composed of a random collection of particle tracks, combinatorial background has a simple shape that can usually be approximated by linear, quadratic, or exponential function. In this measurement, the combinatorial background shape is well described by the second order polynomial. Reflections are often defined differently by different authors; here we call reflections any mass spectrum structures left by misreconstructed decays. Misreconstruction can result from mass misassignments, in which case a particle and the corresponding track are assigned the mass of a different particle, causing the

energy of the system to be misreconstructed and leaving a bump-like mass shape. In this case, though the structure does not look like a normally distributed particle mass peak, the events cluster together. Reflections can also come from the partially reconstructed decays, in which one or more particles escaped detection, causing the reconstructed mass to be below the actual mass of the system. The bump-like shapes left by partially reconstructed decays are more flat and spread out than those of mass misassignments, and typically have long tails on the lower mass side of the distribution. Because reflections leave specific, predictable shapes that can be modeled, we produce Monte Carlo simulations of them and incorporate their shapes into our background shape function.

In the end, the mass distributions of the data are fitted using the sum of the signal, reflections, and combinatorial background templates derived from the Monte Carlo, and the yields are extracted as parameters of the resulting fit.

The efficiencies of $\pi^-\pi^+\pi^+$ and $K^-\pi^+\pi^+$ channels have many common factors. Since these cancel in the relative branching ratio, we only need to worry about those that do not, that is, about the aspects of data collection and reconstruction that differ for the two channels. Most important among these are:

- Dalitz structure of the decays. The efficiency is not uniform across Dalitz space, but this non-uniformity is the same for both channels, except for the different Dalitz area. However, the two decays have different resonant structures, enhancing some Dalitz regions and suppressing others, resulting in significant differences in overall efficiencies.
- Difference in the XFT efficiency of kaons and pions. Due to their different ionizing properties, that is, different shape of their Bethe-Bloch curves, pions and

kaons have different probabilities of passing the tracker hit thresholds and producing enough hits to form trigger tracks. Pions ionize more and are therefore slightly more likely to produce a hit. Their trigger efficiency is larger than that of kaons. Thus, the $\pi\pi\pi$ and $K\pi\pi$ decays differ in the overall reconstruction efficiency.

- Interactions with detector material. Strong interactions with the detector material of the four particle species involved (π^+ , π^- , K^+ , K^-) have different cross sections. This is due to their quark content; while ordinary matter, including that of the CDF detector, is mostly composed of protons (uud) and neutrons (udd), positive pions have $u\bar{d}$ configuration, and positive kaons $u\bar{s}$. The strange quark of the kaon will lower the cross section of its interactions with the detector material, compared to that of the pion. Among kaons, the negatively charged kaon, with its \bar{u} valence quark, will interact more readily with the matter than the positively charged one. These effects add up to a complex difference in interaction rates, which affects our data.

With the abundance of charm events provided by the two track trigger, this analysis is a high statistics one. The biggest challenge of such analysis usually comes from subtle detector and physics related effects which a lower statistics analysis may be able to disregard but a high statistics one cannot. In this analysis, modeling of the reflections-rich background is one such challenge. Another, typical one is the accurate estimate of all the relevant systematic uncertainties. The chapters that follow demonstrate how these challenges were successfully overcome.

Chapter 5

Data Samples

This section describes the data sample used for this measurement. Here we examine the general data processing and selection of good quality data samples at the level of runs, run periods, and trigger paths, leaving the event selection and reconstruction details specific to this analysis to subsequent sections.

5.1 Data Sample

This analysis uses the data collected by the CDF detector between February 2002 and August 2003. The integrated luminosity of these data is 193 pb^{-1} . Out of the multitude of data collected with different triggers, the two track trigger data are what we use for this measurement.

CDF detector is a complex apparatus that has imperfections and time dependencies. In addition, p and \bar{p} beam properties vary in time. Therefore, special attention has to be paid to selecting the data taken during maximally stable and optimal operation of the Tevatron collider and the detector.

As will be seen below, this analysis goes to length to understand time dependencies and imperfections of the data. For a high-statistics measurement, this is crucial, because such factors may cause systematic bias in the measurement. Monte Carlo simulation has to take into account all of these factors.

The sub-sections below describe the selection of good quality runs, uniform periods of data-taking as well as the composition of the analyzed dataset with regard to the two track trigger paths.

5.1.1 Good Runs

The dataset we analyze contains runs of varying quality. Ordinarily, the requirements for a run to be part of a dataset are rather loose. Only gross problems with the detector or the beam cause a run to be completely discarded. For different physics measurements, different run selections are appropriate. In this high statistics analysis only very good quality data are accepted.

There are several important criteria in selecting good data. First, the operating conditions of each subdetector have to be homogeneous over the time of the run. This means, for example, no significant variations in high voltage or in trigger rates. Second, all relevant subsystems have to be on, operating at adequate capacity. For example, data taken with XFT not working, or with several layers of SVX switched off are not good data for the purposes of this analysis. The concept of good runs allows us to remove inadequate data from a dataset. Good run criteria are established by the CDF data validation group. A run is marked as good if the people operating the detector, offline production operators, and subdetector experts all confirm the good quality of the data.

In practice, the people on data-taking duty and subdetector experts mark runs as good or bad by setting the appropriate bits in the CDF-II Run Database [26].

Runs during which there are problems in the detector setup are stopped as soon as the problems are discovered, so a run being short is the first indication of problems. Therefore, a run is accepted only if there are 100 million live Tevatron clock cycles, 10000 Level 1 accepts, 1000 Level 2 accepts, and at least 1 nb^{-1} of integrated luminosity in the run. Any run containing less data was most likely aborted because of technical problems with the detector setup.

The person in charge of data acquisition during the taking of the run confirms that no temporary, undocumented, or test trigger tables were used in the gathering of the data, and the offline shift crew members confirm that the data gathered during the run has been sent through offline production without problems. For the run to be used, the high voltage for the Cherenkov Luminosity Counters must be on during the run, and the luminosity and beam monitor plots must appear sound. This guarantees good quality of the luminosity measurement. The high voltage must also be on for the silicon vertex detector.

The trigger-related bits are set if the Level 1 and Level 2 trigger monitoring plots agree with the templates provided to the shift crew. At the Level 3, the rate of SVX data corruption errors must be less than 1% and the run number must be correctly assigned. The SVT online beam position subtraction must have been done correctly, and the SVT occupancy must be within limits set by the experts. Additionally, the D^0 and D^{*+} yields should be within expected range. Finally, the integrated luminosity of the run has to be larger than 10 nb^{-1} , and the fraction of bad COT channels has to be less than 1%. The first condition tightens the run length requirement, and the second guarantees good COT performance for tracking.

After imposing these good run requirements, the data we use for this measurement amounts to about 193 pb^{-1} of integrated luminosity.

5.1.2 Data Taking Periods

During the time our data was collected, the detector and trigger configuration went through a number of changes. These changes naturally divide our data into seven discrete periods. Table 5.1 describes the periods and their luminosities.

first run	last run	luminosity	change that occurred <i>after</i> this period
138809	142202	4.0 pb^{-1}	April 1, 2002 silicon accident
144013	151845	17.7 pb^{-1}	Start of dynamic prescale
151868	152625	6.9 pb^{-1}	Change from 2-miss to 1-miss XFT
152634	156487	44.7 pb^{-1}	January 2003 shutdown
158821	163113	48.0 pb^{-1}	Start selection of SVX tracks at L3
163117	164303	5.4 pb^{-1}	Switching from SVT 4/4 to 4/5
164304	168889	66.3 pb^{-1}	August 2003 shutdown

Table 5.1: Discrete data periods and corresponding luminosities, as defined by detector and trigger configuration changes. The luminosity is approximate, calculated with the good run script.

The end of the first period of data-taking is marked by an accident on March 30, 2002 when Tevatron experienced a glitch and the silicon tracker received a large dose of radiation. As a consequence, 6 of its 360 ladders were damaged and switched off from that point on. Running with some missing ladders in the silicon tracker, but with otherwise unchanged conditions, continued until run 151,868 when dynamic prescales were introduced. We explain the scheme of dynamic prescales later, in Section 5.1.3. Here it should suffice to note that dynamic prescaling changes the relative fractions of different trigger paths present in the sample.

The next change in the trigger system, and therefore the next boundary of the run

periods, is defined by a change in the XFT-trigger criteria. From the beginning of the Run IIa, the XFT trigger required that each of the four track segments from the four axial superlayers, used in the extra fast track reconstruction, have 10 hit wires out of 12 possible. In October 2002 it was decided that it is beneficial to increase purity of the tracks XFT finds by increasing the requirement to 11 hits out of 12 possible, as the efficiency remains sufficiently high. This change in XFT is known as transition from the 2-miss to the 1-miss configuration.

In January 2003 and August 2003, the Tevatron was shut down for over a month, and extensive repair work was done on the CDF detector. Many failed channels were repaired in many sub-detectors. In the process, the alignment of the detector has changed. The changes in both the live channels and the alignment warrant marking the shutdown as a boundary between the stable run periods.

Since May 2003 the reconstruction of stand-alone SVX tracks in software became sufficiently evolved and fast for it to be included into the online Level 3 trigger. Level 3 SVX stand-alone tracks are better quality tracks than the SVT ones, and adding Level 3 requirements for such tracks allowed reduction in the volume of data in track trigger paths by factor of two while keeping the inefficiency for heavy flavor events at the level of $< 5\%$.

Until June 2003, the SVT triggers required four hits in four SVX layers. The trigger logic was upgraded to include the fifth SVX layer and subsequently required four hits in the five layers. This upgrade greatly increased the efficiency of SVT track reconstruction and consequently the trigger efficiency.

All of the listed changes caused significant change in running conditions. In subsequent analysis of the data as well as in the generation and analysis of Monte Carlo, these conditions are properly tracked and reproduced.

5.1.3 B_CHARM Trigger Paths

The dataset on which this measurement is performed contains data collected through three hadronic trigger paths collectively known as the B_CHARM paths. The paths are: B_CHARM (referred to as Scenario A), B_CHARM_LOWPT and B_CHARM_HIGHPT. Each of these three trigger paths has specific requirements at trigger Level 1, 2 and 3, as listed in Table 5.2.

The Level 1 trigger uses EXtremely Fast Tracker (XFT) to preselect two candidate tracks, each with track segments reconstructed on at least four axial superlayers. These tracks are of low quality and high parameter uncertainties, due to the limited time available for the Level 1 decision. Physics selection is nevertheless possible, and requirements are imposed on the track transverse momenta, including their algebraic sum, and the angle between tracks.

The Level 2 uses Silicon Vertex Trigger. The SVT electronics does fast track reconstruction based on the hits found in SVX. These SVT tracks are further matched to the XFT tracks, and only the matched tracks are considered as the candidates for the Level 2 trigger tracks. The tracks are fitted to a vertex, which has to be of good enough fit quality ($\chi^2 < 25$) in order to be accepted. At the Level 2, the track requirements of Level 1 are reapplied because the parameters of the Level 2 tracks are measured with a significantly better precision, and some amount of background can be rejected by applying the same requirements on these better quality tracks. Finally, the tracks at Level 2 must be displaced with respect to the primary vertex. This requirement favors products of heavy flavor decays. The requirements on the track impact parameter d_0 with respect to the primary vertex in the $r - \phi$ plane are imposed.

At Level 3, the requirements of Level 2 trigger are reapplied using Level 3-quality tracks. Also, a track quality constraint is placed on the z coordinate distance between the drift chamber track and the matching silicon stand-alone track, measured at the distance of closest approach in the transverse plane.

For our purposes, the most important differences between the trigger paths are that of charge and the track transverse momenta. The B_CHARM_LOWPT path, unlike Scenario A and B_CHARM_HIGHPT, allows same charge as well as opposite charge track pairs. Furthermore, its track transverse momenta requirements are the loosest. Both low P_T and Scenario A, but not high p_T , are dynamically prescaled.

	Level	B_CHARM_HIGHPT	B_CHARM	B_CHARM_LOWPT
p_T	L1	$\geq 2.5 \text{ GeV}$	$\geq 2.0 \text{ GeV}$	$\geq 2.0 \text{ GeV}$
$\sum p_T$	L1	$\geq 6.5 \text{ GeV}$	$\geq 5.5 \text{ GeV}$	—
charge product	L1	-1	-1	—
$\delta\varphi_0$	L2	$\geq 2^\circ$	$\geq 2^\circ$	$\geq 2^\circ$
$\delta\varphi_0$	L2	$\leq 90^\circ$	$\leq 90^\circ$	$\leq 90^\circ$
$ d_0 $	L2	$\geq 120 \mu\text{m}$	$\geq 120 \mu\text{m}$	$\geq 120 \mu\text{m}$
$ d_0 $	L3	$\geq 80 \mu\text{m}$	$\geq 80 \mu\text{m}$	$\geq 80 \mu\text{m}$
$ d_0 $	L2	$\leq 1000 \mu\text{m}$	$\leq 1000 \mu\text{m}$	$\leq 1000 \mu\text{m}$
L_{xy}	L2	$\geq 200 \mu\text{m}$	$\geq 200 \mu\text{m}$	$\geq 200 \mu\text{m}$

Table 5.2: Definition of the trigger requirements applied to three different versions of the B_CHARM trigger. The column 'Level' indicates the trigger level at which this requirement is applied for the first time. In general, trigger requirements at Level 1 and Level 2 are repeated at higher trigger levels with the same values. An exception is made for the requirement on the impact parameter, which is looser at Level 3 than at Level 2.

Dynamic Prescaling of Triggers

In order to limit the rate of some triggers, a procedure called prescaling is applied. A trigger prescaled with a factor N will only pass one of every N events which satisfy

the trigger conditions. For some triggers, such as those used in this analysis, the prescale factor is set dynamically during run time, based on the available trigger bandwidth and collision luminosity. First, the triggers are prescaled down at the beginning of the store. This is done so that the rates of the triggers with looser requirements will not be unmanageably high. As the luminosity drops over the course of a store, the unprescaled trigger rates drop over time. Dynamically prescaled trigger rates get accordingly adjusted, thus utilizing trigger bandwidth no longer needed by unprescaled triggers.

The only unprescaled trigger path used for this analysis is the `B_CHARM_HIGHPT`. Its more restrictive requirements, such as that to have two tracks of the opposite charge and of higher track momenta than the other two paths, result in lower yield of events. The `B_CHARM` and `B_CHARM_LOWPT` paths share the remaining trigger bandwidth, and both are dynamically prescaled. The `B_CHARM` path has more restrictive requirements and hence lower prescale factors in comparison to the `B_CHARM_LOWPT` which has the loosest requirements and therefore has to be prescaled the most.

The knowledge of prescale factors with which the data was taken is necessary to prepare proper Monte Carlo samples. We determine the values of prescale factors from the data, by comparing D^+ meson yields in unprescaled and prescaled samples. The procedure is described in Section 9.1.

Chapter 6

Monte Carlo Samples

We start this chapter with the description of Monte Carlo samples generated for this measurement. The samples corresponding to signal help us model the signal shape. As for background, in addition to the combinatorial background (mass distribution coming from the random combinations of tracks from the event record), the reconstructed mass spectra contain rich reflection structures. To get the correct count of the D^+ yields, we need to model these structures. Using the Monte Carlo samples, we study background shapes and develop the fitting framework to extract the signal yields.

We also use Monte Carlo simulation to measure efficiencies of signal extraction, but these procedures are described in the following chapter. For now, we discuss generation of Monte Carlo samples that describe our data, modeling the signal and background, and using the model to get the yields ratio, $N_{\pi\pi\pi}/N_{K\pi\pi}$.

6.1 Monte Carlo Samples

Use of Monte Carlo event simulation has for a long time been commonplace in high energy particle physics. The complexity of detectors and particle interactions make it impractical or impossible to analytically derive distributions of quantities, and numerical procedures are used instead. Monte Carlo simulations are especially useful for studies of small effects in samples with large background, or for events whose origin is difficult to determine.

Throughout this data analysis, we use samples of Monte Carlo events that pass the full detector and trigger simulation. In addition to the signal modes, we use the inclusive samples of D^+ , D_s^+ , D^* , orbitally excited charm, and B hadron samples to derive templates for background mass shapes.

The key components of the Monte Carlo simulations are:

- generation of the D^+ meson and its decay, including quark production mechanism, parton fragmentation, decay branching fractions, and D^+ decay kinematics,
- simulation of detector response to D^+ decays, and simulation of the trigger, and
- reconstruction of the physics objects of the event.

In the above list, the first bullet component rests on theoretical knowledge, and the latter two depend on the knowledge of the detector. Decay branching fractions used in the simulations come from recent measurements and theoretical predictions.

6.1.1 D^+ Production and Decay

When producing Monte Carlo signal for the exclusive reconstruction analysis, we can limit ourselves to simulating only the D^+ meson candidates. By performing sideband subtraction of the data mass spectrum, we can plot and compare properties of the D^+ decay to those of the Monte Carlo simulation. To further simplify matters, the production mechanism and fragmentation process can be ignored, as long as the correct transverse momentum spectra and angular distributions of the tracks are produced. The remaining decay characteristics are in general well reproduced by commonly used decay programs, such as the BGenerator [27], used here.

We use BGenerator to create both charm and bottom particles. BGenerator is based on next-to-leading order calculations. It generates bottom and charm quarks as requested, based on the measured transverse momentum and angular distributions spectra. The minimum p_T is $4.5 \text{ GeV}/c$ and the rapidity range $|y| \leq 1.3$. The ϕ distribution is, of course, uniform. The fragmentation is implemented using Peterson fragmentation function [28]. Recently, more current fragmentation models have become available, but this is not critical to our analysis. BGenerator only produces bottom and charm hadrons; no fragmentation products or proton remnants are present.

The charm and bottom particles are decayed with the EvtGen package [29]. The signal modes are decayed uniformly in phase-space. This allows us to reweigh the events at a later stage according to any Dalitz structure model.

6.1.2 Detector Simulation, Trigger Simulation, and Event Reconstruction

Detector simulation is divided into simulation of the trigger and simulation of the rest of the detector that gives physics objects such as tracks and vertices. The detector geometry and the behavior of the active components of the detector are simulated using the GEANT [30] framework. GEANT allows us to model the detector response at the hit level. This means that we simulate the energy deposition in every active and passive detector component. We also simulate the data acquisition system's response to the active detector components. The output of the simulation mimics the real data structure. This makes it possible to apply the standard data reconstruction program directly to the simulation output.

In its simplest form, the simulation models the detector functions under ideal operating conditions, including all subsystems operating on the prescribed high voltage and the electronics responding to the traversing particles according to the design. But in reality, things do not always function this way. Real data include time dependent inefficiencies, electronic noise, and effects from malfunctioning detector parts. In particular, fractions of the silicon tracker have been off temporarily or permanently. The parameters of the trigger system have evolved over time. The position of the beams with respect to the detector is known to a finite precision and varies with time.

To account for these imperfections, we perform what is known as realistic Monte Carlo simulation. The realistic simulation keeps track of these operational irregularities. It divides the data taking period into sub-periods during which the detector performance is constant. This includes the parameters of the trigger at Level 1 and Level 2, position of the beamline, the silicon detector conditions and alignment.

Because there have been occasional glitches in the various detector systems and these are not simulated, only those runs having reproducible conditions have been selected. For more information about the good runs, refer to Section 5.1.1.

The output of the `BGenerator` package is run through four executables: the first one is responsible for the `GEANT` simulation of the detector response, the second performs the trigger simulation, the third processes the Monte Carlo output in a way identical to production farm processing; and the last one is the same reconstruction executable that we use for data.

To save data processing time, before simulating the detector response we prefilter events based on the information stored in the `HEPG` and `MVTX` banks. The `HEPG` bank contains information about all the particles, that is, complete decay chain, of each event. The events are generated at the coordinate center of the detector, for simplicity. The z position of the primary vertex is then “smeared”, that is, a realistic, non-zero position is assigned to each event according to the appropriate probability function. These primary vertex positions are stored in the `MVTX` bank. In addition to the prefiltering on particle content and primary information, we also impose requirements similar to the `B_CHARM_LOWPT` trigger and minimal analysis requirements:

- At least three tracks with $p_T \geq 0.49 \text{ GeV}/c$, $|z_0| \leq 50 \text{ cm}$, exit radius $\geq 132 \text{ cm}$.
- At least two tracks with $p_T \geq 1.84 \text{ GeV}/c$, $|d_0| \geq 60 \mu\text{m}$, $|z_0| \leq 50 \text{ cm}$, exit radius $\geq 132 \text{ cm}$.

After the detector simulation and the trigger emulation, we require of events to have two SVT tracks with $p_T \geq 2 \text{ GeV}/c$ and $120 \mu\text{m} \leq |d_0| \leq 1000 \mu\text{m}$. All of our Monte Carlo samples are stored on tape, available for use in other CDF data analyses.

mode	generated	on tape
$D^+ \rightarrow K^- \pi^+ \pi^+$	5×10^7	556,939
$D^+ \rightarrow \pi^- \pi^+ \pi^+$	5×10^7	547,342
inclusive D^*	1×10^9	817,104
inclusive D_s	5×10^8	330,791
inclusive B	2×10^8	480,746
inclusive B	3×10^8	710,640
inclusive D^+	2×10^8	445,664
inclusive D^+	2×10^8	470,795
inclusive D^+	2×10^8	496,759
inclusive $D_2^{*+} \rightarrow D^{(*)0} \pi^+$	5×10^8	272,549
inclusive $D_2^{*0} \rightarrow D^{(*)+} \pi^-$	3×10^8	341,613
inclusive $D_1^+ \rightarrow D^{*0} \pi^+$	5×10^8	261,067
inclusive $D_1^0 \rightarrow D^{*+} \pi^-$	5×10^8	302,932
$D^+ \rightarrow K^- \pi^+ \pi^+$ photos	1×10^8	1,108,935
$D^+ \rightarrow \pi^- \pi^+ \pi^+$ photos	1×10^8	1,084,272

Table 6.1: Monte Carlo samples used for this analysis. For the excited charm states the decays are forced to have a charged pion, but the charm states themselves are decayed inclusively.

Throughout this analysis, we reweight the Monte Carlo events several times to account for various effects that are not well reproduced by the simulation. These effects include the proper prescale factors for different trigger paths (Section 9.1), XFT trigger effects that discriminate between kaons and pions (Section 9.3), lifetime of the D^+ meson (Section 9.4), and discrepancies between data and Monte Carlo D^+ transverse momentum spectra. Because these effects are relevant for the measurement of the relative efficiency, but not for signal extraction, we leave their detailed descriptions for later (Chapter 9). We account for the Dalitz structure of the signal modes next (Section 6.2). Of all effects that are not properly simulated in Monte Carlo, it has the biggest potential of affecting the signal mass shape and therefore the candidate yields.

6.2 Dalitz Structure of the Signal Modes

The default B -decay package in CDF, called EvtGen, contains models for the resonant substructure of our signal modes. However, the $D^+ \rightarrow K^- \pi^+ \pi^+$ model is based on the E691 measurement [31] made with only $\approx 4 \times 10^3$ signal events. The EvtGen decay model for $D^+ \rightarrow \pi^- \pi^+ \pi^+$ includes a non-resonant component and a contribution from $D^+ \rightarrow \rho^0 \pi^+$ decays, but does not take into account the relative phase shift between the two, nor the contribution from other resonances.

We therefore opt to generate the events flat in phase-space, and reweight them according to a better model. The E791 experiment published a Dalitz analysis of the $D^+ \rightarrow K^- \pi^+ \pi^+$ mode based on $\approx 15 \times 10^3$ decays [32] and also a Dalitz analysis of the $D^+ \rightarrow \pi^- \pi^+ \pi^+$ mode based on $\approx 1.2 \times 10^3$ decays [7]. To avoid extensive studies associated with complete Dalitz analysis of our data, we use the E791 results in the following way: we perform the two dimensional fit of the Dalitz plots of our data, but use the resonances (masses and widths) from E791 results. We use the data fit results to reweight the Monte Carlo. We now briefly describe the E791 results, and the way we use them.

In parametrization of the resonant structure, the E791 papers apply Blatt-Weisskopf penetration factors, however, we found that the effect of these are small and can be ignored. We use the tables of a_n (resonant amplitudes) and δ_n (resonant phases) listed in the E791 papers to reproduce their models, and to verify the result by reproducing the fit-fraction, f_n , defined by:

$$f_n = \frac{\int |a_n A_n(m_{12}^2, m_{13}^2)|^2 dm_{12}^2 dm_{13}^2}{\int \Gamma(m_{12}^2, m_{13}^2) dm_{12}^2 dm_{13}^2} \quad (6.1)$$

The E791 papers report the normalized amplitude a'_n :

$$a'_n = \frac{a_n}{\sqrt{\int |A_n(m_{12}^2, m_{13}^2)|^2 dm_{12}^2 dm_{13}^2}} \quad (6.2)$$

For the $D^+ \rightarrow K^- \pi^+ \pi^+$ decay, E791 proposes three fit models, indicated as models A, B, and C. In Figure 6.3 we compare the projections of the invariant mass between the E791 models and our data, after selection and background subtraction.

For the $D^+ \rightarrow \pi^- \pi^+ \pi^+$ decay, E791 proposes two fit models, indicated as models 1 and 2. In Figure 6.4, we compare the projections of the invariant mass between the E791 models and our data.

We find that none of the models describes the structure seen in the data well. Therefore, instead of simply using the E791 models for modeling the Dalitz structure, we use CDF data to perform the two dimensional fits using the resonances that E791 found. Figures 6.2 and 6.1 show the results of these fits, used throughout this analysis.

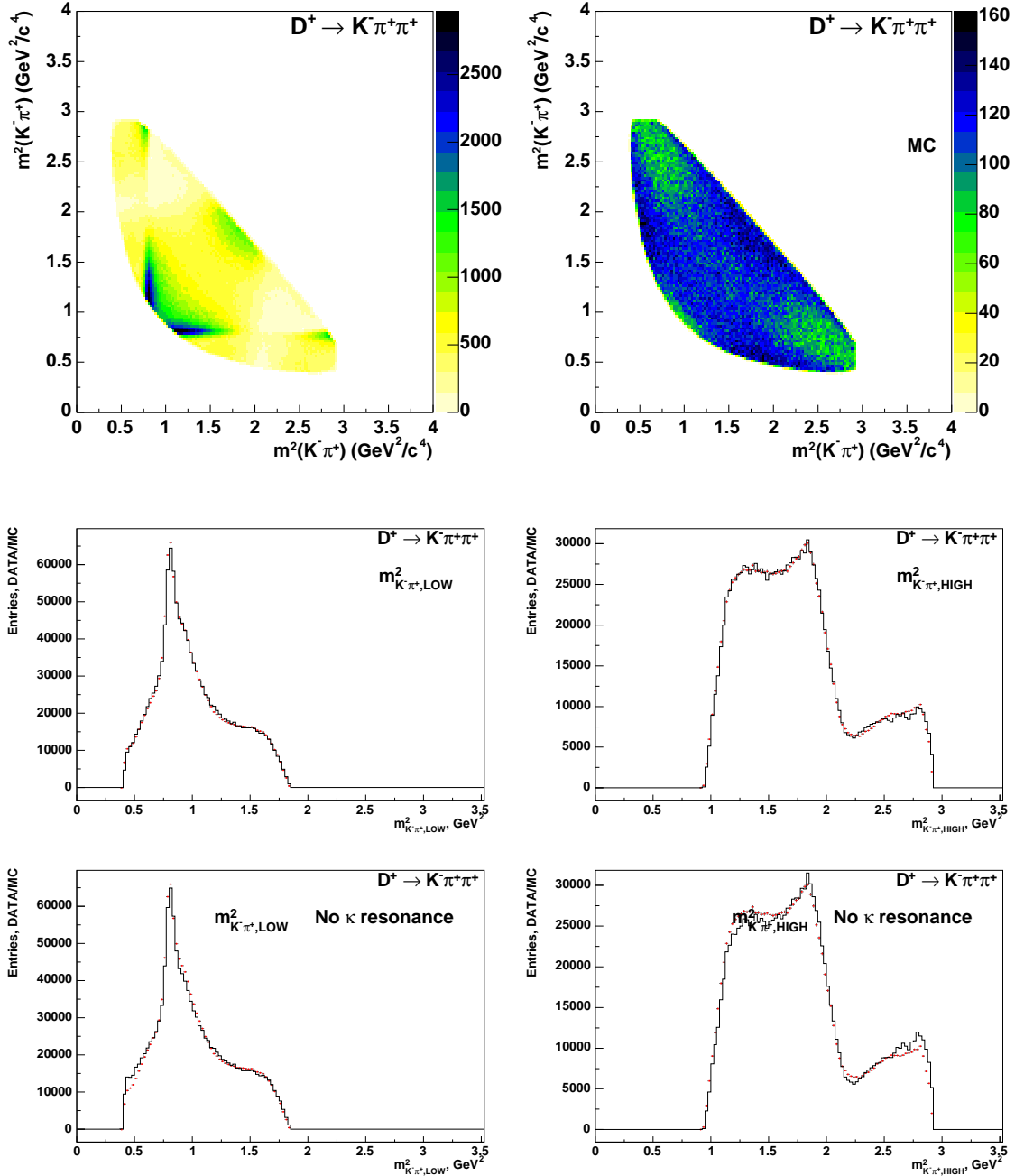


Figure 6.1: Dalitz plots of the $D^+ \rightarrow K^- \pi^+ \pi^+$ decay made with our data (top left); Monte Carlo (top right) is generated flat and reweighted using E791 resonances fitted to the data. The agreement between data (points with error bars) and Monte Carlo (histogram) after reweighting can be seen on the plots of the low and high invariant masses, on the bottom.

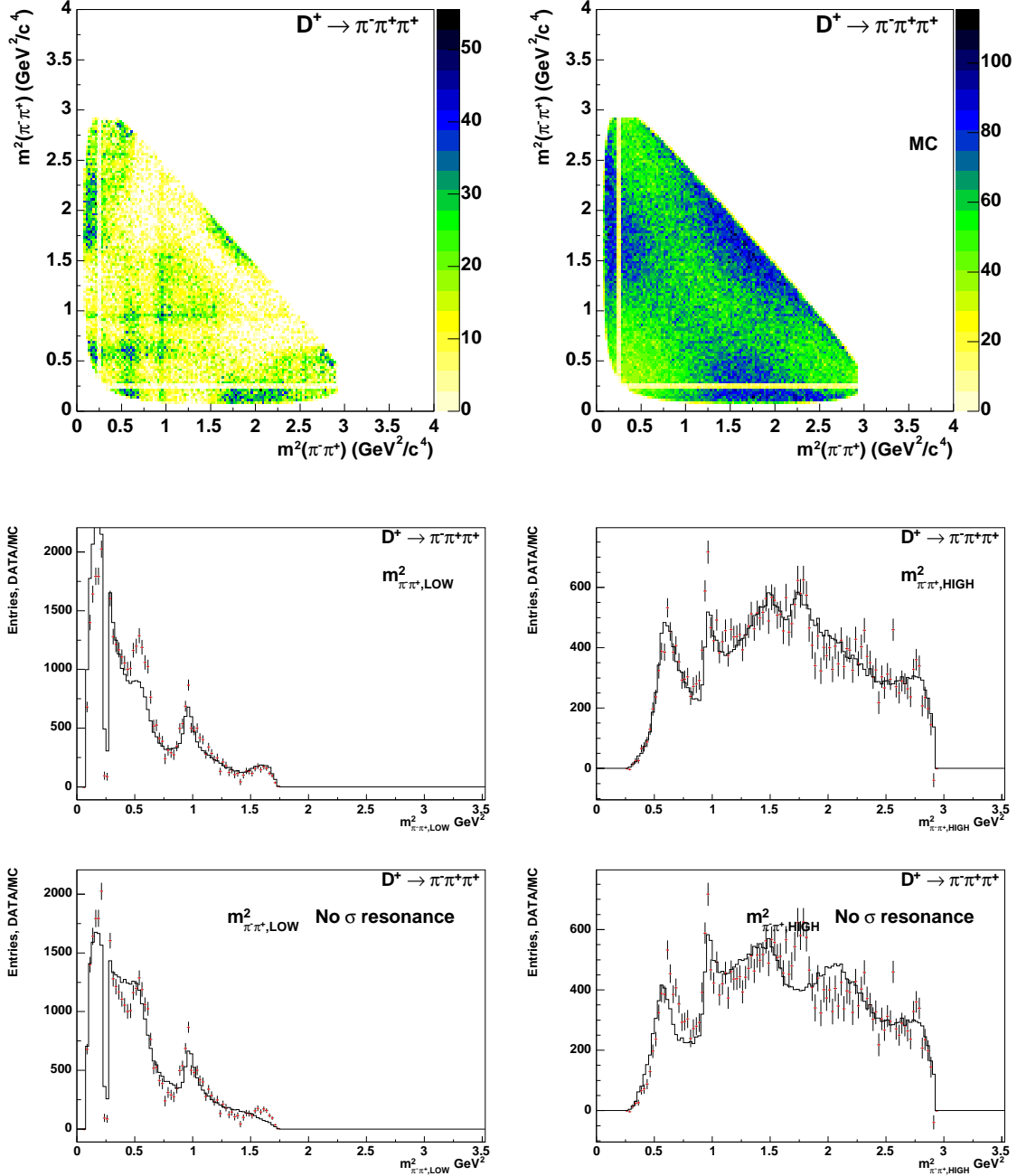


Figure 6.2: Dalitz plots of the $D^+ \rightarrow \pi^- \pi^+ \pi^+$ decay: data (top left) and Monte Carlo (top right). Monte Carlo is generated flat and reweighted using E791 resonances fitted to our data. Plots of the low (bottom left) and high (bottom right) invariant masses show the agreement between data (points with error bars) and Monte Carlo (histogram) after reweighting. The high mass corners are cut off due to a kinematic constraint to suppress background, introduced in next Chapter. Similarly, the low mass band cut-out is due to a constraint to suppress K_S two-body decays.

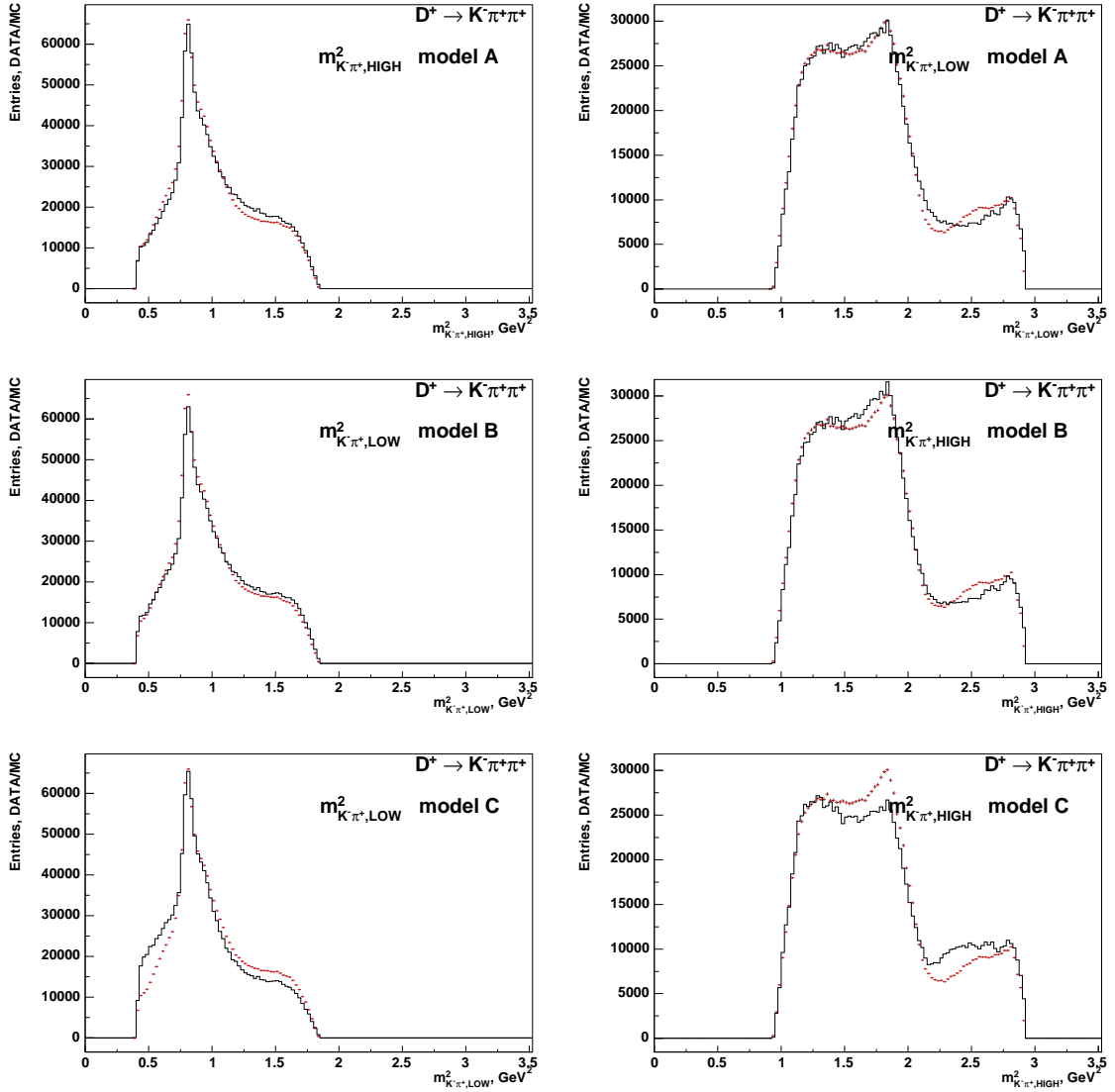


Figure 6.3: Comparison of the low-mass(left) and high-mass(right) combination in $D^+ \rightarrow K^- \pi^+ \pi^+$ decays between E791 model A (top), model B (middle) and model C (bottom), as compared with our data (points with error bars).

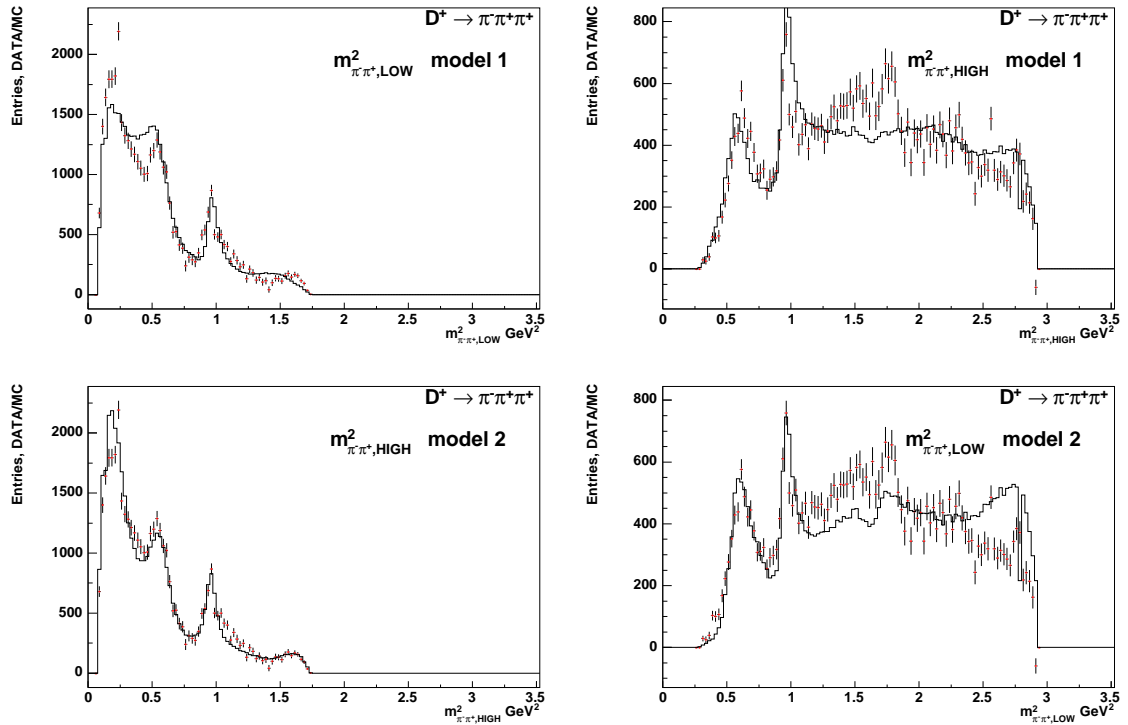


Figure 6.4: Comparison of the low-mass(left) and high-mass(right) combination in $D^+ \rightarrow \pi^- \pi^+ \pi^+$ decays between E791 model 1 (top) and model 2 (bottom), as compared with our data (points with error bars).

Chapter 7

Event Selection and Candidate Reconstruction

Our goal is to reconstruct fully hadronic D^+ meson decays, from a sample preselected by the B-CHARM triggers. To do this, we consider all track combinations in the events that pass the triggers, and try to recognize track triplets that could be coming from the D^+ decays. To each of those tracks, we assign the mass of kaon or pion, depending on the channel being reconstructed and the track charge. We then reconstruct the three track invariant mass, based on the kaon/pion mass hypotheses and the track momenta. The track triplets originating from the D^+ decays into the channels being reconstructed should form gaussian-like mass peaks.

To make best use of the trigger preselection, we confirm the trigger requirements on every D^+ candidate. This helps to remove from the dataset the so called volunteers: events which passed all three trigger levels but are not coming from the long lived particle decay. This could happen due to an existence of a fake track, or tracks which happen to satisfy the conditions but do not come from the candidate. Therefore, we

require that two of the three final state tracks be matched to the tracks that actually passed the trigger.

Ultimately, we want to extract the number of reconstructed D^+ candidates with the smallest relative statistical error. We therefore use the selection criteria which maximize the statistical significance of the signal. The procedure by which we arrive at this set of selection criteria is described in Section 7.5.

Our candidate reconstruction is entirely track based. We first describe methods of track preparation, then impose track quality requirements. The quality requirements reduce the amount of background originating from misreconstructed tracks.

7.1 Track Preparation

Because we reconstruct D^+ candidates based solely on the tracks of their daughters, we take special care to ensure that tracks used for reconstruction are of the highest available quality.

Due to misalignments in the detector subsystems and hits caused by noise in the tracking system, fake and mismeasured tracks inevitably appear in the data. A simple way to reduce their occurrence is to require a minimum number of hits in the drift chamber and the silicon detector. We require of tracks to have at least 20 axial and 16 stereo hits in the central tracker.

Studies done on Monte Carlo and data have shown that the error matrix of the COT track fit underestimates the measurement errors. In order to correct for this problem, we refit each COT track. Before fitting, we rescale the covariance matrix of the COT track: $c_{ij}^{new} = s_i s_j c_{ij}$, where the indices i and j stand for the different track parameters. The scale factors are obtained experimentally. For a representative

sample of tracks, distributions of each of the five track parameters are created, such that each value is divided by its error, as it was estimated by the fitting of the track. If the errors are correct, the resulting distribution should be a perfect Gaussian with the unit width. If it is not so, the errors are rescaled until $\sigma = 1$ for each track parameter distribution. The resulting scale factors, used for this measurement, are:

$$\begin{aligned}
 s(\lambda) &= \sqrt{1 + p_\lambda(1 + \lambda^2)^{1.5}/p_T^2}, & \text{with } p_\lambda &= 0.580 \\
 s(C) &= \sqrt{1 + p_C/p_T^2}, & \text{with } p_C &= 5.33 \\
 s(z_0) &= \sqrt{1 + p_{z_0}(1 + \lambda^2)^{1.5}/p_T^2}, & \text{with } p_{z_0} &= 0.653 \\
 s(d_0) &= \sqrt{1 + p_{d_0}/p_T^2}, & \text{with } p_{d_0} &= 3.01 \\
 s(\phi_0) &= \sqrt{1 + p_{\phi_0}/p_T^2}, & \text{with } p_{\phi_0} &= 3.01
 \end{aligned} \tag{7.1}$$

Here, $\lambda = \cot \theta$.

The rescaled COT track is used as a starting point for the refit of the combined COT and silicon track. We do not use the Layer00 hits in this analysis, because the hits from this system were considered not properly aligned at the time of data taking. The refit of the track takes into account the energy loss corrections for kaons and pions, according to the species requested. The refitting is done using a specific the track fitting package (Kalman, commonly used by high energy physics collaborations), which contains the description of the detector material and the alignment table relevant for our data.

Each of the tracks we use in this analysis has to satisfy the following track quality criteria:

- COT hits, axial: ≥ 20
- COT hits, stereo: ≥ 16

- $p_T \geq 0.5 \text{ GeV}/c$
- $|\eta| \leq 2.0$

These criteria are motivated by our need to extract the track parameters with high precision. Given that the maximum possible number of both axial and stereo hits is 48, a track that has a fraction of that number is likely composed of random hits not produced by a single charged particle. If it is in fact a genuine track, it will be measured with poor resolution. Similarly, a very low p_T track will have poor resolution of its parameters, especially the impact parameter. The limit on the geometrical variable of pseudorapidity assures that the particle passed through the central tracker ($|\eta| \leq 1.0$) or, at the very least, through both SVX and the Intermediate Silicon Layers ($|\eta| \leq 2.0$).

7.2 Track matching to SVT

For a relative rate analysis, it is essential to avoid counting the so called volunteer candidates. Recall that these can be present for several reasons. Among the most relevant here is the possibility of only one track of the D^+ decay passing the trigger criteria while the second one is provided by a fake XFT track which got assigned several accidental hits and thus has high probability of having a large impact parameter. Events like these will not be reproduced by Monte Carlo. Unless we prevent volunteers from entering as candidates, we are likely to measure incorrect efficiencies. We address this by matching the offline tracks with the SVT trigger tracks, and confirming the trigger requirements on each offline trigger track.

We first match the good quality offline tracks, at least two out of the three that

come from the D^+ candidate, to the SVT tracks.

The quantities available for this selection are: track charges, track curvatures and transverse momenta, the linear SVT p_T sum, the $\Delta\phi$ angle between the SVT tracks, and the L_{xy} as calculated from the SVT track parameters. The SVT track quantities get recorded as they were at the time of trigger decision, thus the original trigger decision can be reached again during data analysis.

The SVT track matching algorithm calculates the distance:

$$\Delta = \sqrt{\frac{(C_{offline} - C_{SVT} - C_{mean})^2}{\sigma_C^2} + \frac{(\phi_{offline}^0 - \phi_{SVT}^0 - \phi_{mean}^0)^2}{\sigma_\phi^2}} \quad (7.2)$$

where $C_{offline}$ is the offline measured curvature, C_{SVT} is the curvature measured by the SVT, $\phi_{offline}^0$ and ϕ_{SVT}^0 are the ϕ_0 angles measured by the offline and SVT reconstruction, respectively. C_{mean} and σ_C are the mean and the width of the difference between online and SVT curvature measured in the J/ψ signal data [33]. ϕ_{mean} and σ_ϕ are the corresponding mean and width of the ϕ difference. The non-zero mean of the difference in ϕ between SVT and the offline tracks is a consequence of the different silicon alignments used in offline and SVT reconstruction. As the ϕ and the curvature measurements in a track fit are correlated, the curvature difference between SVT and offline tracks will also have a non-zero mean.

Offline matching is only done on tracks with good quality SVT fit ($\chi^2 \leq 25$). To ensure that an offline track is matched to an SVT track, we require that the distance Δ be less than 95, and that the SVT measurements of the transverse momentum and the impact parameter comply with $p_T > 2 \text{ GeV}$, and $120 \mu\text{m} < |d_0| < 0.1 \text{ cm}$.

7.3 Trigger Confirmation

Because the SVT track fit is not obtained from the same set of hits and tracking algorithm as the offline fit, it is crucial to confirm that trigger requirements are satisfied by the offline tracks. The differences between SVT and offline track quantities are subtle, necessitating careful analysis. We start by recording the complete set of trigger bits, for all three trigger levels and for each event.

We perform two types of trigger confirmation: at the level of event, and at the level of candidate. At the level of event, we need to be able to assign each event to a particular trigger path. While this could in principle also be done at the candidate rather than event level, the trigger prescaling and the shared phase space of the trigger paths make the matter more complicated. The `B_CHARM`, `B_CHARM_LOWPT` and `B_CHARM_HIGHPT` trigger paths share a lot of phase space. Consequently, a candidate which passes `B_CHARM` (scenario A) confirmation might not have been accepted through the `B_CHARM` path because of the dynamic prescale, but instead might have gotten accepted through one or both of the other two paths. Independent trigger prescales for triggers sharing phase space therefore necessitate proper storing of the event trigger bits.

In addition to the event based trigger bit information, we store candidate based trigger variables, and require that the trigger criteria be confirmed on the decay products of the D^+ candidate. This procedure guarantees that the candidate track was not a volunteer, but a qualified track that caused the event to be accepted by the trigger.

Finally, we ask that the trigger bit be matched with the corresponding set of selection criteria satisfied by two of the three daughter tracks. This candidate level

trigger confirmation further suppresses volunteers.

7.4 Candidate Reconstruction

As we emphasized earlier, the reconstruction $D^+ \rightarrow \pi^- \pi^+ \pi^+$ and $D^+ \rightarrow K^- \pi^+ \pi^+$ candidates in an event is based on tracking information. It relies on a set of selection criteria optimized to quickly reject uninteresting events. We consider all triplets of tracks that passed track quality requirements. In forming these triplets we combine one track of one charge and the other two of the opposite charge. We accept only those combinations for which at least two of the three tracks are trigger tracks. The raw mass is calculated based on the track momenta, and candidates are only accepted within the loose mass window (between 1.7 GeV and 2.1 GeV). In order to distinguish tracks from the relatively long-lived D^+ from tracks coming from the primary vertex, we look for a vertex that is displaced relative to the primary vertex, that is, one that is formed by displaced tracks. We find the D^+ decay vertex by using the procedure called vertex fit, which involves finding the best estimate for the common vertex given the track parameters of the three tracks. Vertex fitting provides improved track parameters, and therefore improved measurement of the invariant mass. Long lived particles appear as Gaussian-shaped peaks in the otherwise smooth mass spectrum.

The reconstruction requirements are summarized below. If a three track combination satisfies all of them, it is accepted as a candidate and its invariant mass is measured.

- 3 tracks satisfying track quality requirements:
 - COT hits, axial: ≥ 20

- COT hits, stereo: ≥ 16
- $p_T \geq 0.5$ GeV/c
- $|\eta| \leq 2.0$
- ≥ 2 SVT matches with $p_T \geq 2\text{GeV}$, $120 \mu\text{m} \leq |d_0| \leq 1000 \mu\text{m}$
- converged vertex fit of the tracks

The resulting $D^+ \rightarrow \pi^- \pi^+ \pi^+$ and $D^+ \rightarrow K^- \pi^+ \pi^+$ mass spectra still contain too much background for signal extraction. We need to apply a tighter set of requirements, based on the physics properties of the signal modes and the statistical considerations.

7.5 Optimization of Selection Requirements

When reconstructing the D^+ decays, our goal is to extract the candidate yields with the smallest relative statistical error. This will ensure that the statistical error of branching ratio measurement is as small as possible. We now describe the process of obtaining a set of selection requirements that accomplish this goal.

We have to be careful not to choose selection requirements which artificially enhance the D^+ meson yields. We avoid this by using a combination of data and Monte Carlo simulated events to optimize selection requirements. To estimate the number of signal events (S) after selection requirements are applied, we use Monte Carlo signal events. To estimate the number of background events (B) after the same selection, we use a sample of data that contains no signal, but is kinematically similar to it due to being near the signal region. This data subsample is called sideband. We define the signal region as residing within $\pm 2\sigma$ from the PDG [8] value for D^+ mass

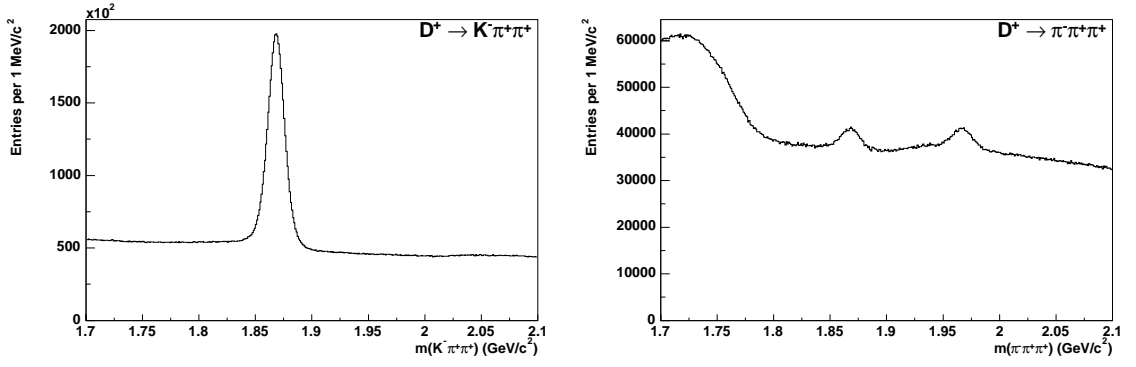


Figure 7.1: Mass spectra of $D^+ \rightarrow K^- \pi^+ \pi^+$ (left) and $D^+ \rightarrow \pi^- \pi^+ \pi^+$ (right) decays, made with loose set of selection requirements used in studies.

(1869.3 ± 0.5 MeV). The sidebands span $[3\sigma, 7\sigma]$ region on both sides of the mass peak.

From these estimated numbers of signal and background events, we construct the statistical significance, defined as

$$\frac{S}{\sqrt{S+B}}. \quad (7.3)$$

We then vary the selection requirements to maximize this significance.

As emphasized before, we use the same set of selection criteria for extracting the signal of both channels, allowing for most systematic uncertainties to cancel each other out in the ratio of the yields. We perform the selection optimization procedure on the $D^+ \rightarrow \pi^- \pi^+ \pi^+$ channel. This channel, in contrast to $D^+ \rightarrow K^- \pi^+ \pi^+$, has a low signal to background ratio, as seen in Figure 7.1, so it is the significance of the $D^+ \rightarrow \pi^- \pi^+ \pi^+$ yields that we need to maximize in order to minimize the uncertainty. The plots in the figure are made with the set of very loose selection criteria, too loose for signal extraction but appropriate for efficiency studies.

We chose the discriminating quantities guided by the decay topology. Good vertex fit is a strong discriminating quantity, as it can be seen in Monte Carlo (Figures 7.2 and 7.3), so $\chi_{r\phi}^2(D)$, which is a measure of the vertex fit quality, may be used for the signal selection. The long life of the D^+ mesons distinguishes their decay products from the particles originating in the primary vertex. To make use of this fact, we measure the proper decay length of the candidate particle (ct), and use it as a selection criterion. The transverse momentum of the D^+ meson is also expected to be different from the transverse momenta of fake candidates that are constructed from random combinations of tracks; it therefore makes a good selection variable. By imposing a requirement on the decay time and p_T of the candidate, we are also effectively imposing a geometric requirement on the displacement in the laboratory frame of the secondary vertex (decay of the D^+) with respect to the primary vertex (production of the D^+). This variable is called L_{xy} , and is an implicit selection variable. Among the tracks coming from primary vertex, there are those with very low transverse momenta, too low to be coming from the $\pi\pi\pi$ or $K\pi\pi$ decays of the D^+ . By requiring that all tracks have $p_T \geq 600\text{MeV}$, we can reject some of the fake D^+ candidates.

The sample of $D^+ \rightarrow K^-\pi^+\pi^+$ candidates will likely be contaminated by D^* decays. These can look like the D^+ decays of interest when they proceed as follows: $D^{*+} \rightarrow D^0\pi_s \rightarrow [h^-h^+]\pi_s$. Here, “h” stands for a hadron, and the most probable h^-h^+ decay of the D^0 , leading to the $K^-\pi^+\pi_s^+$ final state. The index “s” here refers to the pion being soft, that is, of low transverse momentum. The D^{*+} decay vertex can look like that of D^+ decay because of the relatively short D^0 lifetime ($c\tau = 123.0\mu\text{m}$). Due to the proximity of the D^* and D^0 vertices and the limited accuracy of our vertex reconstruction, it is possible to mistakenly combine the π_s from D^* with the D^0 daughters, thus forming a 3-track vertex and obtaining a fake

D^+ candidate. While D^* itself usually does not live long enough to be substantially removed from the primary vertex, it could be produced in decay of a B meson, which would make its decay vertex displaced due to the long lifetime of the B . To suppress the D^* contribution, we try to reject decays in which the third track belongs to a very soft pion. We require that the difference between the D^+ invariant mass and the invariant mass of two of its daughters, be large enough to ensure a pion of sizable momentum: $m(D^+) - m(h^-h^+) \geq 160$ MeV. This requirement is responsible for the cut off high mass corners of our Dalitz plots.

The final set of selection quantities is therefore: $\chi_{r\phi}^2(D)$, $|d_0(D)|$, $ct(D)$, $p_T(D)$, $|d_0(tracks)|$, $\Delta M(D, K\pi(\pi\pi))$. We later add a requirement on the invariant mass of the same charge particles, $M(\pi\pi)$ (see below).

We study the distribution of the selection quantities in Monte Carlo samples, and qualitatively verify that they match the data well enough. The agreement between our signal Monte Carlo and the data for these variables is shown in plots of the Figures 7.2 and 7.3. The plotted data is sideband subtracted, that is, showing only properties of signal.

As already emphasized, we use the same criteria for extracting the signal of the two channels, allowing for most systematic uncertainties to cancel each other. We optimize the selection criteria to maximize the significance of the less probable $\pi\pi\pi$ decay. We occasionally use another set of selection requirements, too loose for signal extraction, but useful for efficiencies studies. As Figure 7.1 indicates, these requirements are inadequate for $\pi\pi\pi$ channel, but for $K\pi\pi$ channel they give a satisfactory signal to background ratio. These loose selection requirements are used in (XFT) efficiency studies, based solely on the $K^-\pi^+\pi^+$ channel (Section 9.3). Throughout this dissertation, the selection requirements used to make plots and tables are the

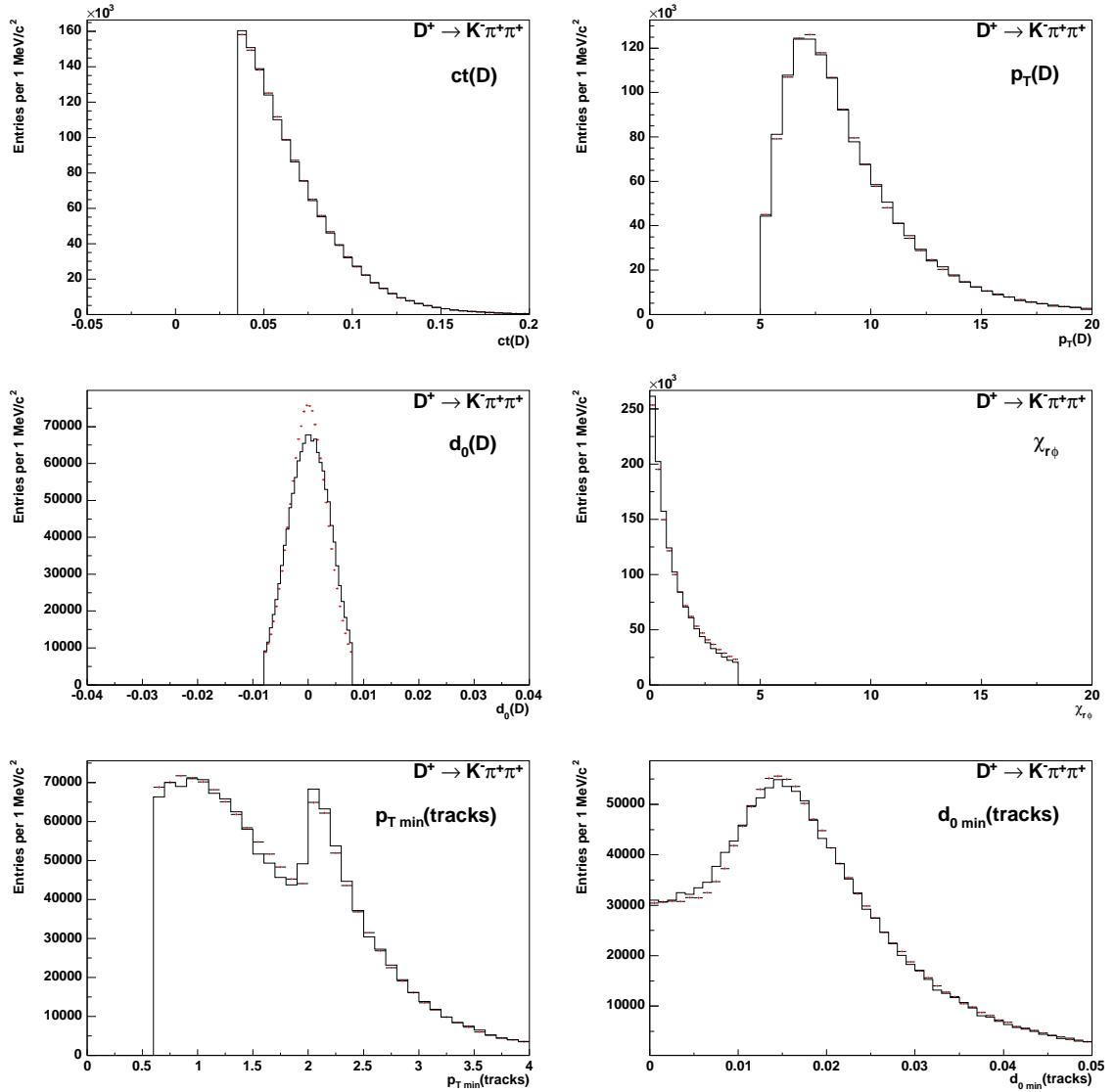


Figure 7.2: Data - Monte Carlo comparison of six kinematic variables, used for extracting the $D^+ \rightarrow K^- \pi^+ \pi^+$ signal. Dots with (tiny) error bars are data points, and histogram represents Monte Carlo.

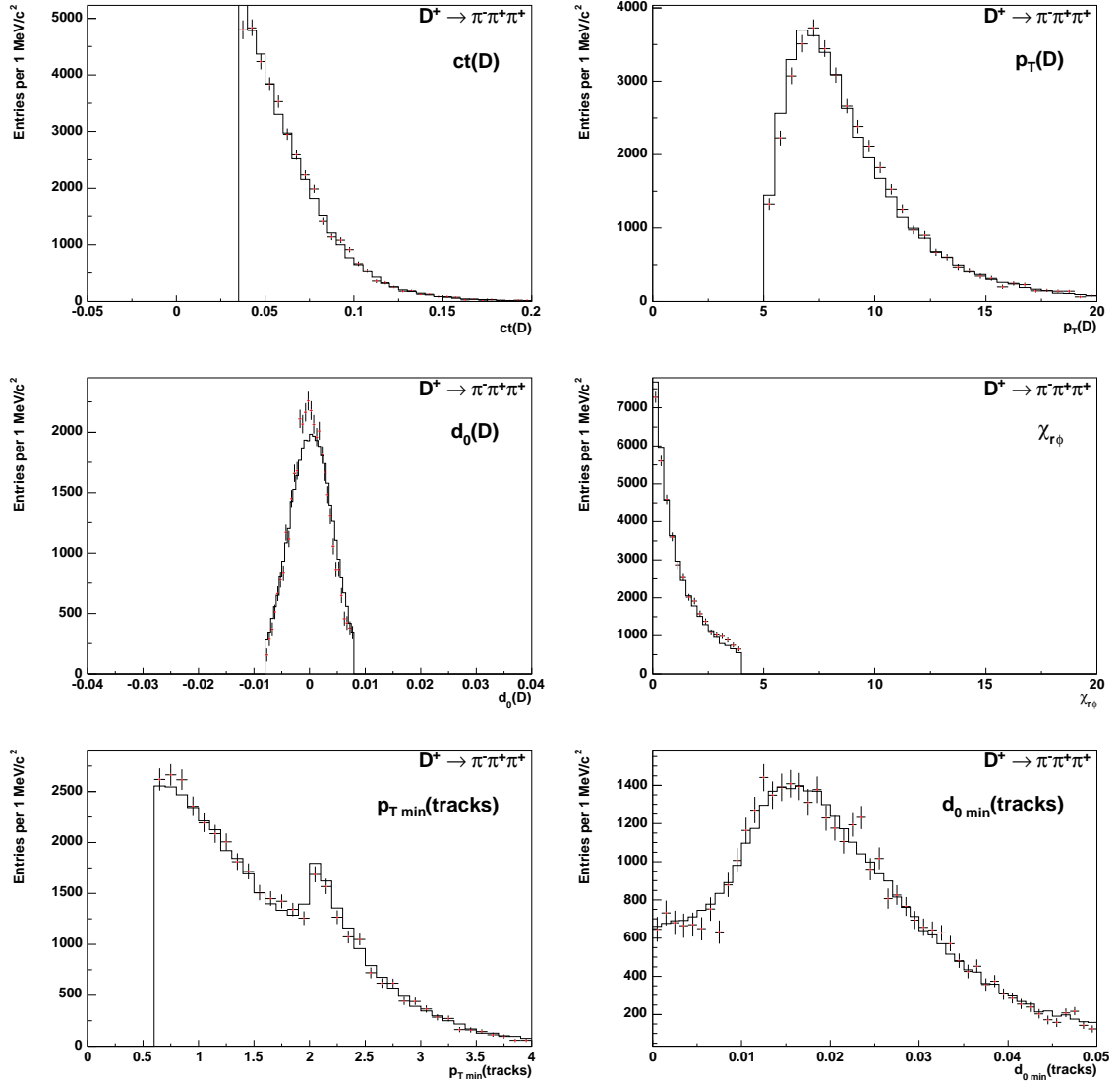


Figure 7.3: Data - Monte Carlo comparison of six kinematic variables, used for extracting the $D^+ \rightarrow \pi^- \pi^+ \pi^+$ signal. Dots with error bars are data points, histogram represents Monte Carlo.

tight, optimized ones, unless explicitly said otherwise.

The selection criteria are optimized by maximizing statistical significance, $\frac{S}{\sqrt{S+B}}$, of the $\pi^-\pi^+\pi^+$ decay. Here, S is the expected number of signal events taken from Monte Carlo, and B is the expected number of background events, taken from the data sidebands.

In varying the selection criteria, we perform a simultaneous scan of all criteria combinations. With 7 possible values for the $\chi^2(D)$, and 6 for each of the 5 other variables, this amounts to $7 \times 6 \times 6 \times 6 \times 6 = 54432$ combinations of selection requirements. Plots in Figure 7.4 show the results of the optimization procedure. The track impact parameter variable turns out best not constrained, hence we do not mention the d_0 requirement any further. As for the transverse momentum, p_T , of the tracks, statistically preferred lowest value is at 0.5 GeV, but allowing such a low value would mean letting D^* decays to D^0 and π_s in; we opt for requiring $p_T \geq 0.6$ GeV. We also depart from the results of the optimization regarding the lifetime (ct) requirement. Tightening the requirement, as described below, reduces the systematic uncertainties which, in this analysis, dominate the statistical ones.

The summary of the final selection requirements is in Table 7.1. After their application, the $D^+ \rightarrow \pi^-\pi^+\pi^+$ and $D^+ \rightarrow K^-\pi^+\pi^+$ mass spectra look as in Figure 7.5.

The D^+ meson mass distribution peaks at around 1.87 GeV. In the $\pi^-\pi^+\pi^+$ mass plot, the large structure on the low end of the spectrum is the contribution from the much more frequent $K^-\pi^+\pi^+$ mode, where pion mass gets misassigned to a kaon. On the high mass side of the signal, at around 1.96 GeV, we see the $\pi^-\pi^+\pi^+$ reconstructed decay of the D_s^+ meson.

To see the effect of tightening the ct requirement, consider the plot in Figure 7.6, made with the statistically optimized value (250 μm). The wide structure under the

cutscan of the significance w.r.t. optimal cuts

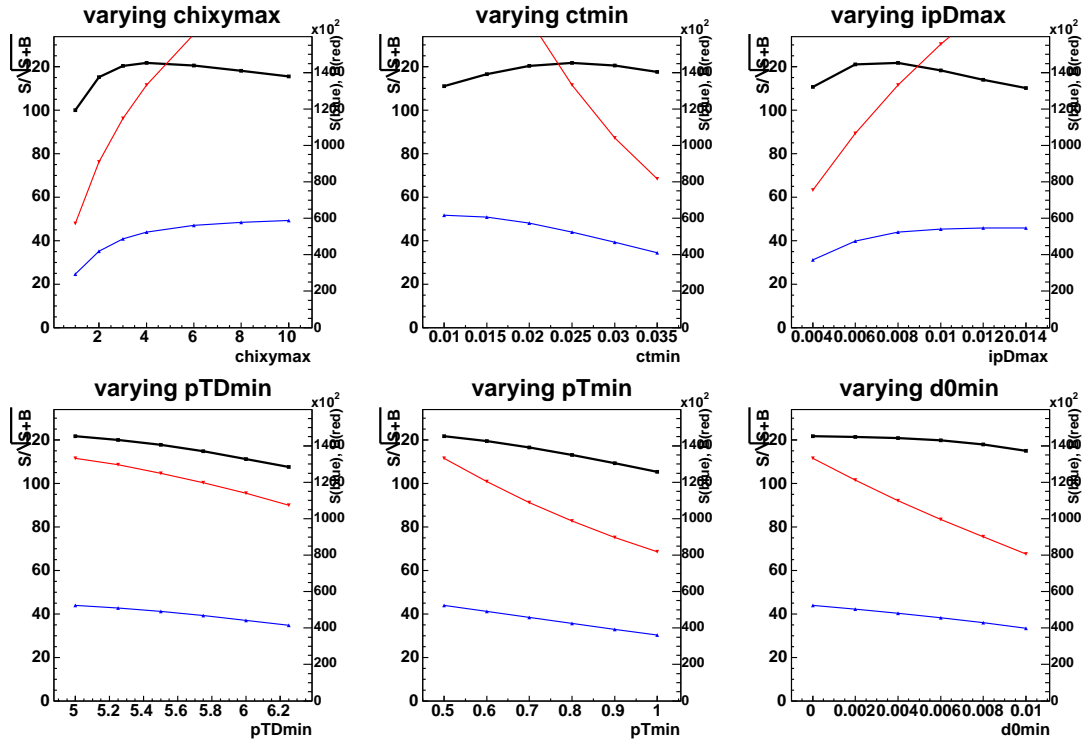


Figure 7.4: Cut-scan of the significance (black line) with respect to selection criteria values, for $D^+ \rightarrow \pi^- \pi^+ \pi^+$ decay. The signal yields, blue, are taken from the Monte Carlo, the background (red) from sidebands of the data.

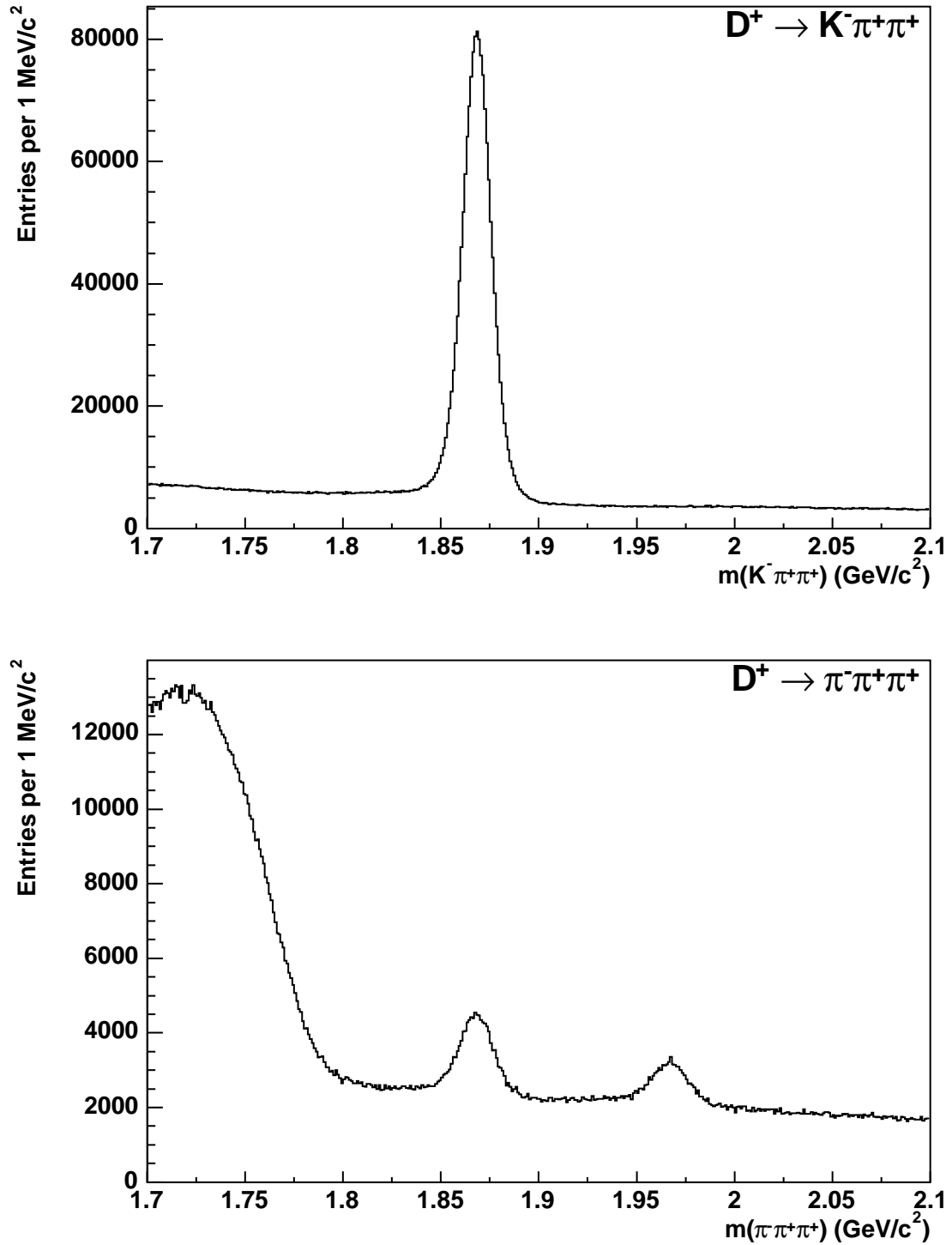


Figure 7.5: Mass spectrum of $D^+ \rightarrow K^- \pi^+ \pi^+$ decay (above) and $D^+ \rightarrow \pi^- \pi^+ \pi^+$ decay (below), obtained with the $\pi\pi\pi$ -optimized tracks.

Parameter	Selection Criterion	
	Loose (studies)	Tight (signal)
$\chi_{r\phi}^2(D)$	≤ 20.0	≤ 4.0
$ d_0(D) $	$\leq 500 \mu\text{m}$	$\leq 80 \mu\text{m}$
$ct(D)$	—	$\geq 350 \mu\text{m}$
$p_T(D)$	$> 4.0 \text{ GeV}/c$	$> 5.0 \text{ GeV}/c$
$p_T(\text{tracks})$	$\geq 0.5 \text{ GeV}/c$	$\geq 0.6 \text{ GeV}/c$
$\Delta m_{D^+,h-h^+}$	$> 160 \text{ MeV}$	$> 160 \text{ MeV}$
$M(\pi^-\pi^+) (\pi\pi\pi \text{ channel only})$	—	$\leq 480 \text{ MeV} \text{ OR } \geq 520 \text{ MeV}$

Table 7.1: Summary of selection criteria for $D^+ \rightarrow \pi^-\pi^+\pi^+$ and $D^+ \rightarrow K^-\pi^+\pi^+$ decays. The ‘‘Loose’’ requirements are used for efficiency studies, and are meaningful only for $K\pi\pi$ channel; for $\pi\pi\pi$ they allow too much background. The tight criteria are used for signal extraction.

D_s^+ peak, part of the complex charm decays background, is significantly reduced when the requirement is tightened to $350\mu\text{m}$, as in Figure 7.5.

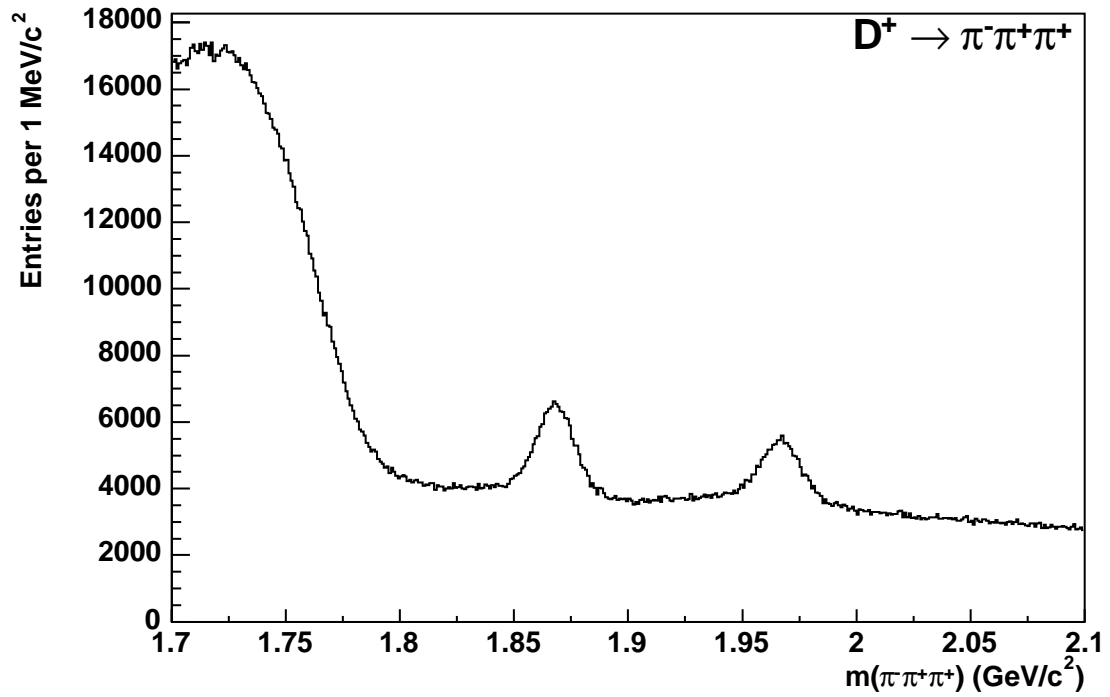


Figure 7.6: $D^+ \rightarrow \pi^-\pi^+\pi^+$ mass, with $ct \geq 250 \mu\text{m}$; the wide structure under the D_s^+ peak is diminished when the requirement is tightened to $350 \mu\text{m}$.

As explained before, the $\Delta m_{D^+, h^- h^+}$ requirement ($m(D^+) - m(h^- h^+) \geq 160 \text{ MeV}$) is effective in suppressing the D^* contribution ($D^* \rightarrow D^0 \pi_s \rightarrow [h^- h^+] \pi_s$) to the $K \pi \pi$ mass. We also add a constraint on $M(\pi\pi)$, $M(\pi\pi) \leq 480 \text{ MeV}$ or $M(\pi\pi) \geq 520 \text{ MeV}$, and apply it only to the $\pi^- \pi^+ \pi^+$ channel, to suppress contributions from $D^+ \rightarrow K_s \pi^+$ decays. The long-lived K_s particle travels for several tens of centimeters and decays into $\pi^- \pi^+$, thus mimicking the $D^+ \rightarrow \pi^- \pi^+ \pi^+$ decay. The $M(\pi\pi)$ requirement results in 7.5% candidate loss.

Chapter 8

Yields Analysis

8.1 General Fit Model

We now derive models for the shapes of the $D^+ \rightarrow \pi^- \pi^+ \pi^+$ and $D^+ \rightarrow K^- \pi^+ \pi^+$ signal peaks and of the background, including combinatorial background and reflections. We model the mass space of our data using binned χ^2 fits on Monte Carlo for templates derivation, and likelihood fits on the data. We describe the reflection fits in Section 8.2, the signal shape study in Section 8.3. We estimate the systematic uncertainties of the yields at the end of this chapter (Section 8.5).

8.2 Reflections Fits

To study the reflections backgrounds, we generate large samples of inclusive Monte Carlo decays of D^+ , D_s^+ , and D^* , all of which can produce non-trivial background structures. We study their mass distributions and distinguish those that produce bump-like reflections structures. For each of these we derive a template, that is, an

analytical function that describes the distribution shape. The choice of the function is motivated by physics arguments, and is determined by the best fit to the distribution.

To derive the reflections shape template, we run the D^+ reconstruction code on the Monte Carlo samples listed in Table 6.1. We use information from the HEPG bank, which contains complete decay chains and momenta of all particles produced, to group the candidates by decay mode. We plot the individual decay modes and observe structures shown in Figure 8.1. The plots are not normalized between themselves, but clearly show that signal mass regions contain reflections from other decays.

Inspection of the plots reveals several different contributions to the signal modes. The D_s^+ , when decaying to the Cabibbo allowed $KK\pi$ mode, contributes significantly to the $K\pi\pi$ mass spectrum. On the other hand, the partially reconstructed decays of the D_s^+ , such as $\pi^-\pi^+\pi^+\gamma$ and $K^-\pi^+\pi^+\pi_0$, add up to a nontrivial structure in the wide region around the $D^+ \rightarrow \pi^-\pi^+\pi^+$ signal.

While the inclusive D^+ decays produce non-negligible structures in the low mass (but not high mass) region of the spectrum (Figure 8.1), the D^* contribution is small and trivially shaped, so it can either be disregarded or else absorbed into the combinatorial background. As Figure 8.2 shows, when reconstructed as $D^+ \rightarrow \pi^-\pi^+\pi^+$ mode, the D^* is effectively suppressed by the selection requirements. Its contribution to the $K\pi\pi$ mass has a shape similar to that of the combinatorial background, and can be absorbed into it.

B meson decays also give combinatorics-like background, in addition to the decays proceeding through charm states. We look for structures coming from Λ_c decays, but they appear too infrequent to give measurable contribution. We consider excited charm states: inclusive $D_2^{*+} \rightarrow D^{(*)0}\pi^+$, $D_2^{*0} \rightarrow D^{(*)+}\pi^-$, $D_1^+ \rightarrow D^{*0}\pi^+$, and $D_1^0 \rightarrow D^{*+}\pi^-$ decays. In each case, we find the contribution to our mass distribution

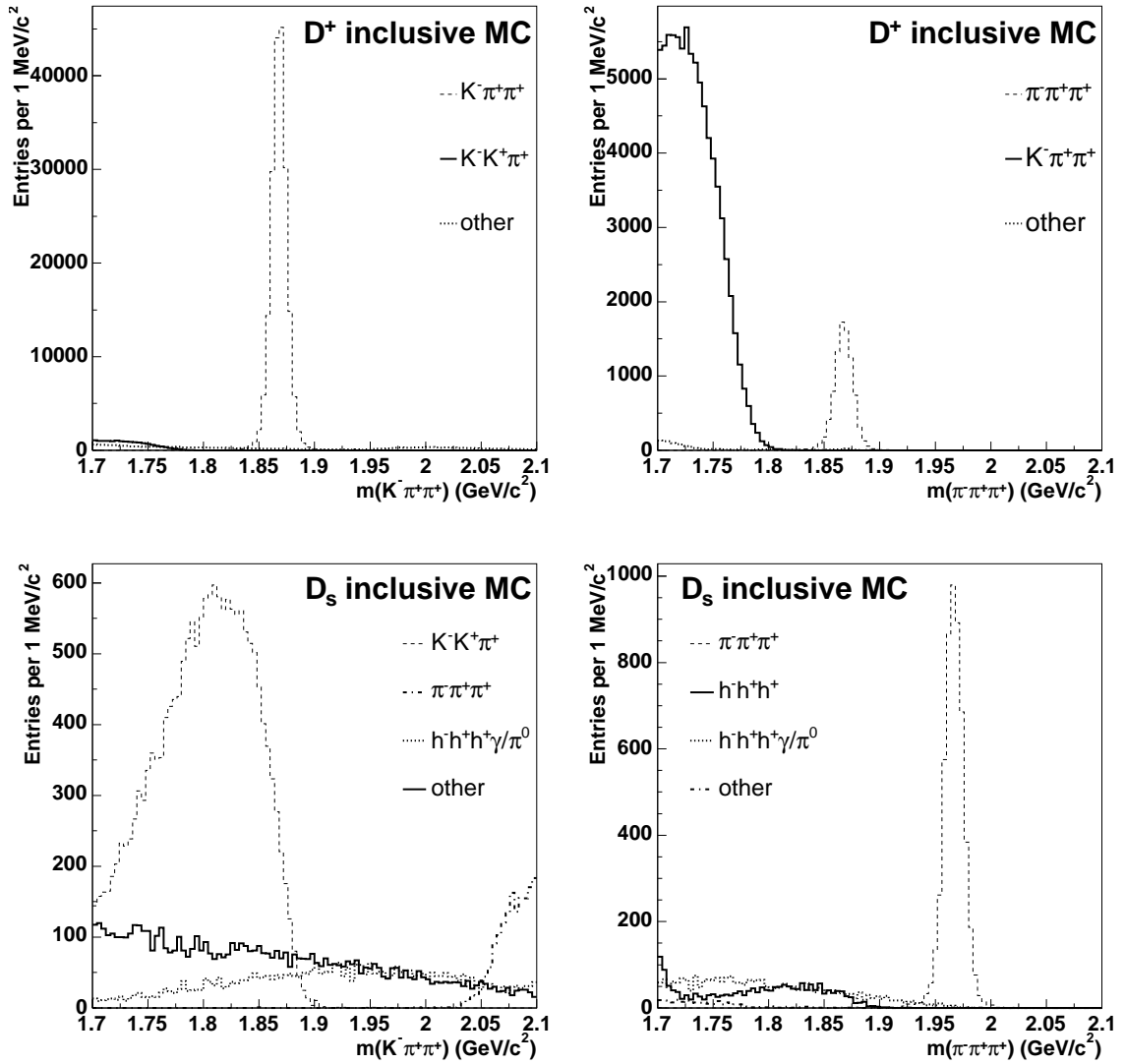


Figure 8.1: Reflections from inclusive D^+ and D_s^+ decays, reconstructed as $D^+ \rightarrow K^- \pi^+ \pi^+$ (left) and $D^+ \rightarrow \pi^- \pi^+ \pi^+$ (right), after applying the signal extraction requirements.

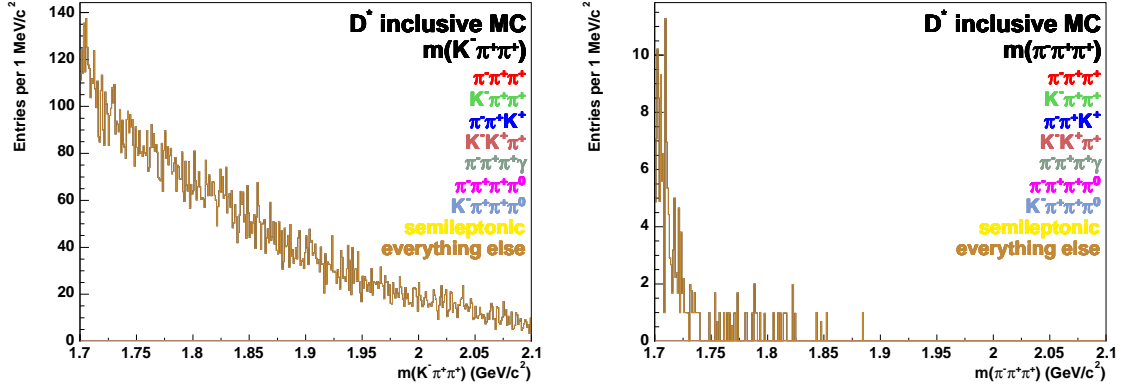


Figure 8.2: Reflections from inclusive D^* decays, reconstructed as $D^+ \rightarrow K^- \pi^+ \pi^+$ (left) and $D^+ \rightarrow \pi^- \pi^+ \pi^+$ (right), after applying the signal extraction requirements.

statistically insignificant.

We individually fit contributions from all but the most negligible D^+ and D_s^+ decays; the latter are bunched up and comprise the “other” bin. The results of these fits are shown in Figures 8.3, 8.4 and 8.5; they comprise the fit template that we apply to the data background.

In the fit to the data, we leave the overall normalizations of D^+ and D_s^+ free, and fix the relative fractions of each reflection from Monte Carlo. Therefore, for the $\pi\pi\pi$ plot, the normalization scale is effectively set by the main decay: the $D^+ \rightarrow K^- \pi^+ \pi^+$ reflection, large and dominant in the low mass region it occupies, determines the normalizations of the rest of D^+ decays. In the same way, the $D_s \rightarrow \pi^- \pi^+ \pi^+$ decay sets the scale for the other D_s^+ decays. For the $K\pi\pi$ channel, the dominant reflection is the $D_s^+ \rightarrow K^- K^- \pi^+$; it controls the norm of all other D_s^+ decays.

In contrast to the reflections, combinatorial background has a simple, slow-changing shape, which we model by a second order polynomial. Superimposing the derived reflections template and the polynomial model for the combinatorial background gives

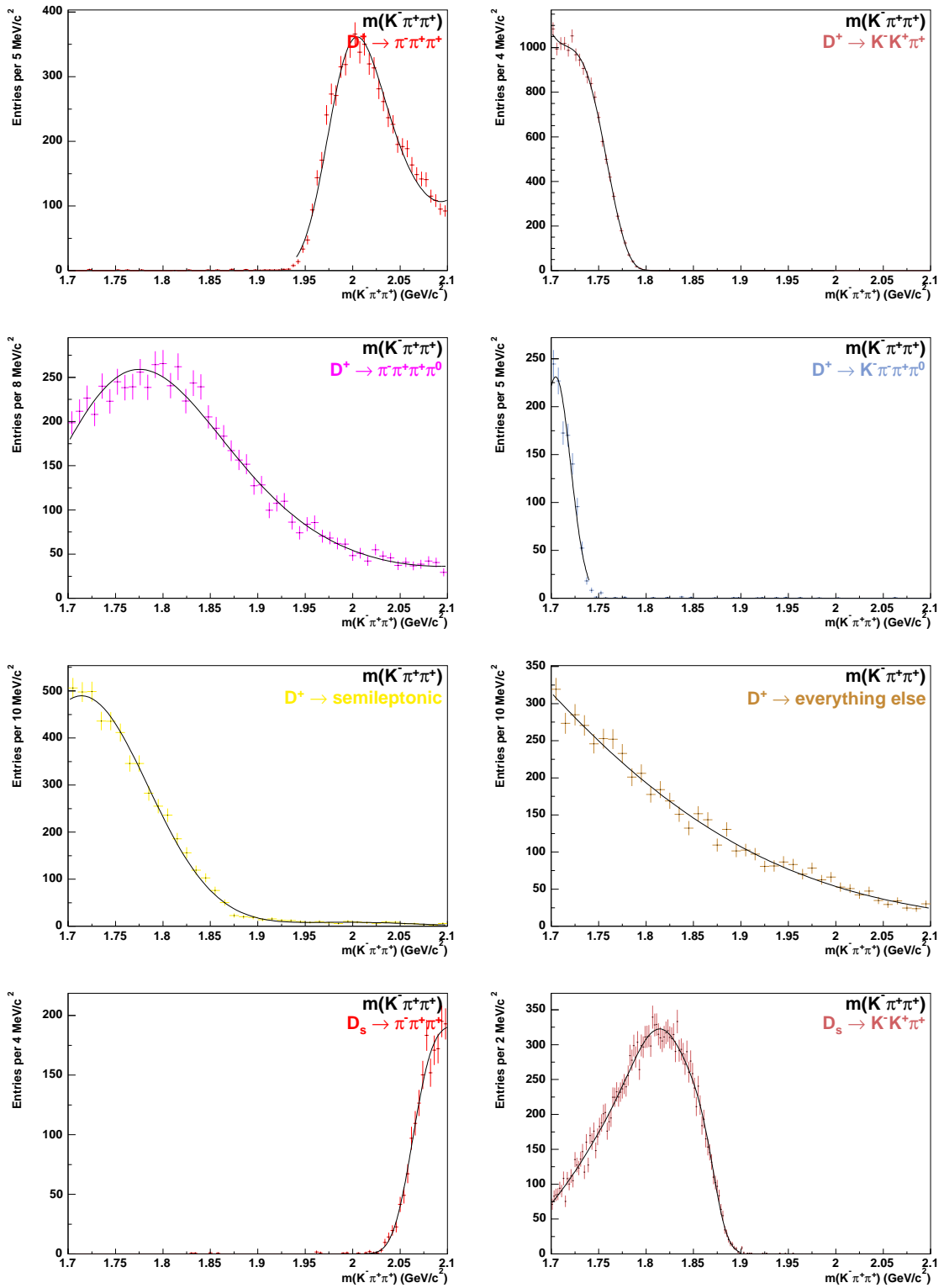


Figure 8.3: Individually fitted reflections contributing to $D^+ \rightarrow K^- \pi^+ \pi^+$ background.
Continued on next page

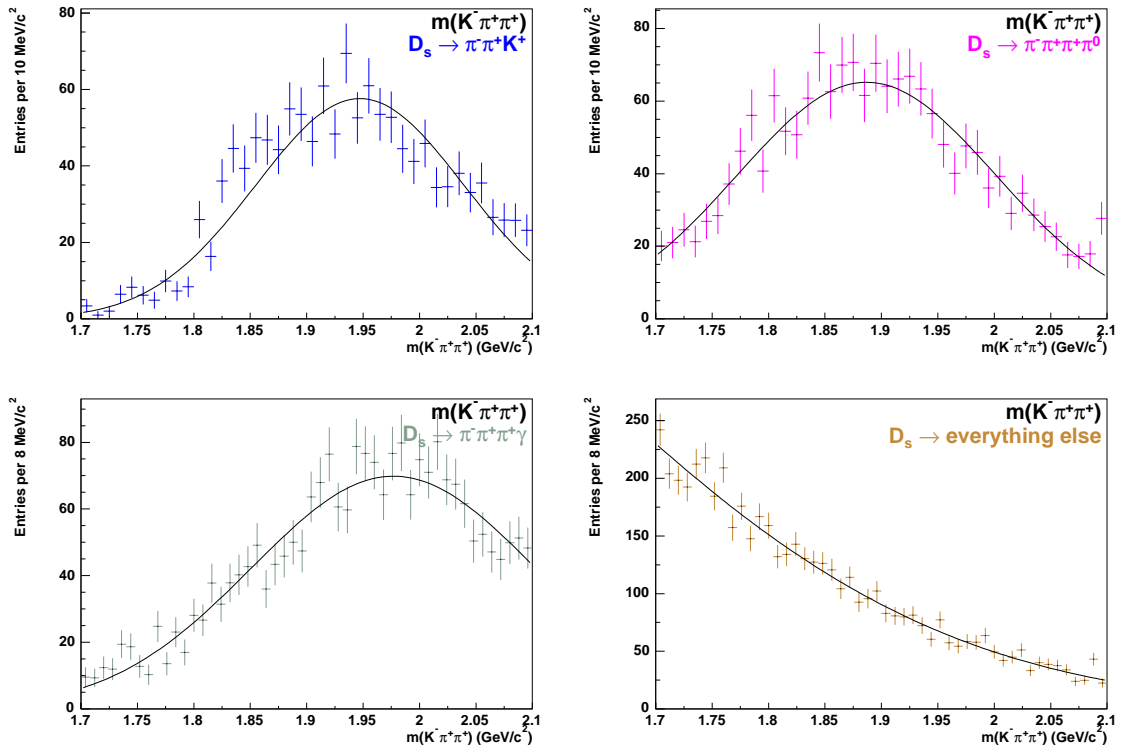


Figure 8.4: Individually fitted reflections contributing to $D^+ \rightarrow K^- \pi^+ \pi^+$ background, from D^+ and D_s^+ decays. Contributions from decays that are not shown are negligible.

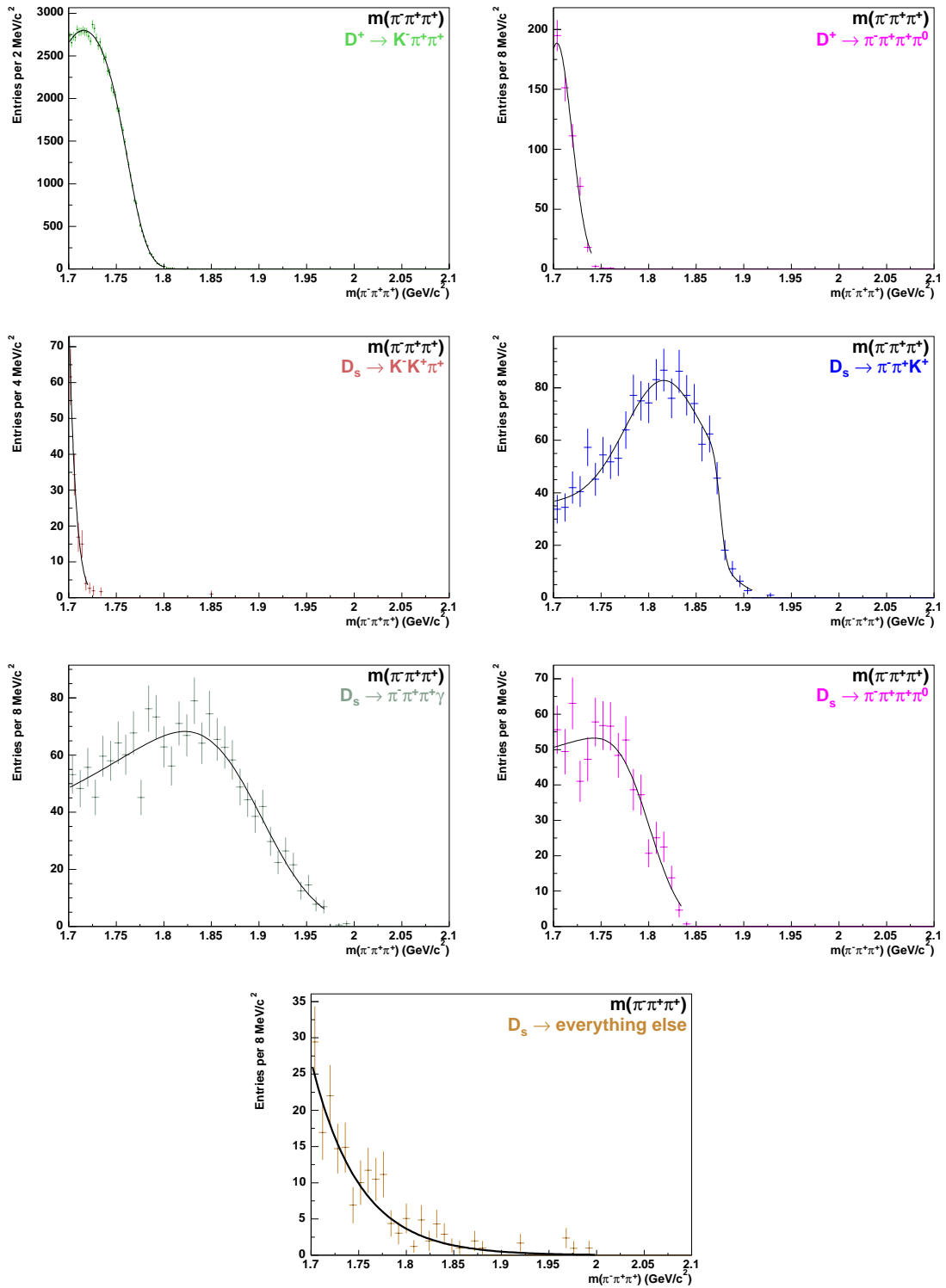


Figure 8.5: Individually fitted reflections contributing to $D^+ \rightarrow \pi^- \pi^+ \pi^+$ background, from D^+ and D_s^+ decays. Contributions that are not shown are negligible.

a complete background description.

8.3 Signal Shape

To describe the $D^+ \rightarrow \pi^- \pi^+ \pi^+$ and $D^+ \rightarrow K^- \pi^+ \pi^+$ mass peaks, we use the shape of two Gaussian functions centered on the common mean, and a radiative tail on the low mass side of the peak.

The tail models two kinds of effects: energy loss of pions and kaons in the detector due to scattering (bremsstrahlung), and the final state radiation, that is, the process $D^+ \rightarrow K^- \pi^+ \pi^+ \gamma$. The latter gives a more pronounced contribution to the tail. The tail function is a convolution of a Gaussian and an exponential, effectively a product of an exponential and an error function:

$$T(m, \sigma, a_{rad}) = \frac{0.5}{a_{rad}} \cdot e^{\left(\frac{x-m}{a_{rad}} + \sigma^2 / (2 \cdot a_{rad}^2)\right)} \cdot \text{Erf} \left(\frac{\left(x - m + \frac{\sigma}{a_{rad}}\right)}{\sqrt{2} \cdot \sigma} \right). \quad (8.1)$$

Here, m and σ are the parameters of one of the gaussians that describe the signal shape, (each of the two comes with a tail): m is the mean of the Gaussian, and σ is its width. Parameter a_{rad} determines the shape of the tail, that is, the rate of it falling off. Larger a_{rad} corresponds to a longer tail.

The total signal shape function is:

$$\begin{aligned} F_{SIG}(m, \sigma_n) &= (1 - f_{tail}) \cdot ((1 - f_w) \cdot G_n(m, \sigma_n) + f_w \cdot G_w(m, \sigma_w)) \\ &+ f_{tail} \cdot ((1 - f_w) \cdot T_n(m, \sigma_n, a_{rad}) + f_w \cdot T_w(m, \sigma_w, a_{rad})). \end{aligned} \quad (8.2)$$

The indices n and w denote the narrow and wide components of the Gaussian $G(m, \sigma)$ and its tail $T(m, \sigma, a_{rad})$. f_{tail} and f_w are the fractions of the candidates which reside respectively in the tail region and in the wide Gaussian part of the function.

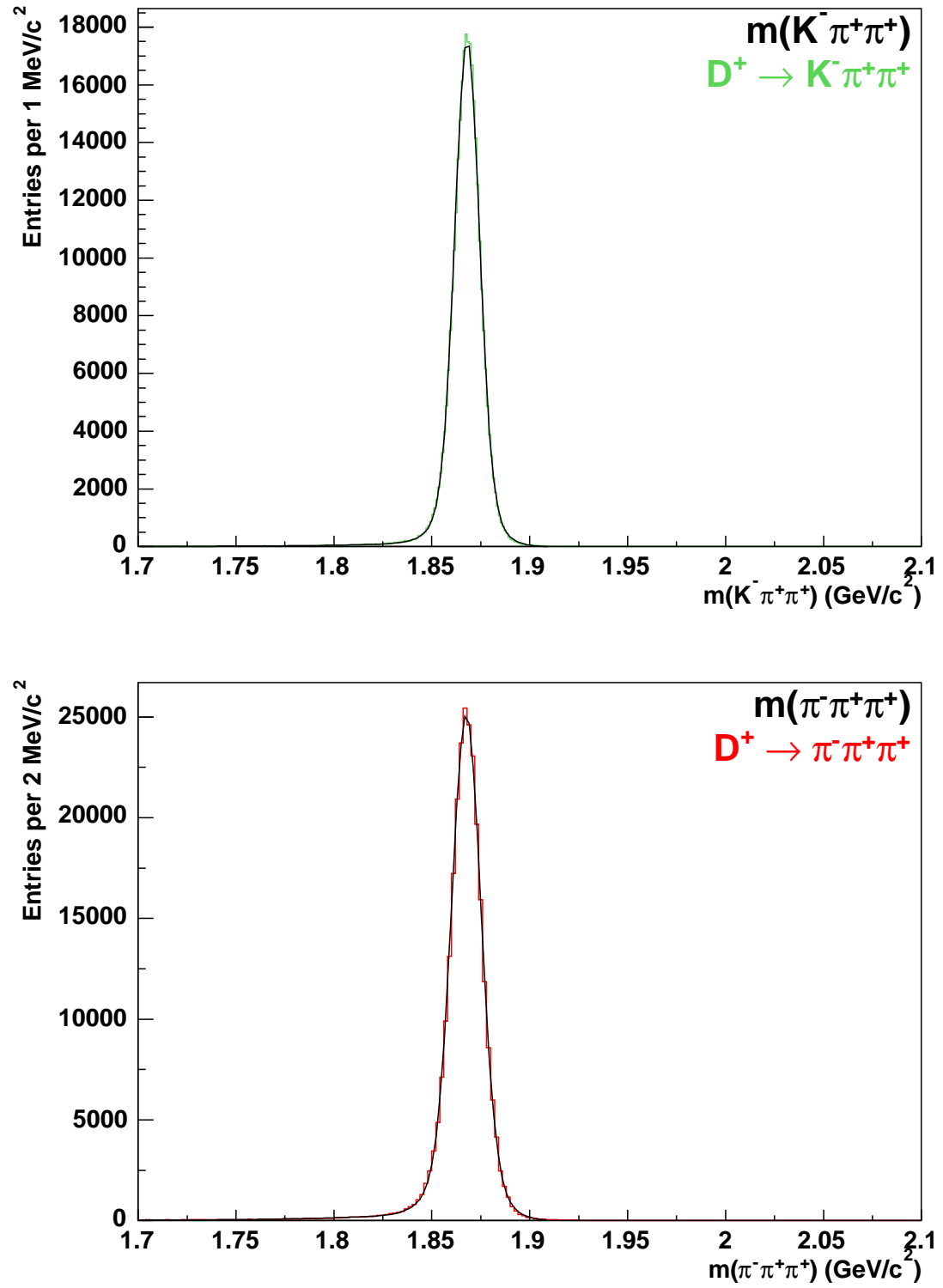
The resulting fits of both channels' signal Monte Carlo can be seen in Figure 8.6.

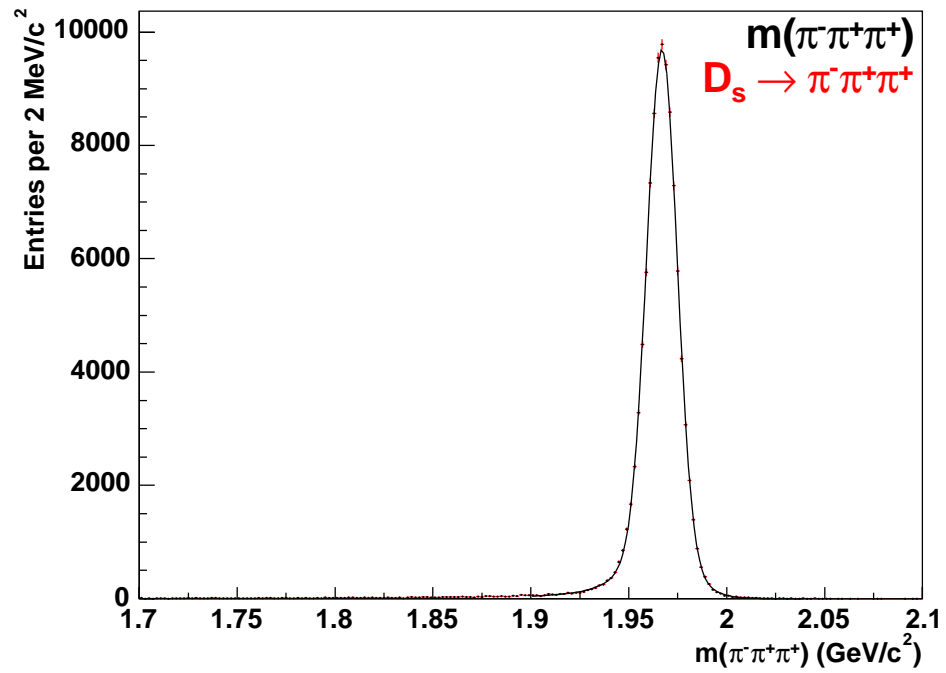
The $\pi\pi\pi$ mass windows contains the peak of the $D_s \rightarrow \pi^- \pi^+ \pi^+$ decay. The basic characteristics of this decay are similar to those of $D^+ \rightarrow \pi^- \pi^+ \pi^+$. We therefore fit it using the same function as for the signal peak. Figure 8.7 shows the fit template derived on the D_s^+ Monte Carlo that accounts for final state radiation.

The fit parameters for all three decays are listed in Table 8.1. Consider the two D^+ decays. The $\pi\pi\pi$ peak is clearly wider than the $K\pi\pi$. This is expected, as the final state is lighter than in $K\pi\pi$ case, leaving more Q value, or freed energy, available for distribution as kinetic energy. These differences in decay kinematics lead to the differences in the widths, as the detector resolution depends on the decay kinematics. Similarly, the $D_s \rightarrow \pi^- \pi^+ \pi^+$ peak is wider than the peak of the lighter D^+ meson decaying into the same final state.

The tail parameters resulting from our fit also confirm our physics expectations. We expect the decay to lower mass states, $D^+ \rightarrow \pi^- \pi^+ \pi^+$, to produce a final state photon more often than $D^+ \rightarrow K^- \pi^+ \pi^+$, due to higher amount of energy freed in the decay. Indeed, the $\pi\pi\pi$ decay has larger fraction of events in the tail. We also see that D_s^+ radiates more than D^+ . This too is expected, as the D_s^+ is heavier than D^+ and therefore leaves more energy to the final state.

In the fit to the data (Section 8.4), we keep the shape and the relative size of the radiative tails fixed, while letting most of the other signal shape parameters float.

Figure 8.6: Signal shapes: $D^+ \rightarrow K^- \pi^+ \pi^+$ (top) and $D^+ \rightarrow \pi^- \pi^+ \pi^+$ (bottom).

Figure 8.7: $D_s \rightarrow \pi^- \pi^+ \pi^+$ peak fit template.

Parameter	$K^-\pi^+\pi^+$	$\pi^-\pi^+\pi^+$	
		D^+	D_s^+
$m(\text{MeV})$	1868.08 ± 0.01	1867.67 ± 0.02	1966.96 ± 0.03
$\sigma_N(\text{MeV})$	6.20 ± 0.03	7.29 ± 0.04	7.70 ± 0.06
$\frac{\sigma_W}{\sigma_N}$	1.94 ± 0.02	1.84 ± 0.02	2.03 ± 0.06
$f_w(\%)$	16.3 ± 0.7	19.5 ± 1.1	11.9 ± 1.3
$a_{rad}(\text{MeV})$	40.9 ± 0.9	45.7 ± 0.9	26.4 ± 1.6
$f_{rad}(\%)$	3.34 ± 0.06	5.28 ± 0.08	6.69 ± 0.26

Table 8.1: Fit parameters from the signal shape template, for $D^+ \rightarrow \pi^-\pi^+\pi^+$, $D^+ \rightarrow K^-\pi^+\pi^+$ and $D_s \rightarrow \pi^-\pi^+\pi^+$ decays.

8.4 Data Fit

After putting all the mass fit components together, our fitting function (FF) takes the following shape:

$$FF = N_{CBG} \cdot P_2 + N_{D^+} \cdot R_{D^+} + N_{D_s^+} \cdot R_{D_s^+} + N_{SIG} \cdot F_{SIG}, \quad (8.3)$$

where $N_{CBG/D^+/D_s^+}$ are the norms of the combinatorial background/ D^+ reflections/ D_s^+ contribution. N_{D^+} is determined from the $K\pi\pi$ reflection and $N_{D_s^+}$. F_{SIG} is the signal shape function and N_{SIG} is the signal normalization, that is, the yield of the D^+ signal decays.

The relative normalizations of various backgrounds (combinatoric background, D^+ and D_s^+ decays) are left free in the fit. We also let float several signal shape parameters. For the $K\pi\pi$ fit, these free parameters are: the signal norm (N_{SIG}), mass of the D^+ (M_{D^+}), width of the narrower of the two gaussians (σ_N), ratio of the widths of the wide and narrow gaussians ($\frac{\sigma_W}{\sigma_N}$), and the fraction of the events in the wide gaussian (f_W). In the case of the $\pi\pi\pi$ fit, the free-floating fit parameters are:

signal norm (N_{SIG}), D^+ mass (M_{D^+}) and width (σ_N) of the narrower gaussian of the signal peak, norm and position of the $K\pi\pi$ reflection, and norm and width (N_{D_s} and σ_N) of the $D_s \rightarrow \pi^-\pi^+\pi^+$ decay.

To make the fit as robust and stable as possible, we adopt the following fitting procedure. We begin fitting with just the overall background norms (N_{CB} , N_{D^+} , N_{D_s}) and signal norm free, and the rest of the parameters fixed from the Monte Carlo. We then reiterate the fit several times, each time letting free one additional parameter. This way, the resulting many-parameter fit converges well, without any limits being imposed on the floating parameters.

The final data fits are shown in Figures 8.8 and 8.9. To better judge the quality of the fit, we also plot the residuals, i.e. subtract the value of the fit function from the histogram bin content and plot it divided by the statistical error on the histogram bin content (Figures 8.10 and 8.11). From these we see that the fits are satisfactory, especially in the signal region. Most of the contribution to the χ^2 of the fit comes from the complex background fits in regions far removed from the signal region. These do not affect our branching ratio result.

Parameters describing the two signal modes are listed in Table 8.2.

Parameter	$D^+ \rightarrow K^-\pi^+\pi^+$	$D^+ \rightarrow \pi^-\pi^+\pi^+$
$N(\times 10^3)$	1473.9 ± 1.5	44.24 ± 0.48
$m(\text{MeV})$	1868.430 ± 0.008	1868.15 ± 0.09
$\sigma_N(\text{MeV})$	6.54 ± 0.03	7.793 ± 0.09
$\frac{\sigma_w}{\sigma_N}$	1.78 ± 0.01	—
$f_w(\%)$	30.0 ± 1.0	—

Table 8.2: Fit parameters for the signal peaks, $D^+ \rightarrow \pi^-\pi^+\pi^+$ and $D^+ \rightarrow K^-\pi^+\pi^+$ decays. The errors are statistical. The numbers that are left out are fixed from Monte Carlo; see Table 8.1.

As is clear from Figures 8.12 and 8.13, D_s^+ decays occupy both signal regions, and overlap with the radiative tails of the signal peaks. This fact is the primary motivation behind our decision to not let the tail parameters float freely. For the same reason, we keep the relative contributions of D_s^+ decays fixed.

We arrive at the central value for $N_{\pi\pi\pi}/N_{K\pi\pi}$ of 3.002%, with a relative statistical error of 1.09%.

$$N_{\pi\pi\pi} = (44.24 \pm 0.48) \times 10^3 \quad (8.4)$$

$$N_{K\pi\pi} = (1473.9 \pm 1.5) \times 10^3 \quad (8.5)$$

$$N_{\pi\pi\pi}/N_{K\pi\pi} = (3.002 \pm 0.033)\% \quad (8.6)$$

8.5 Systematic Uncertainties

We now evaluate the systematic uncertainties associated with the decay yields, or more precisely with the signal shapes. We quote the mean variation in $N_{\pi\pi\pi}/N_{K\pi\pi}$ for every effect considered. The uncertainties associated with the fitting procedure turn out to be relatively small.

8.5.1 Treatment of signal width parameters

Despite our insistence on treating the two D^+ decay channels as similarly as possible, we are led to treat the signal peaks differently in the data fits. In $K\pi\pi$, we leave the ratio of the widths of the two Gaussians ($\frac{\sigma_w}{\sigma_N}$), and the fraction of D^+ 's in the wide Gaussian (f_w) free to float. Doing so improves the quality of the fit, and there is no physics reason to constrain them. However, if we release these parameters in the $\pi\pi\pi$

fit, the fit yields an unphysical result: the wide Gaussian ends up accommodating 91% of the D^+ 's. Apparently, the relatively high background levels under the D^+ peak make it difficult to determine with precision the parameters of both gaussians. Hence, for the nominal fit outcome, we fix the $\frac{\sigma_W}{\sigma_N}$ and f_w of the $\pi\pi\pi$ peak, thereby adopting different treatment of the signal peaks' width parameters. This introduces a systematic uncertainty into the measurement of the yields, which obviously does not cancel in the ratio. The difference in $D^+ \rightarrow K^-\pi^+\pi^+$ yields obtained with fixed and with released width parameters is a good measure of this uncertainty. Refer to Table 8.3 for the values.

Model	$N_{\pi\pi\pi}$	$N_{K\pi\pi}$	$N_{\pi\pi\pi}/N_{K\pi\pi} \times 10^{-2}$
central: $K\pi\pi$ $\frac{\sigma_W}{\sigma_N}$, f_w free	44242	1.474×10^6	3.002
$K\pi\pi$ $\frac{\sigma_W}{\sigma_N}$, f_w fixed from MC	44242	1.473×10^6	3.003
relative uncertainty (%)	0.03		

Table 8.3: Systematic uncertainties associated with fixing and releasing $D^+ \rightarrow K^-\pi^+\pi^+$ signal $\frac{\sigma_W}{\sigma_N}$ and f_w .

8.5.2 Radiative tail

The shape of the radiative tail simulated in the Monte Carlo also carries a degree of uncertainty, due to the limited adequacy of our understanding and consequently our ability to model these effects with high precision. First, there is an uncertainty of the accuracy with which PHOTOS describes final state radiative processes in hadronic final states. Additionally, there is an uncertainty of the amount of the CDF detector material and thereby of the rate of Bremsstrahlung radiation that particles undergo inside it. The material uncertainty is considerable, amounting to up to 20%. To account for these uncertainties, we vary the size of the tails by $\pm 30\%$. (Similar 30%

uncertainty on FSR is quoted in one of the latest CLEO-c papers, [34]. For further justification, refer to [35].) Since the physics governing the radiative properties in the two channels is the same, under- or over-estimating one tail will result in proportional effect in the other. To see how the branching ratio changes with varying the size of the tails, refer to Table 8.4.

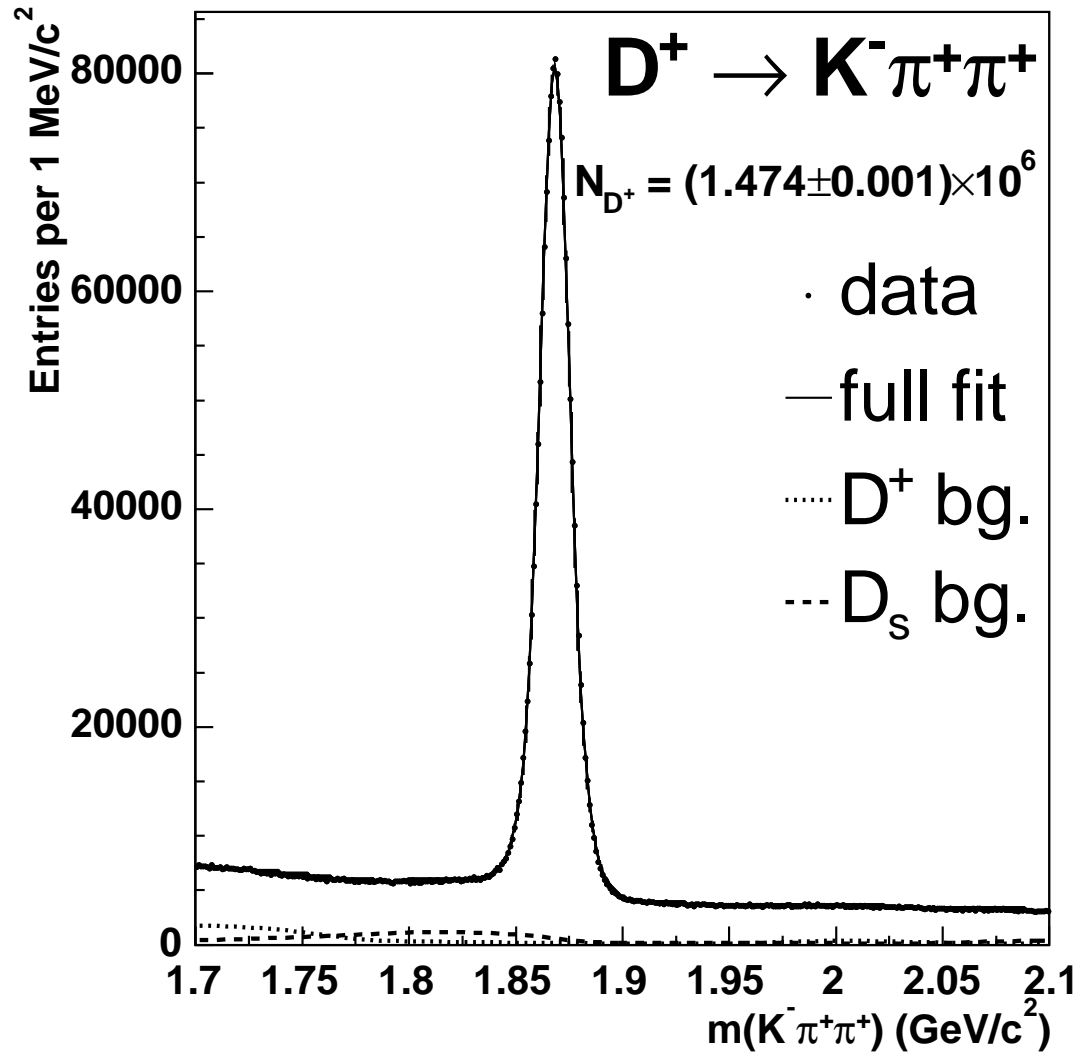
Model (f_{tail} value)	$N_{\pi\pi\pi}$	$N_{K\pi\pi}$	$N_{\pi\pi\pi}/N_{K\pi\pi} \times 10^{-2}$
central value (C.V.)	44247	1.474×10^6	3.002
- 30% C.V.	43670	1.465×10^6	2.981
+30% C.V.	44799	1.483×10^6	3.021
relative uncertainty (%)	0.67		

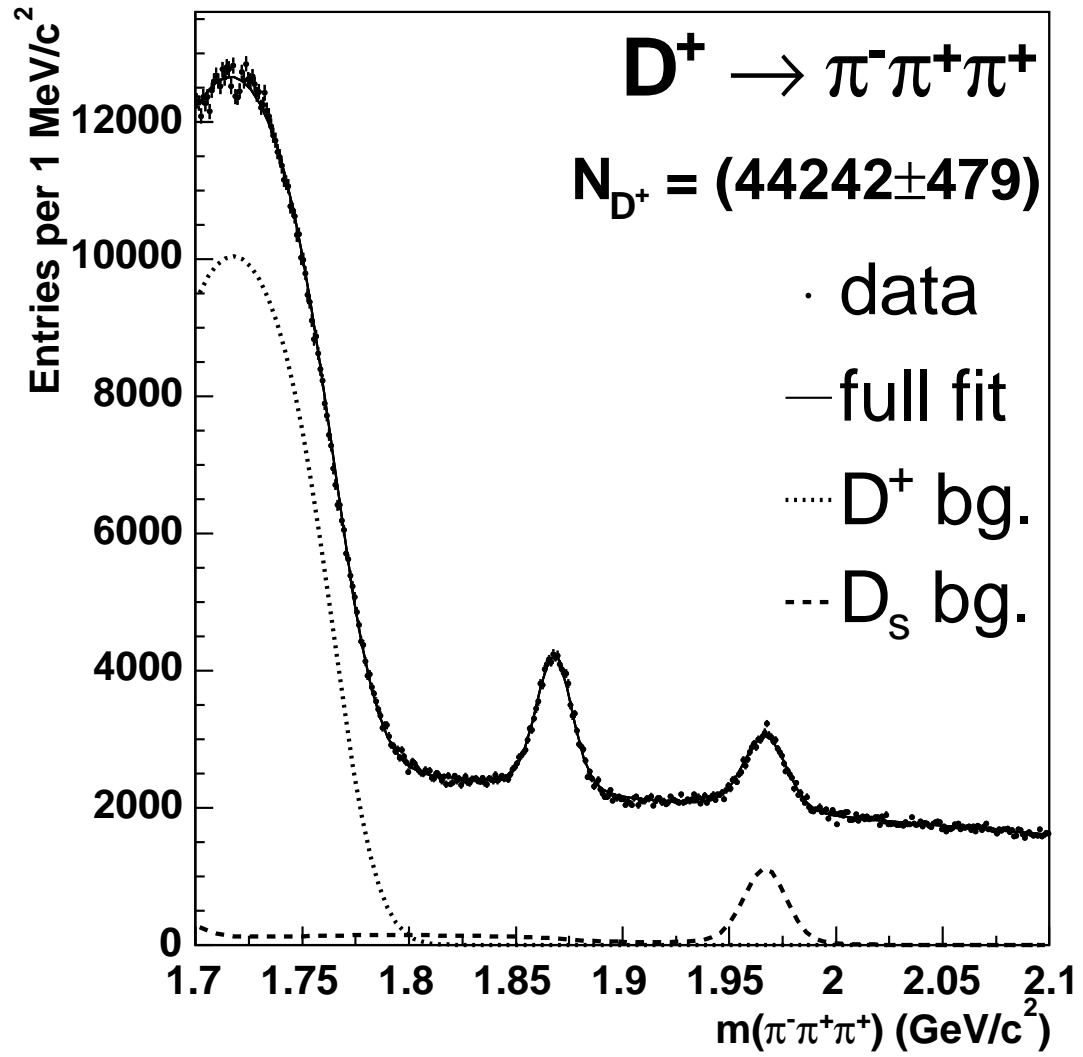
Table 8.4: Systematic uncertainties associated with the size of the signal peaks' radiative tails.

8.5.3 Systematic Uncertainties of Yields: Summary

The dominant systematic error of the measurement of the yields ratio results from the uncertainty with which we simulate the radiative processes. The different treatment of signal width parameters has a very small effect on our measurement. The biggest uncertainty of the yields ratio is statistical, coming from the limited sample sizes of the data and Monte Carlo, and amounting to 1.09%.

$$N_{\pi\pi\pi}/N_{K\pi\pi} = (3.002 \pm 0.033(stat) \pm 0.020(syst))\% \quad (8.7)$$

Figure 8.8: $D^+ \rightarrow K^- \pi^+ \pi^+$ data fit.

Figure 8.9: $D^+ \rightarrow \pi^- \pi^+ \pi^+$ data fit.

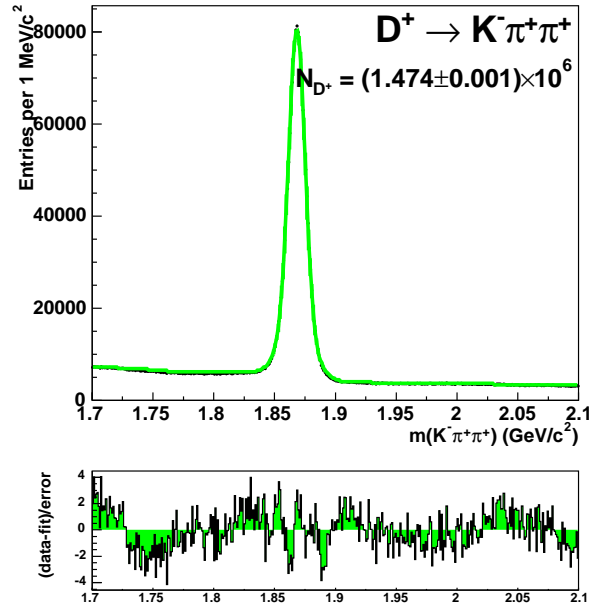


Figure 8.10: Residuals of the $D^+ \rightarrow K^-\pi^+\pi^+$ data fit. No systematic trends are observed, and the largest residuals tend to occur in the regions far from the signal peak.

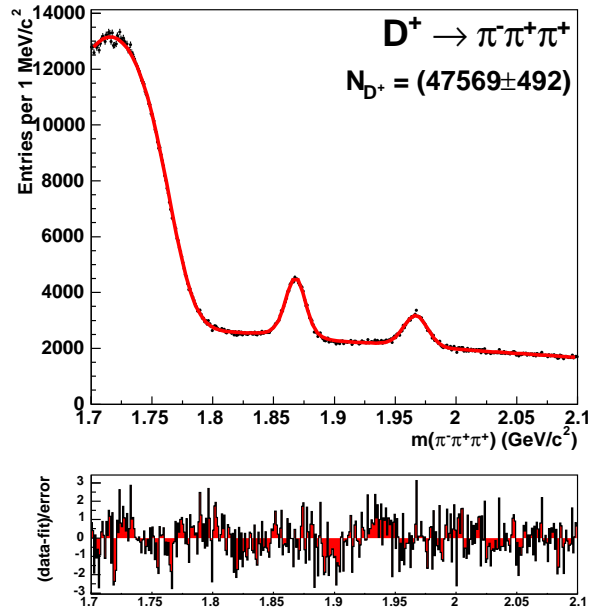


Figure 8.11: Residuals of the $D^+ \rightarrow \pi^- \pi^+ \pi^+$ data fit. No systematic trends are observed, and the largest residuals tend to occur in the regions far from the signal peak.

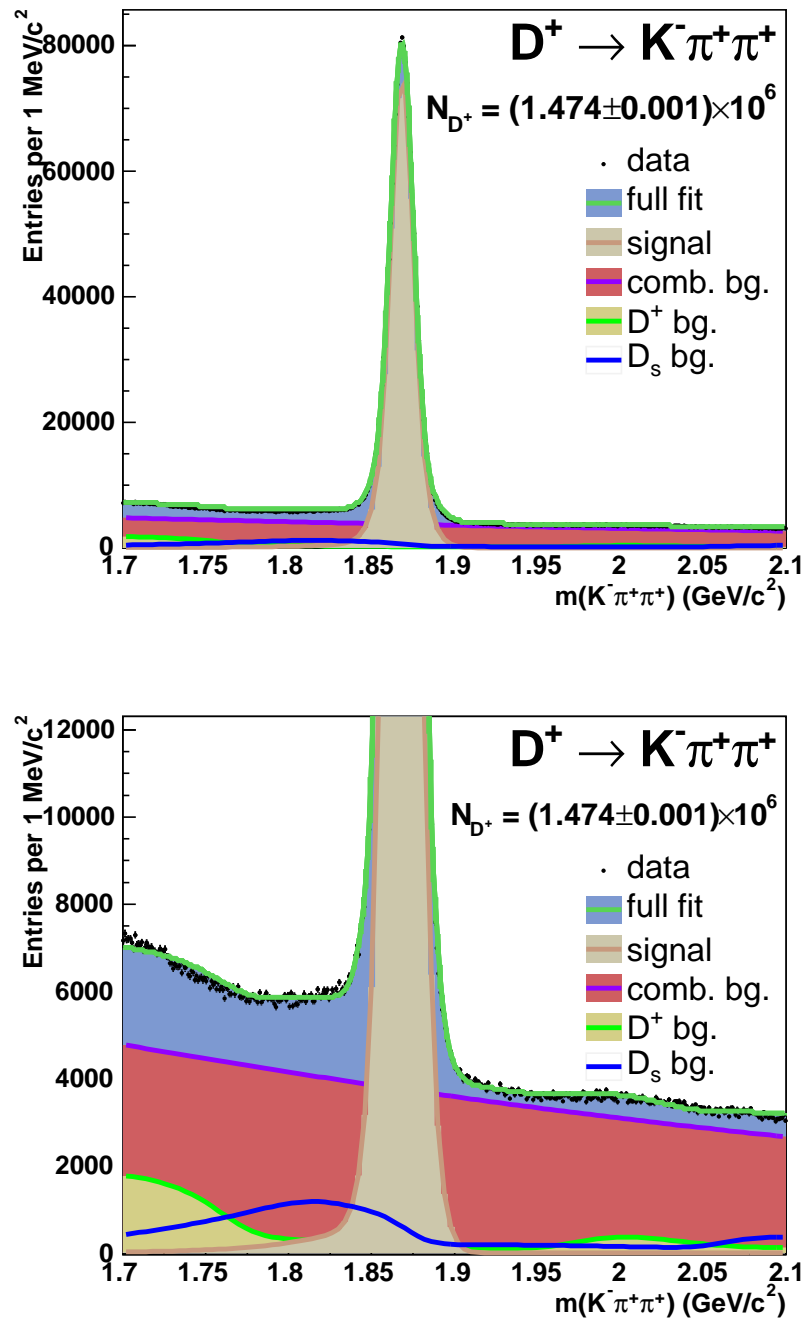


Figure 8.12: $D^+ \rightarrow K^- \pi^+ \pi^+$ data fit, with reflections contributions emphasized. All the contributions add up to form the area under the topmost green line.

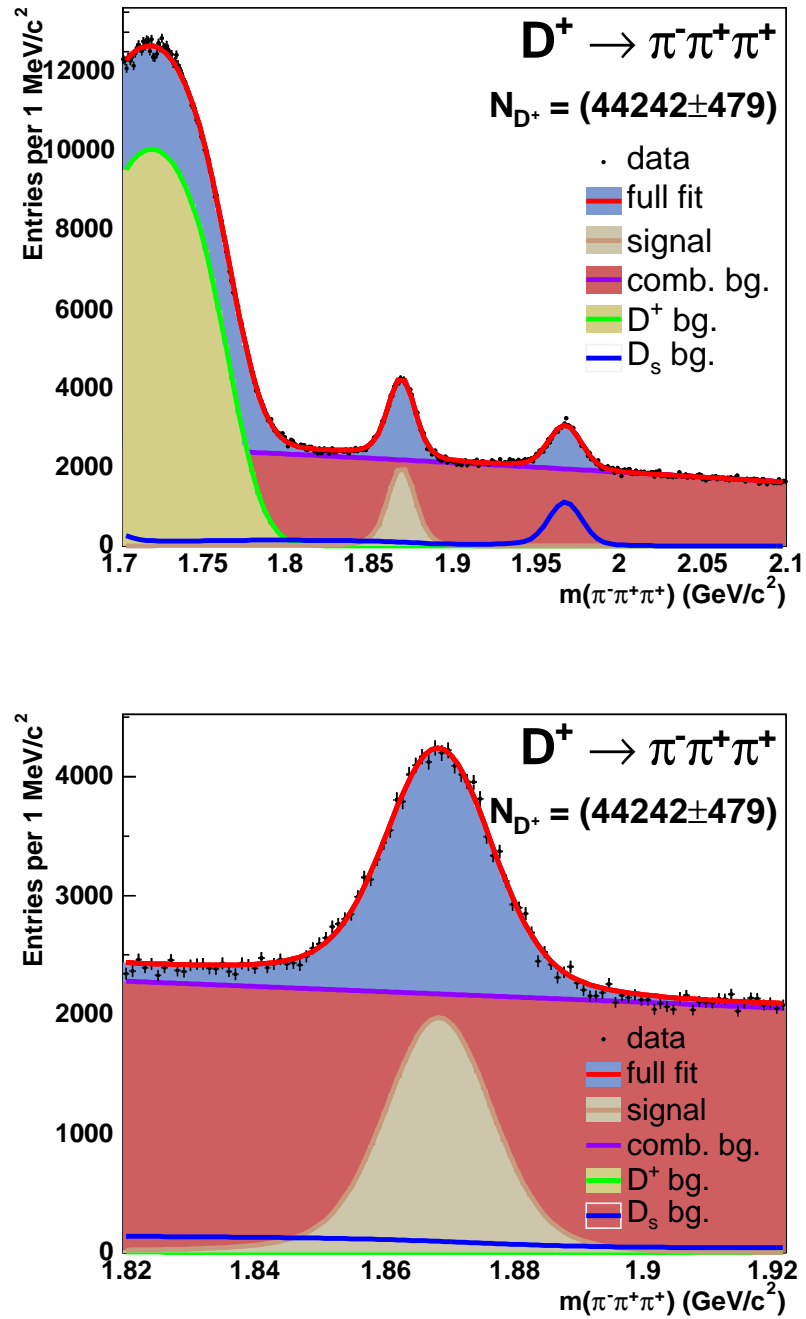


Figure 8.13: $D^+ \rightarrow \pi^- \pi^+ \pi^+$ data fit, with reflections contributions emphasized. All the contributions add up to form the area under the topmost red line.

Chapter 9

Relative Efficiencies

We now turn to measuring $\frac{\varepsilon(K\pi\pi)}{\varepsilon(\pi\pi\pi)}$, the relative efficiency of the two decays. To extract it, we again use the Monte Carlo simulation, because it allows us to keep track of events that get lost during reconstruction or signal extraction. We count the fraction of the generated Monte Carlo events that survive the simulation, reconstruction, and the candidate selection. This procedure gives a reasonable first order measurement of the relative efficiency. Note that, for all efficiency studies, we weight the Monte Carlo to mimic the dynamic trigger prescaling of the data. The method by which we determine the prescale factors is described in Section 9.1.

To refine the relative efficiencies measurement, we derive corrections for the effects which are not well reproduced by the Monte Carlo. These include:

- Dalitz structure of the decays (Section 9.2)
- XFT efficiencies of K and π (Section 9.3)
- D^+ lifetime (Section 9.4)
- D^+ p_T spectrum (Section 9.5)

Systematic uncertainties of the relative efficiency measurement are discussed in Section 9.6.

9.1 Trigger Prescale Factors

In making our Monte Carlo samples, we use the fact that the trigger paths differ only by the tightness of their requirements: the events that satisfy the High p_T trigger criteria are a subset of those that satisfy the Scenario A, which in turn satisfy the Low p_T criteria. At the time of Monte Carlo simulation, we require that the events pass the trigger requirements of only the loosest trigger path - the `BCHARM_LOWPT`. Trigger confirmation allows us to later classify the Monte Carlo events by the trigger they would pass if given all three `BCHARM` paths. Upon applying the trigger confirmation, we split the Monte Carlo sample into three subsamples, each corresponding to one of the trigger paths used in this analysis. However, the triggers used for collecting the data are dynamically prescaled: they don't accept every event that satisfies the requirements, but instead only every $1/\text{PF}$ 'th event, where PF is the trigger path's prescale factor. As explained in Section 5.1.3, the prescale factors, and therefore the rate of acceptance, changes with the beam conditions. In accordance with their unprescaled rates, the `BCHARM_LOWPT` path is prescaled more than the Scenario A, while `BCHARM_HIGHPT`, the tightest path, is not prescaled at all. Therefore, the simple Monte Carlo trigger subsamples do not correspond to the data; using them without correction would result in yield ratios different from those of the data. We correct this situation by reweighting the Monte Carlo by the trigger prescale factors.

We determine the prescale factors from our data. Because the prescaling is dynamic, the factors change from run to run. Recall that we divide our data by the

time of collection into seven discrete periods (Table 5.1), due to the changes in the detector configuration and trigger conditions. To each of the seven periods, we assign a prescale factor averaged over that time interval. Note that the first two data-taking periods are different from the rest, as there was only one BCHARM trigger path (Scenario A) and no prescaling at the time.

For each of the prescaled triggers (Low p_T or Scenario A) in any time period, we find the prescale factor as the ratio of the D^+ yields: those passing both the prescaled and non-prescaled trigger (High p_T), and those passing the non-prescaled trigger.

$$PF_{PRESC\ TRIG} = \frac{N(D^+)_{PRESC\ TRIG} \&\& NONPRESC\ TRIG}{N(D^+)_{NONPRESC\ TRIG}} \quad (9.1)$$

To understand how this ratio shows the prescaled trigger’s rate of acceptance of eligible events, recall that any event satisfying the nonprescaled trigger will also be satisfying the prescaled trigger requirements. The resulting prescale factors can be found in Table 9.1. As can be expected, the Low p_T factors are consistently lower than Scenario A.

Trigger	Time Period						
	1	2	3	4	5	6	7
BCHARM (scenario A)	1.0	1.0	0.805	0.991	0.968	0.990	0.982
BCHARM_LOWPT	0	0	0.158	0.547	0.700	0.872	0.686
BCHARM_HIGHPT	0	0	1.0	1.0	1.0	1.0	1.0

Table 9.1: Prescale factors for the two prescaled triggers, averaged over time for each of the data-taking time periods. The first two periods are trivial because there was only one BCHARM trigger employed at the time, and it was not prescaled.

For the overall efficiency ratio $\frac{\varepsilon(\pi\pi\pi)}{\varepsilon(K\pi\pi)}$ quoted in the row “ALL” of Table 9.2, prescale factors from Table 9.1 are folded in.

9.2 Dalitz Structure

The resonant structures of the two decays significantly influence their kinematics, and hence their efficiencies. Recall that the BGenerator, which we use to generate the Monte Carlo, implements models of Dalitz structure based on old measurements made with small decay samples. Because of this, we generate our Monte Carlo as uniformly distributed across Dalitz phase space and correct for the resonant structure ourselves. We reweight the Monte Carlo based on our own $D^+ \rightarrow \pi^- \pi^+ \pi^+$ and $D^+ \rightarrow K^- \pi^+ \pi^+$ data Dalitz plots. We first perform a two-dimensional fit of our data, using resonance masses and phases reported by the E791 studies of $D^+ \rightarrow \pi^- \pi^+ \pi^+$ and $D^+ \rightarrow K^- \pi^+ \pi^+$ decays ([7], [32]). We then apply the resulting amplitudes as weights to each of the Monte Carlo signal events. More information about the E791 studies and the variables we take over can be found in Section 6.2.

The reweighting procedure results in relative efficiency decrease of about 4.4%. The agreement between data and Monte Carlo Dalitz variables can be seen in Figures 6.4 and 6.3

To interpret the numbers, it helps to be aware of another effect, independent of the resonant decay structure: the "sculpting" of the Dalitz space by triggers. Sculpting here means that some events get favored over others, based on their position in the phase space, because the trigger acceptance rate depends on the track kinematics, which obviously varies over Dalitz phase space. The sculpting effects are clearly visible on the plots in Figure 9.1, made using the Monte Carlo before the Dalitz reweighting, that is, events that were generated uniform across the Dalitz phase space. The triggers that require opposite charge tracks, BCHARM_HIGHPT and BCHARM (Scenario A) sculpt the space more, and differently, than the BCHARM_LOWPT. Both $\pi\pi\pi$ and $K\pi\pi$ channels

suffer losses of candidates with the opposite charged triggers, but for $\pi\pi\pi$ the effect is stronger, due to the fact that most of its resonances reside in the disfavored, low invariant mass corner of the phase space. Having more of the resonances in the disfavored region results in the larger combined effect of the Dalitz weighting and trigger sculpting.

Trigger	$\varepsilon(\pi\pi\pi)/\varepsilon(K\pi\pi)$	
	no Dalitz weighting	with Dalitz weighting
BCHARM_HIGHPT	0.8375	0.8186
BCHARM (scenario A)	0.8532	0.842
BCHARM_LOWPT	0.9375	0.8734
ALL	0.9201	0.8673

Table 9.2: Relative efficiencies before and after Dalitz reweighting, sorted by the trigger sample.

Trigger	$\varepsilon(\pi\pi\pi)$ (%)	
	no Dalitz weighting	with Dalitz weighting
BCHARM_HIGHPT	0.09333	0.0827
BCHARM (scenario A)	0.1688	0.1517
BCHARM_LOWPT	0.3366	0.3227
ALL	0.2805	0.2659

Table 9.3: Absolute efficiency of the $\pi\pi\pi$ channel before and after Dalitz reweighting, sorted by the trigger sample.

We estimate the uncertainty of this method of Dalitz reweighting in Section 9.6.1.

9.3 XFT efficiencies

As they move through the gas inside the central tracker, kaons and pions exhibit different ionization properties. Pions ionize more than kaons, they produce more

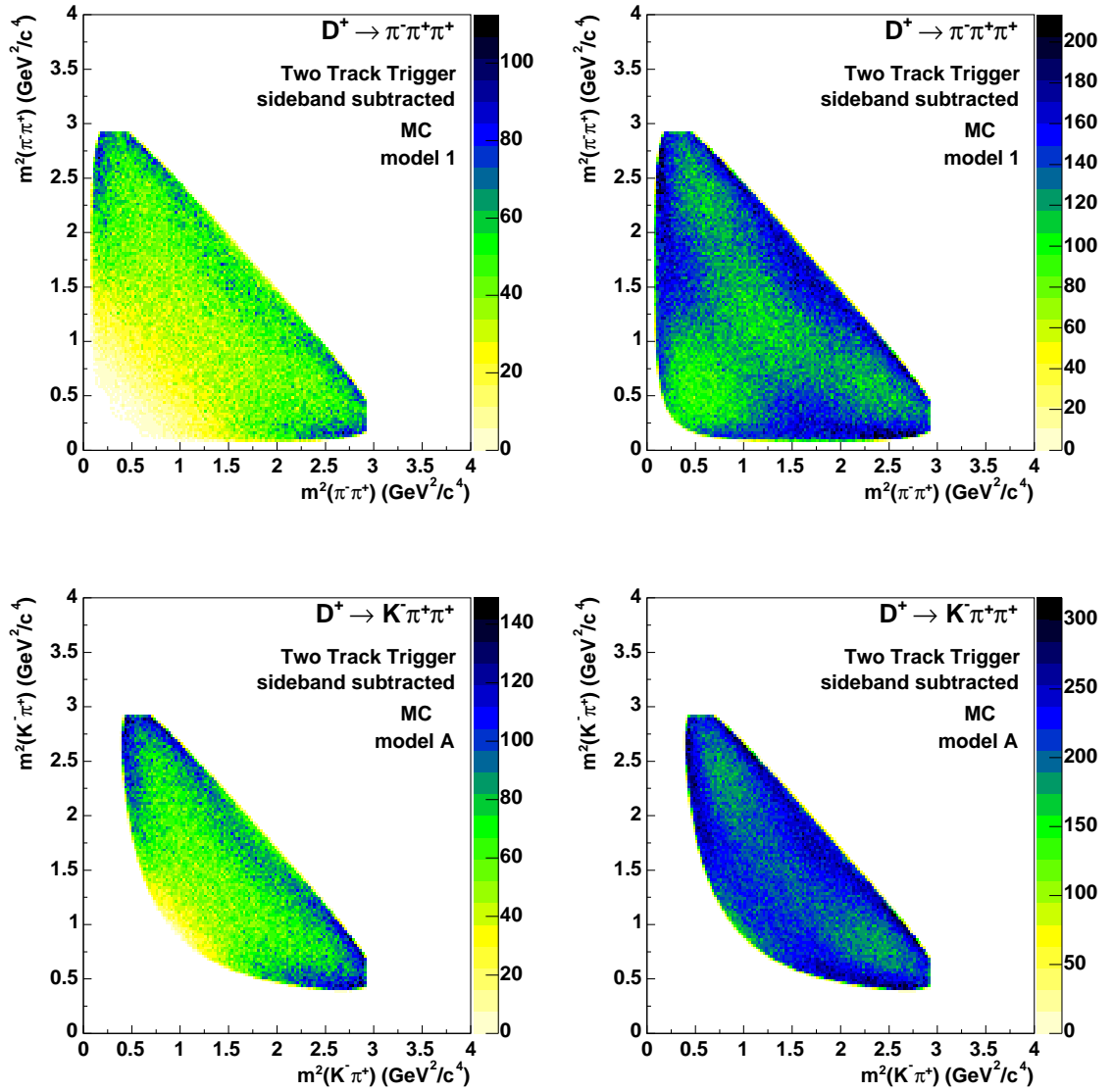


Figure 9.1: Trigger sculpting of the Dalitz space, $\pi\pi\pi$ on top and $K\pi\pi$ on bottom, for the opposite charge BCHARM_HIGHPT trigger (left side) and for BCHARM_LOWPT trigger (right side). The Monte Carlo used here is uniformly distributed over the phase space, but the triggers have different acceptance rate for different regions of the phase space.

Trigger	$\varepsilon(K\pi\pi)$ (%)	
	no Dalitz weighting	with Dalitz weighting
BCHARM_HIGHPT	0.1114	0.101
BCHARM (scenario A)	0.1978	0.1802
BCHARM_LOWPT	0.359	0.3695
ALL	0.3049	0.3066

Table 9.4: Absolute efficiency of the $K\pi\pi$ channel before and after Dalitz reweighting, sorted by the trigger sample.

signal in the drift chamber and therefore have more chance to register a hit. But the XFT trigger has a threshold of the number of COT hits required of a track. It therefore collects the two channels with slightly different efficiencies. If left unchecked, this can bias our measurement toward the $\pi\pi\pi$ channel.

The Monte Carlo does not reproduce this discrepancy well, as can be seen in Figure 9.2. The plots show kaon and pion XFT efficiencies, namely $\frac{N_{PASS}}{N_{PASS}+N_{FAIL}}$, sideband subtracted and plotted as function of track parameters, for period 7 of data taking. (Since XFT configuration was changing during the data taking, we divide the data by time periods for this study). The kaon and pion track distributions are shown in red and blue respectively. While the two differ for data, they are almost identical for Monte Carlo.

The number of COT hits depends on more than one of the track variables (track momentum, track polar angle θ , and even ϕ due to the COT aging, that is, coating of the drift wires that builds up with time and reduces the efficiency of the tracks). Because of this, no single one of the five track parameters is a good choice of variable as a function of which to study the efficiency. We would have to consider their correlations. The reason for this complicated dependence of efficiency on the track parameters is that the number of drift chamber hits essentially depends on the energy

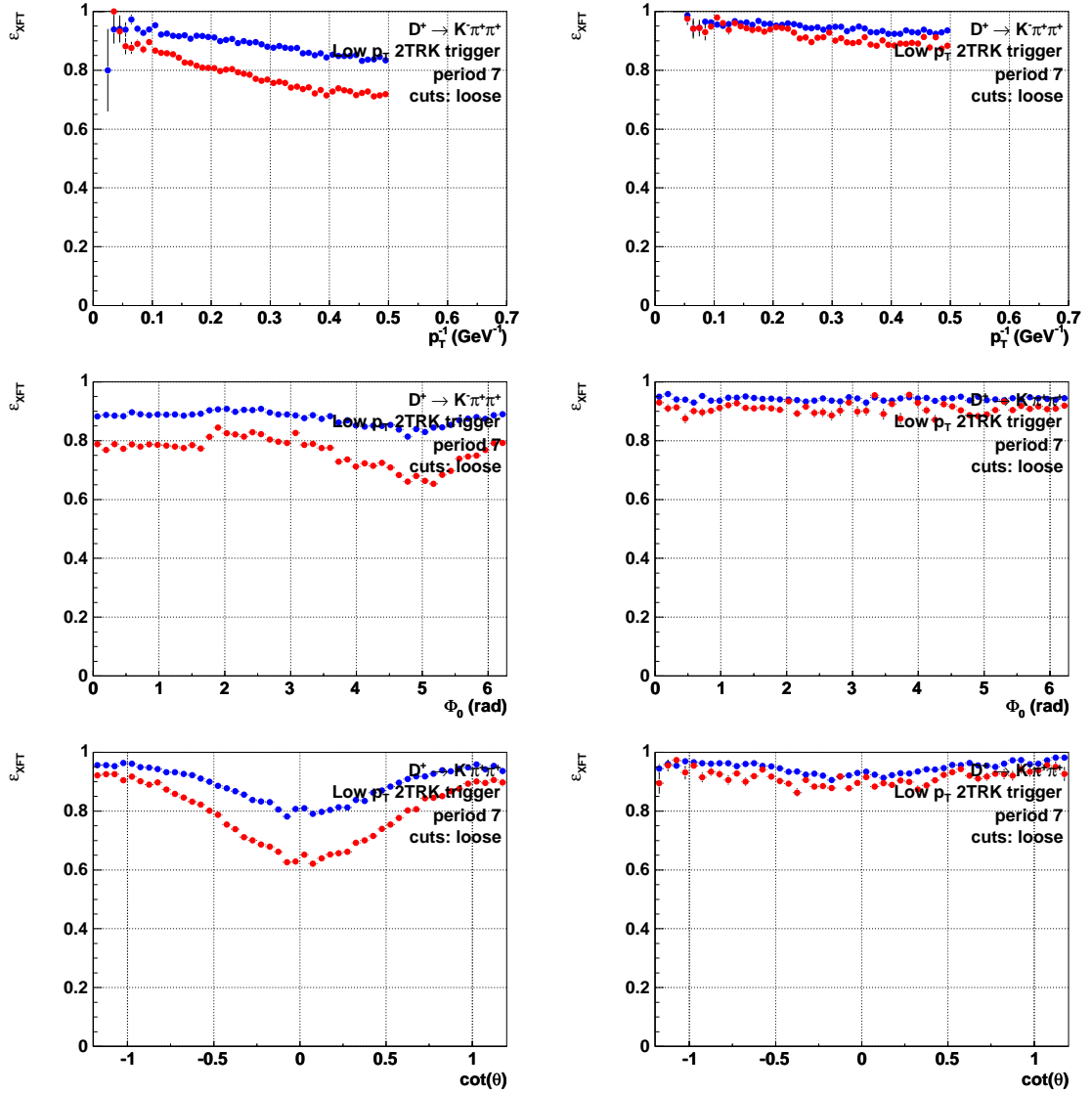


Figure 9.2: XFT efficiency dependence on the track variables p_T , ϕ_0 and $\cot(\theta)$, for kaons (red) and pions (blue), recorded during data-taking period 7. Data plots are on the left and Monte Carlo on the right.

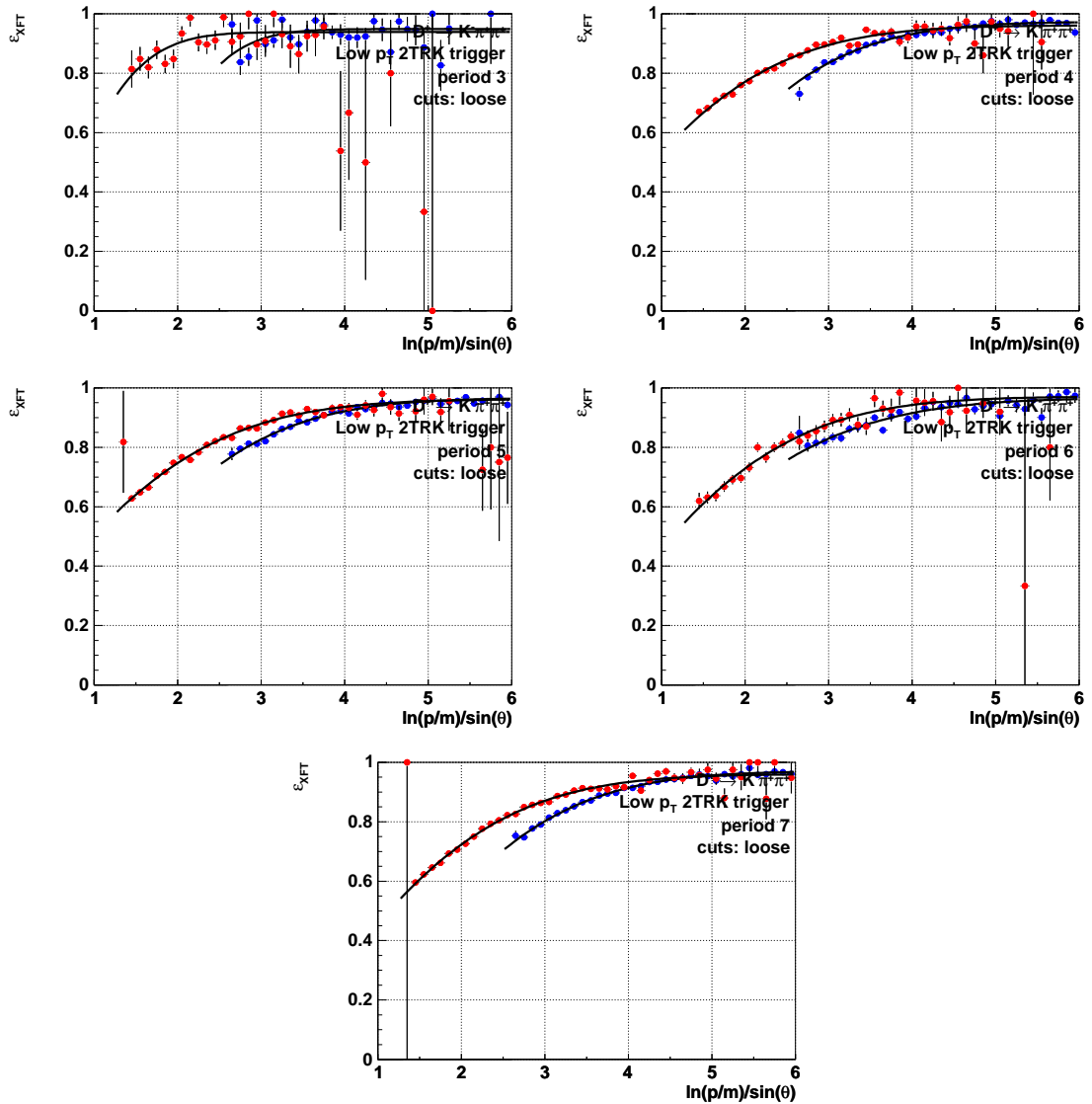


Figure 9.3: XFT efficiency dependence on $E_{loss} = \ln(p/m)/\sin(\theta)$ variable, for kaons (red) and pions (blue), periods 3 to 7.

the particle deposits while ionizing the surrounding gas. This quantity, which we call E_{loss} , is a function of track parameters θ and p_T , and is given by the Bethe-Bloch formula. In the high momentum limit that applies here, it can be simplified to:

$$E_{loss} = \ln(p/m)/\sin(\theta) \quad (9.2)$$

The efficiency dependence on E_{loss} for kaons and pions for the seven different data taking periods is plotted in the Figure 9.3. As E_{loss} depends on mass of the ionizing particle, the pion and kaon efficiency curves do not overlap in E_{loss} range.

We now implement the procedure to drop the fraction of Monte Carlo events that is in excess of the XFT accepted data. We need a set of kaon and pion tracks that is unbiased by the XFT trigger selection. Because $D^+ \rightarrow K^-\pi^+\pi^+$ is a three body decay containing both K and π tracks, and the BCHARM paths require only two trigger tracks, we can extract these unbiased tracks from our $D^+ \rightarrow K^-\pi^+\pi^+$ sample. High p_T and Scenario A paths require the trigger tracks to have opposite charge, hence the kaon of the $D^+ \rightarrow K^-\pi^+\pi^+$ decay will always be trigger track for those paths, and will never be unbiased by the selection. We therefore use Low p_T path, which has no opposite charge requirement and therefore allows both kaons and pions as trigger tracks. Whichever two D^+ daughters fire the Low p_T trigger, the third one is XFT-unbiased, regardless of whether it, too, fired another trigger in combination with one more track. By checking the trigger bits and confirming the trigger requirements, we extract a set of XFT-unbiased kaon and pion tracks. We use only tracks from this unbiased set in all discussions in this Section.

For each period, we fit the sideband subtracted efficiency distribution to a three

parameter error function of E_{loss} :

$$\varepsilon_{XFT}(E_{loss}) = A \cdot Erf((E_{loss} - B) \cdot C) \quad (9.3)$$

We do this for both data and Monte Carlo. Note that the first two time periods are exempt from this procedure, as there was no Low p_T trigger during early data taking.

We extract the fit parameters, A, B and C, for data and for Monte Carlo. Then, for each Monte Carlo track and its E_{loss} value, we calculate

$$\frac{\varepsilon_{XFT}^{DATA}(E_{loss})}{\varepsilon_{XFT}^{MC}(E_{loss})}, \quad (9.4)$$

ratio of the efficiencies parametrized as data and as Monte Carlo. We compare this ratio to a randomly drawn number. If the ratio is bigger than the random number, we keep the track, if it is not, we drop it, that is, we take it out of consideration when determining efficiencies.

This is effectively a “hit and miss” procedure. The corrections differ from period to period, and amount to about 6% overall increase. We discuss the uncertainties associated with this procedure in Sections 9.6.2 and 9.6.3.

9.4 D^+ Lifetime Correction

The D^+ meson lifetime used by the BGenerator for Monte Carlo generation, $c\tau = 315.0 \mu m$, does not come from the best available measurement. The PDG [8] reports as best value to date $c\tau = 311.8 \pm 2.1 \mu m$. We use this value to reweight all Monte

Carlo histogram entries by the lifetime weight factor:

$$\frac{c\tau_{BGEN}}{c\tau_{PDG}} \cdot \frac{\exp(-ct/c\tau_{PDG})}{\exp(-ct/c\tau_{BGEN})} \quad (9.5)$$

This results in a slight ($< 0.1\%$) correction to the relative efficiency.

9.5 $P_T(D^+)$ Spectrum Correction

Compared with the data of $D^+ \rightarrow \pi^-\pi^+\pi^+$ and $D^+ \rightarrow K^-\pi^+\pi^+$ decays, the Monte Carlo D^+ p_T spectra tend to be shifted toward the lower values of transverse momentum. In other words, the BGenerator transverse momentum spectra do not correspond to what we see in the data. To correctly estimate the relative efficiency, we need Monte Carlo that is as similar as possible to the data. We correct for this discrepancy by rescaling the Monte Carlo p_T spectrum.

Using the large sample $D^+ \rightarrow K^-\pi^+\pi^+$ decay mode, we produce a histogram of which each bin is a ratio of the p_T values of the data and Monte Carlo for the same bin. The p_T ratio distribution obtained in this way can be fitted with an exponential plus a linear function of the p_T . Figure 9.5 shows the result of this fit. We use the fit parameters to rescale the Monte Carlo spectrum. The resulting efficiency correction amounts to 0.16% effect (Table 9.9). We thus derive the central value of our efficiency measurement from Monte Carlo p_T spectra corrected according to the $K\pi\pi$ data.

The overlays of the data and the corrected Monte Carlo p_T spectra are shown in Figure 9.4. The Figures show the Monte Carlo spectrum of the $\pi\pi\pi$ channel still noticeably shifted toward lower values, even after applying the $K\pi\pi$ -derived

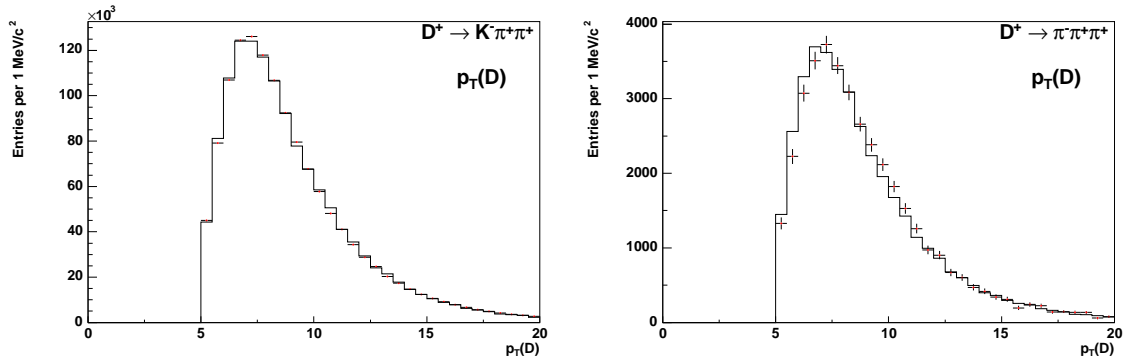


Figure 9.4: Data - Monte Carlo comparison of transverse momentum of the D^+ in $K^-\pi^+\pi^+$ (left) and $\pi^-\pi^+\pi^+$ (right) decays. Plots indicate that, even after the correction, Monte Carlo deviates from data by being generally shifted toward lower p_T values.

correction. The $K\pi\pi$ and $\pi\pi\pi$ channels differ in this respect, requiring that we assign a systematic uncertainty that accounts for the difference (Section 9.6.4).

9.6 Systematic Uncertainties of Relative Efficiency

We now evaluate the systematic uncertainties associated with the relative efficiency, $\frac{\varepsilon(\pi\pi\pi)}{\varepsilon(K\pi\pi)}$. We quote the largest deviation from the central value, unless otherwise noted.

The sum of all systematic errors can be found in Table 9.12.

9.6.1 Uncertainty of Dalitz Weighting

To make the Monte Carlo resonant structure correspond to that of the data, we used the E791-reported resonances to fit our data, and applied the resulting amplitudes and phases as weights to our Monte Carlo (Section 9.2). To estimate the uncertainty of this Dalitz weighting of Monte Carlo, we perform the same Dalitz fits on our data

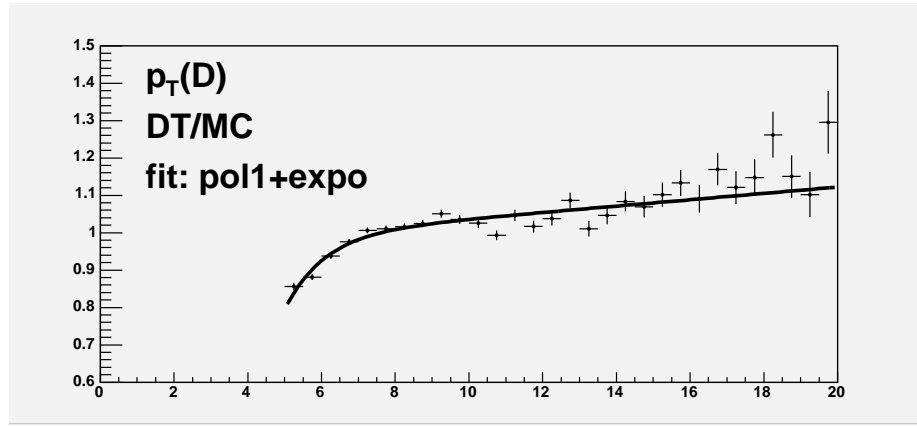


Figure 9.5: Ratio of data and Monte Carlo p_T spectra of the D meson, as derived from $D^+ \rightarrow K^- \pi^+ \pi^+$ decay, and fitted to an exponential plus a first order polynomial.

but this time without the σ and κ resonances, the existence and properties of which have been proposed but not validated so far. As in the original procedure, we weight the Monte Carlo with the resulting fit functions. The overlays of data and resulting Monte Carlo mass projections are shown in Figures 9.6 and 9.7. For each channel, we take the deviation between the efficiency derived in this way and the central value of efficiency (that is, using fits with σ and κ resonances) to be the systematic uncertainty (Tables 9.5 and 9.6). Since the Dalitz structures of the two decays are independent, the corresponding uncertainties of the Dalitz weighting are uncorrelated.

Sideband subtracted	$\varepsilon(\pi\pi\pi)$	$\frac{\varepsilon(\pi\pi\pi)}{\varepsilon(K\pi\pi)}$
central value: with σ	0.002659	0.8673
vary $\pi\pi\pi$: no σ	0.002668	0.8701
Relative uncertainty (%)	0.33	

Table 9.5: Systematic uncertainty assigned to $D^+ \rightarrow \pi^- \pi^+ \pi^+$ Dalitz structure modeling.

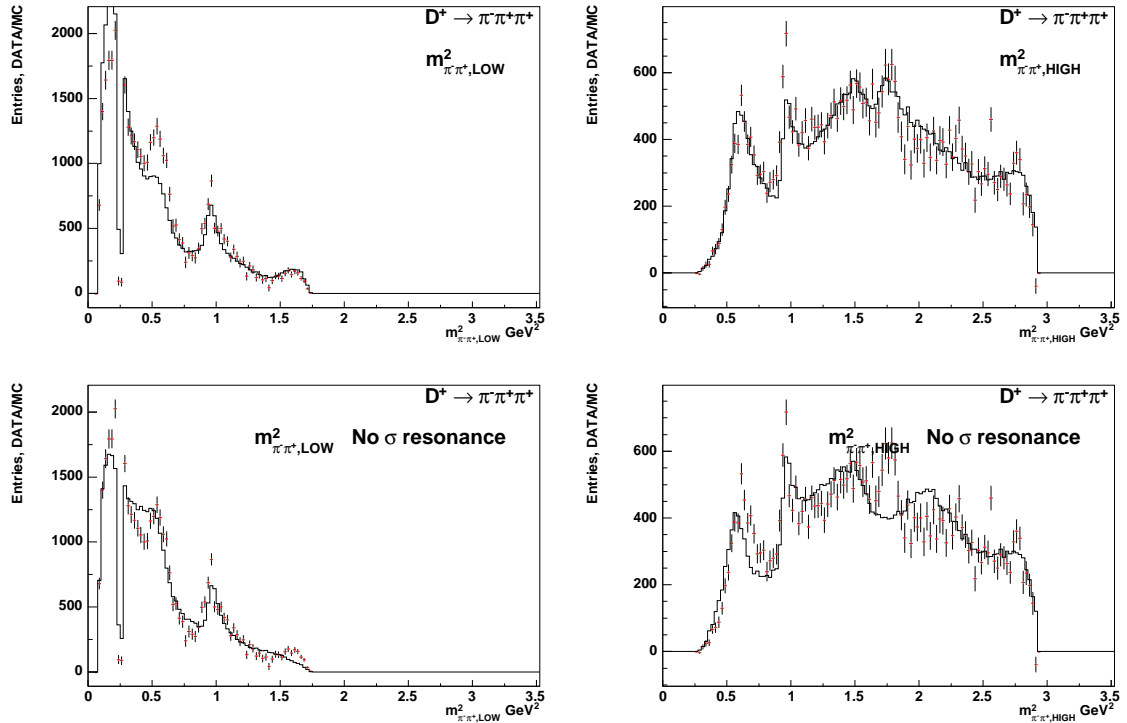


Figure 9.6: Invariant mass projections of Dalitz plots of the $D^+ \rightarrow \pi^- \pi^+ \pi^+$ decay for central value (top) and the assigned systematic uncertainty (bottom). Shown is the agreement between data and Monte Carlo. The latter is generated flat and reweighted using E791 resonances fitted to the data.

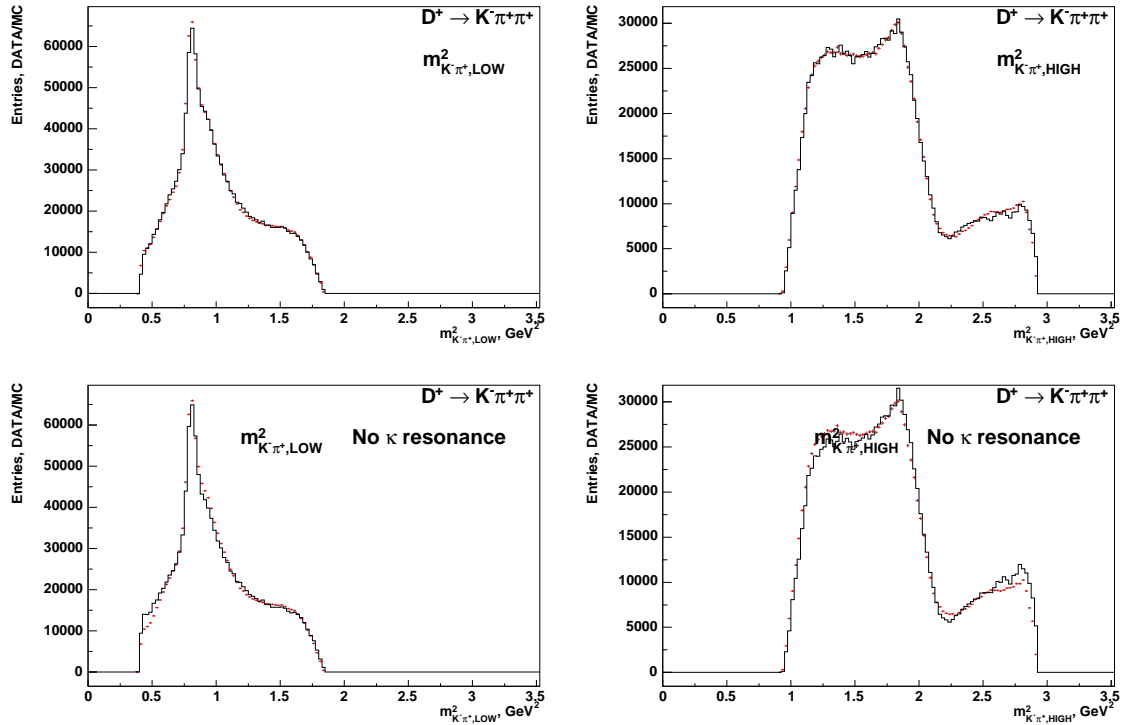


Figure 9.7: Invariant mass projections of Dalitz plots of the $D^+ \rightarrow K^- \pi^+ \pi^+$ decay for central value (top) and the assigned systematic uncertainty (bottom). Shown is the agreement between data and Monte Carlo. The latter is generated flat and reweighted using E791 resonances fitted to the data.

Sideband subtracted	$\varepsilon(K\pi\pi)$	$\frac{\varepsilon(\pi\pi\pi)}{\varepsilon(K\pi\pi)}$
central value: with κ	0.003066	0.8673
vary $K\pi\pi$: no κ	0.003049	0.8722
Relative uncertainty (%)	0.56	

Table 9.6: Systematic uncertainty assigned to $D^+ \rightarrow K^-\pi^+\pi^+$ Dalitz structure modeling.

9.6.2 XFT Efficiency Correction: Sideband Subtraction Uncertainty

In Section 9.3, we described the procedure by which we correct the Monte Carlo for the discrepancy with respect to the data, regarding XFT efficiency of the kaon and pion tracks in comparison with the data. When deriving the parameters for the “hit and miss” Monte Carlo reweighting procedure, we studied the K and π efficiency distributions as they depend on E_{loss} variable. These efficiencies were sideband subtracted in the manner used throughout this analysis: both left and right sidebands are used, each between 3 and 7 σ away from the mass peak. However, the reflections in this region make the sidebands slightly asymmetric, hence this procedure may introduce an asymmetry in the way we treat the K and π tracks and, by implication, the $K\pi\pi$ and $\pi\pi\pi$ decays of the D^+ . To estimate the size of this effect, we perform the E_{loss} fit on the efficiency distributions after subtracting only left or only right sideband. As the Table 9.7 shows, the effect is very small.

9.6.3 XFT Efficiency Correction: Fit Choice Uncertainty

When reweighting the Monte Carlo to correct for XFT efficiencies of kaons and pions, we analyze the efficiency distributions as a function of E_{loss} , and choose the fitting

XFT weight sideband subtraction	$\frac{\varepsilon(\pi\pi\pi)}{\varepsilon(K\pi\pi)}$
central value: both	0.8673
left only	0.8696
right only	0.865
Relative uncertainty (%)	0.26

Table 9.7: Systematic uncertainty associated with correcting XFT efficiencies of tracks: sideband subtraction is performed using left or right sideband, not both as in the rest of the analysis.

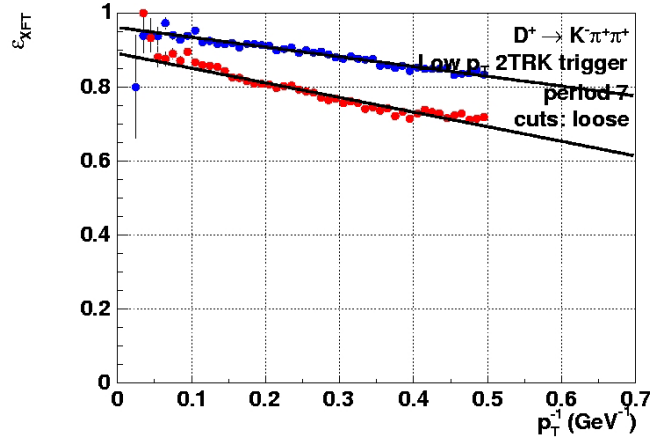


Figure 9.8: Pion and kaon XFT efficiency fitted as a function of p_T^{-1} (only period 7 shown; other periods are similar), as an estimate of systematic uncertainty of Monte Carlo XFT efficiency reweighting.

function accordingly. Doing so introduces an uncertainty regarding our choice of fit variable and function. To estimate this uncertainty, we perform the procedure again, this time fitting the efficiencies as a function of p_T^{-1} . An example is shown in Figure 9.8 for the period 7. The effect is described in Table 9.8.

XFT reweighting model	$\frac{\varepsilon(\pi\pi\pi)}{\varepsilon(K\pi\pi)}$
central value: E_{loss}	0.8673
p_T^{-1} fit	0.8652
Relative uncertainty (%)	0.24

Table 9.8: Systematic uncertainty associated with the choice of procedure for correcting XFT efficiencies of tracks.

9.6.4 $P_T(D^+)$ Spectrum Correction Uncertainty

The Monte Carlo $p_T(D)$ spectra of the two channels differ in that, even after correcting for the data/Monte Carlo discrepancy using the large sample $K\pi\pi$ channel (Section 9.5), the $\pi\pi\pi$ data spectrum still has higher p_T than the $\pi\pi\pi$ Monte Carlo. This warrants the introduction of another systematic uncertainty. To estimate it, we derive the same functional correction as for the central value of the measurement, but this time using the $\pi\pi\pi$ channel. We apply the results of the fit, shown in Figure 9.10, as weights to the Monte Carlo $p_T(D^+)$ spectrum, bin by bin (Figure 9.9). The efficiency drops by 0.32% when compared to the case of no correction (Table 9.9). We take this value as a systematic uncertainty of our result.

$p_T(D)$ correction	$\frac{\varepsilon(\pi\pi\pi)}{\varepsilon(K\pi\pi)}$
No correction	0.8687
central value: $K\pi\pi$ derived	0.8673
$\pi\pi\pi$ derived	0.8659
Relative uncertainty (%)	0.32

Table 9.9: Systematic uncertainty associated with the different Monte Carlo $p_T(D)$ spectra corrections.

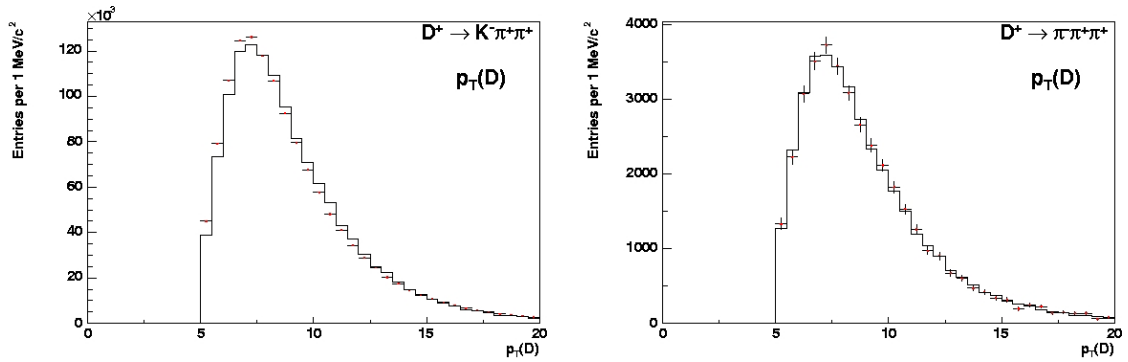


Figure 9.9: Data - Monte Carlo comparison of transverse momentum of the D^+ in $K^-\pi^+\pi^+$ (left) and $\pi^-\pi^+\pi^+$ (right) decays, after applying the $\pi\pi\pi$ -derived correction to estimate the systematic uncertainty.

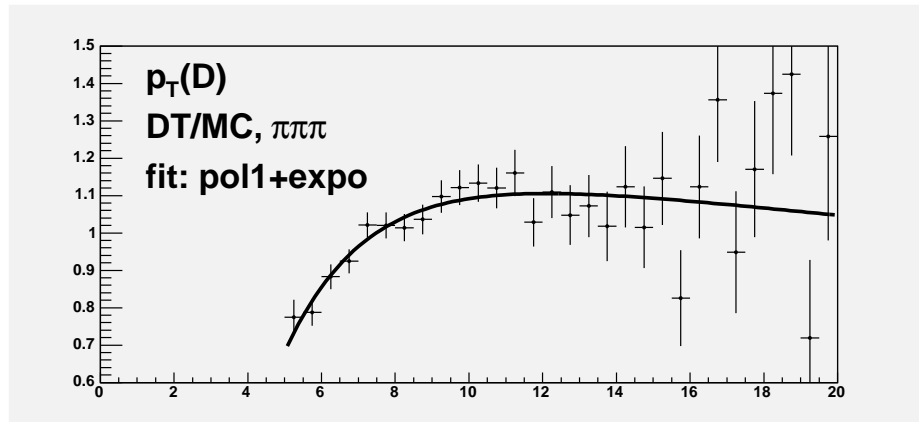


Figure 9.10: Ratio of data and Monte Carlo p_T spectra of the D meson, as derived from $D^+ \rightarrow \pi^-\pi^+\pi^+$ decay, and fitted to an exponential plus a first order polynomial. This is then used to assign an uncertainty.

9.6.5 D^+ Lifetime Uncertainty

The best available D^+ lifetime measurement, $c\tau = 311.8 \pm 2.1\mu m$, which we use to correct the outdated D^+ lifetime value used by the BGenerator, carries an uncertainty of $2.1\mu m$. To estimate the corresponding uncertainty of our relative efficiency result, we measure the efficiency using $c\tau = 311.8 - 2.1\mu m$ and $c\tau = 311.8 + 2.1\mu m$. We assign the mean deviation from the central value as the tiny systematic error (Table 9.10).

D lifetime correction	$\frac{\varepsilon(\pi\pi\pi)}{\varepsilon(K\pi\pi)}$
central value: $c\tau = 311.8\mu m$	0.8673
$c\tau = (311.8 - 2.1)\mu m$	0.8678
$c\tau = (311.8 + 2.1)\mu m$	0.8668
Relative uncertainty (%)	0.06

Table 9.10: Systematic uncertainty associated with the uncertainty on D^+ lifetime

9.6.6 Uncertainty on Hadronic Interactions in the Detector Material

Sometimes a final state particle interacts with the detector material before exiting the tracker, in which case its reconstruction is not possible. The probability for this to happen is about 5% for hadrons. However, this probability differs between pions and kaons and between positively and negatively charged particles, and it depends on the momentum of the hadrons.

The interactions of the final state particles are simulated in the full detector simulation, and are thus accounted for in the relative efficiency. However, both the amount of material in the CDF tracking volume and the hadronic cross-sections have associated uncertainties.

We estimate that the amount of material in the tracking volume is simulated with 20% of uncertainty, whereas hadronic interaction cross sections are known with 15% error. This implies that the hadronic interactions with the detector material carry a total uncertainty of 25% of their value.

To determine the hadronic interaction probability in the Monte Carlo, we perform full detector simulations of single particle events of π^+ , π^- , K^+ , K^- . For each of the four meson types, we simulate 2,000,000 events with transverse momentum between 0.3 and 20.0 GeV/ c , and pseudo-rapidity between -1.5 and 1.5 . The requirements on the tracks known to the GEANT detector simulation are the same as the requirement on the charm daughters; they need to traverse the active volumes of the silicon and the central trackers. We use the same software as in the full detector simulation of the charm mesons.

Figure 9.12 shows the probabilities of a hadronic interaction of the mesons as they depend on the track transverse momentum. We observe that the GEANT simulation reproduces the known effects of hadron interactions in matter. In particular, while the interaction probability is similar for the negative and the positive pions, the K^+ has a significantly smaller probability to interact with matter than the K^- .

For each charm daughter, we determine the average interaction probability by weighting the particle interaction probability with the measured p_T spectrum of its species (Figure 9.11); the charm daughters' spectra are ordered so that the first particle is, as usual, the oppositely charged hadron, and the second one forms larger invariant mass with the first than does the third. Because the latter two charm daughters are always of the same species, this requirement essentially means that we order the latter two tracks by p_T . The averaged interaction probabilities are shown in Table 9.11. Also shown are the corresponding total efficiencies, that is, probabilities

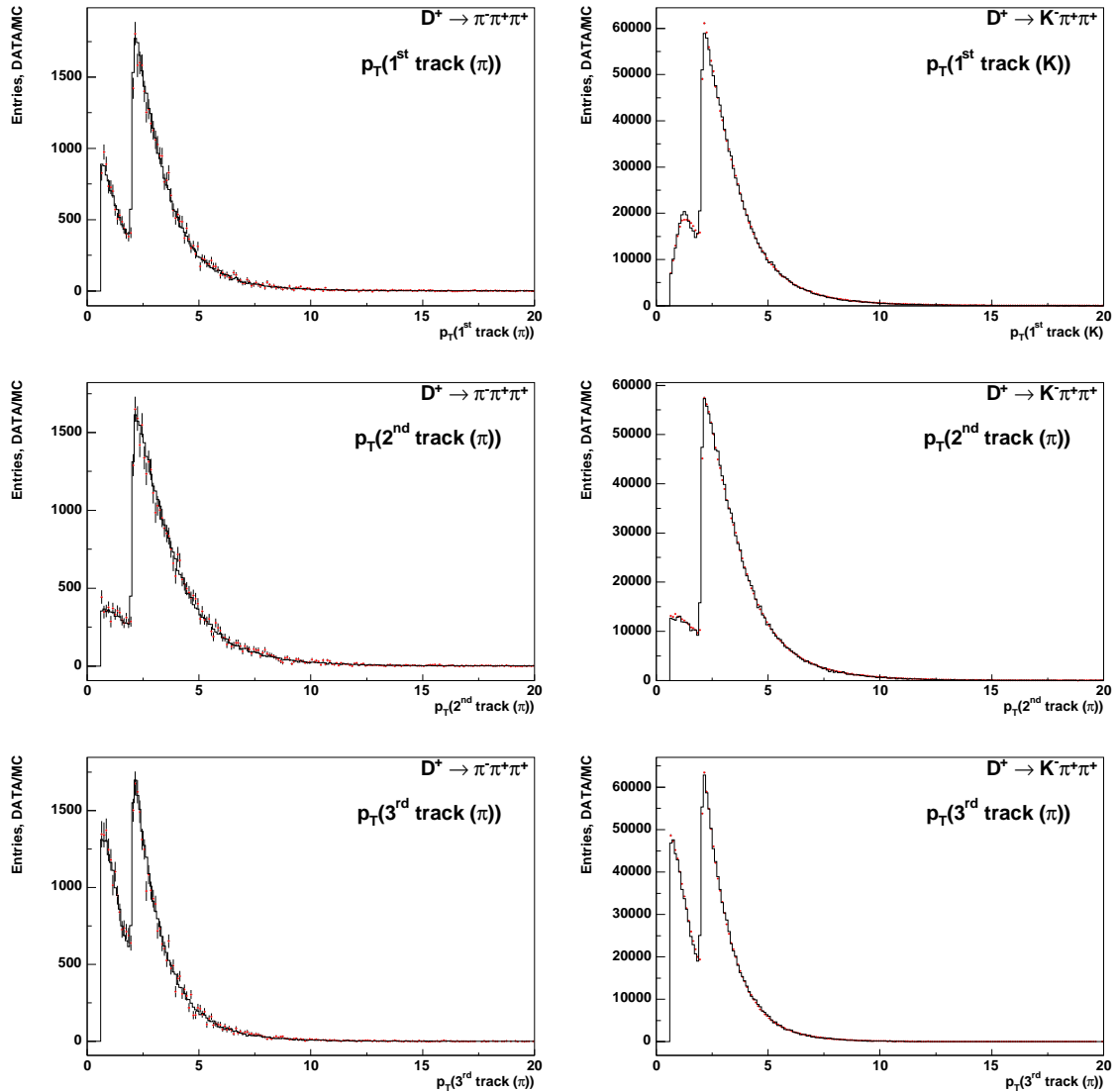


Figure 9.11: Overlay of data and Monte Carlo p_T spectra of the D^+ daughter tracks. $D^+ \rightarrow K^- \pi^+ \pi^+$ plots are on the left and $D^+ \rightarrow \pi^- \pi^+ \pi^+$ on the right. Track 1 corresponds to the track of the charge opposite to that of the D^+ meson. Track 2 and 3 are ordered such that $m_{12} > m_{13}$.

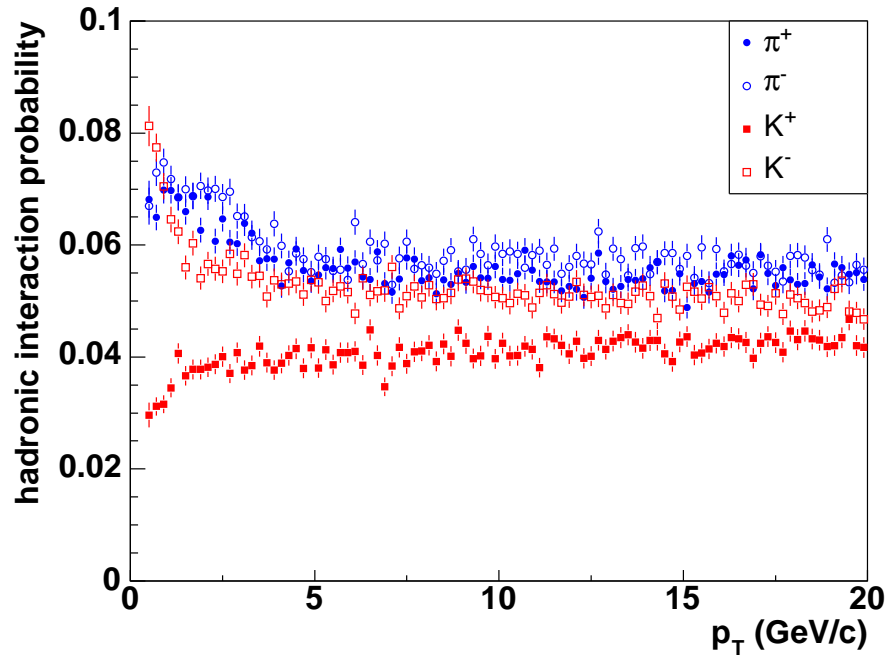


Figure 9.12: Hadronic interaction probabilities using simulated single particle events.

	$D^+ \rightarrow K^- \pi^+ \pi^+$	$D^- \rightarrow K^+ \pi^- \pi^-$	$D^+ \rightarrow \pi^- \pi^+ \pi^+$	$D^- \rightarrow \pi^+ \pi^- \pi^-$
track 1	0.055958	0.038758	0.065771	0.062009
track 2	0.060819	0.064437	0.060526	0.064034
track 3	0.063302	0.067280	0.063110	0.066986
eff(D)	0.830500	0.838797	0.822293	0.819119
eff(D)	0.834649		0.820706	

Table 9.11: Probability of charm daughters to undergo hadronic interactions inside the tracking volume (first three rows) and efficiency for not having any of the three daughters interact (last two rows)

to have none of the three charm daughters interacting.

We find that the relative difference in the efficiency due to hadronic interactions between the $K\pi\pi$ and $\pi\pi\pi$ mode is 1.70%. Assigning 20% of this value to the uncertainty on the amount of material in the tracking volume and 15% to the uncertainty on the hadronic interaction cross-sections, we estimate the systematic uncertainty on the $\pi\pi\pi$ to $K\pi\pi$ relative efficiency from material interactions to be 0.43%.

9.6.7 Systematic Uncertainties: Summary

We arrive at the relative reconstruction efficiency of $D^+ \rightarrow \pi^- \pi^+ \pi^+$ to $D^+ \rightarrow K^- \pi^+ \pi^+$ of 0.8673 ± 0.0083 .

Table 9.12 summarizes the systematic uncertainties we considered in this measurement.

Uncertainty source	Assigned error (%)
$N_{\pi\pi\pi}/N_{K\pi\pi}$	
Radiative tail	0.67
Width parameter treatment	0.03
Total, signal extraction	0.67
$\frac{\varepsilon(\pi\pi\pi)}{\varepsilon(K\pi\pi)}$	
$\pi\pi\pi$ Dalitz structure	0.33
$K\pi\pi$ Dalitz structure	0.56
XFT efficiency, fit variable	0.24
XFT efficiency, sideband subtraction	0.26
p_T spectra rescaling	0.32
D^+ lifetime	0.06
material interactions	0.43
Monte Carlo sample size	0.26
Total, relative efficiency	0.96
ALL	1.17

Table 9.12: Summary of the relative systematic uncertainties.

Chapter 10

Result and Conclusions

Combining the event yields, $N_{\pi\pi\pi}/N_{K\pi\pi} = (3.002 \pm 0.033 \pm 0.020)\%$, and the relative efficiency, $\frac{\varepsilon(\pi\pi\pi)}{\varepsilon(K\pi\pi)} = 0.8673 \pm 0.0083$, we find the branching ratio of $D^+ \rightarrow \pi^-\pi^+\pi^+$ versus $D^+ \rightarrow K^-\pi^+\pi^+$ to be:

$$\frac{BR(D^+ \rightarrow \pi^-\pi^+\pi^+)}{BR(D^+ \rightarrow K^-\pi^+\pi^+)} = (3.461 \pm 0.038(stat) \pm 0.040(syst))\%. \quad (10.1)$$

This result agrees with the present world average, $(3.48 \pm 0.19)\%$ [8], and is about three times more precise than the most precise measurement to date, $(3.52 \pm 0.11 \pm 0.12)\%$ [6], performed by CLEO-c.

Using the world average of the absolute branching ratio of the $D^+ \rightarrow K^-\pi^+\pi^+$, $(9.51 \pm 0.34)\%$ [8] we find $BR(D^+ \rightarrow \pi^-\pi^+\pi^+) = (3.29 \pm 0.11) \times 10^{-3}$.

The most straightforward way to improve this measurement would be to increase the amount of data. The sample size we used is small, at least compared to the amount of data presently available for CDF physics analyses. However, the systematic and

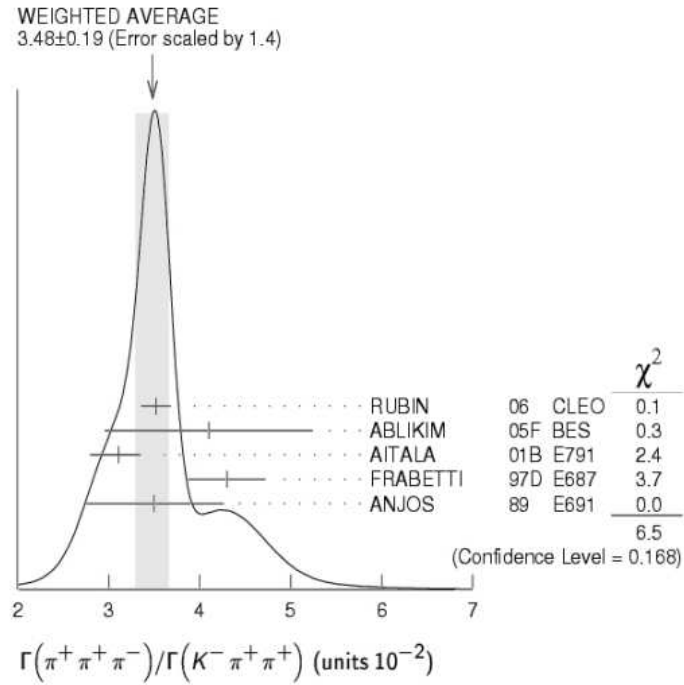


Figure 10.1: PDG plot comparing measurements of $\frac{BR(D^+ \rightarrow \pi^- \pi^+ \pi^+)}{BR(D^+ \rightarrow K^- \pi^+ \pi^+)}$ performed by several collaborations.

the statistical errors are of roughly the same size. Therefore, increased amount of data would improve the precision to a certain degree, at which point the error would be dominated by systematic uncertainties.

The leading systematic uncertainty is the one we assigned to the shape of the signal peaks' radiative tails. To estimate it, we varied the size of the tails, as they are generated by the BGenerator using the PHOTOS package. Increasing the signal sample size would help with this only if the tail was relatively extreme in size. The reason is that the tail region is also populated with the D_s^+ misreconstructed decays, and distinguishing between the two would be extremely difficult even with significantly more data. On the other hand, should the description of the final state radiation in PHOTOS improve for hadronic decays, or even better, should the amount of material in the CDF detector become known with better precision, it would be possible to improve this result and reduce its main systematic error.

The second largest systematic uncertainty comes from our modeling of the $D^+ \rightarrow K^- \pi^+ \pi^+$ Dalitz structure; the $D^+ \rightarrow \pi^- \pi^+ \pi^+$ Dalitz structure also contributes significantly and takes the fourth largest place among the systematic uncertainties. We used the results of another experiment to fit our data and correct the Monte Carlo. We estimated errors by implementing the same procedure, but using a different set of Dalitz models proposed by the same E791 studies. Clearly, performing the full Dalitz analysis of our data would improve our result, but would also require substantial work. We leave this task to other members of the CDF collaboration.

The third largest systematic uncertainty is that of the hadronic interactions with the detector material. Here, too, larger amount of data would not be of help. This uncertainty has two components: the amount of material in the tracking volume of the material, and the hadronic interactions cross sections. Improvement in the GEANT

description of our detector, as well as in the hadronic interactions cross sections, would result in better precision four measurement.

Nevertheless, as Figure 10.1 shows, this is by far the best measurement to date of the relative branching fraction of $D^+ \rightarrow \pi^- \pi^+ \pi^+$ with respect to $D^+ \rightarrow K^- \pi^+ \pi^+$. In addition to being a good measurement in its own right, by providing tools and understanding of the signal, background, and efficiency issues, this work opens the door for CDF collaboration to measure the CP asymmetry in the $D^+ \rightarrow \pi^- \pi^+ \pi^+$ channel. Looking for CP violation within the resonant decays of the $D^+ \rightarrow \pi^- \pi^+ \pi^+$ would be interesting, and would hold added potential in comparison with studying the decay as a whole. The standard model predicts a CP violation effect of the order of 10^{-3} - 10^{-2} [5]. Finding a CP asymmetry of this size would add to our knowledge of the charm sector and to our confidence in the current understanding of the charm phenomenology.

More interestingly, finding an asymmetry higher than that predicted by the standard model would indicate new physics phenomena, unaccounted for by the standard model. At this point of the particle physics history, new physics phenomena are expected to be found soon, most likely by the experiments at the Large Hadron Collider. The Large Hadron Collider is expected to deliver 1 fb^{-1} of data within the first year of operation (in comparison, it took Tevatron almost 4 years to do this), and it is scheduled to start operating in the second half of 2008. Meanwhile, the experiments at the Tevatron are racing to analyze the data collected over the years and complete their contributions to the exploration of the standard model and beyond.

Bibliography

- [1] A.D. Sakharov. Violation of cp invariance, c asymmetry, and baryon asymmetry of the universe. *JETP Lett.*, 5:24–27, 1967.
- [2] K. Niu, E. Mikumo, and Y. Maeda. *Prog. Theor. Phys.*, 46:1644, 1971.
- [3] J. J. Aubert et al. Experimental observation of a heavy particle j. *Phys. Rev. Lett.*, 33:1404–1406, 1974.
- [4] G. S. Abrams et al. The discovery of a second narrow resonance in e+ e- annihilation. *Phys. Rev. Lett.*, 33:1453–1455, 1974.
- [5] S. Bianco, F. L. Fabbri, D. Benson, and I. Bigi. A cicerone for the physics of charm. *Riv. Nuovo Cim.*, 26N7:1–200, 2003, hep-ex/0309021.
- [6] P. Rubin et al. New measurements of cabibbo-suppressed decays of d mesons in cleo-c. *Phys. Rev. Lett.*, 96:081802, 2006, hep-ex/0512063.
- [7] E. M. Aitala et al. Experimental evidence for a light and broad scalar resonance in $D^+ \rightarrow \pi^- \pi^+ \pi^+$ decay. *Phys. Rev. Lett.*, 86:770–774, 2001, hep-ex/0007028.
- [8] Yao, W.-M. and others. Review of Particle Physics. *Journal of Physics G*, 33:1, 2006.
- [9] S. L. Glashow. Partial symmetries of weak interactions. *Nucl. Phys.*, 22:579–588, 1961.
- [10] Steven Weinberg. A model of leptons. *Phys. Rev. Lett.*, 19:1264–1266, 1967.
- [11] Abdus Salam. Weak and electromagnetic interactions. 1968. Originally printed in *Svartholm: Elementary Particle Theory, Proceedings Of The Nobel Symposium Held 1968 At Lerum, Sweden*, Stockholm 1968, 367-377.
- [12] Steven Weinberg. Physical processes in a convergent theory of the weak and electromagnetic interactions. *Phys. Rev. Lett.*, 27(24):1688–1691, Dec 1971.

BIBLIOGRAPHY

- [13] S. W. Herb, D. C. Hom, L. M. Lederman, J. C. Sens, H. D. Snyder, J. K. Yoh, J. A. Appel, B. C. Brown, C. N. Brown, W. R. Innes, K. Ueno, T. Yamanouchi, A. S. Ito, H. Jöstlein, D. M. Kaplan, and R. D. Kephart. Observation of a dimuon resonance at 9.5 gev in 400-gev proton-nucleus collisions. *Phys. Rev. Lett.*, 39(5):252–255, Aug 1977.
- [14] F. Abe, H. Akimoto, A. Akopian, M. G. Albrow, S. R. Amendolia, D. Amidei, J. Antos, C. Anway-Wiese, S. Aota, G. Apollinari, T. Asakawa, W. Ashmanskas, M. Atac, P. Auchincloss, F. Azfar, P. Azzi-Bacchetta, N. Bacchetta, W. Badgett, S. Bagdasarov, M. W. Bailey, J. Bao, P. de Barbaro, A. Barbaro-Galtieri, V. E. Barnes, B. A. Barnett, P. Bartalini, and G. Bauer. Observation of top quark production in $p\bar{p}$ collisions with the collider detector at fermilab. *Phys. Rev. Lett.*, 74(14):2626–2631, Apr 1995.
- [15] S. Abachi, B. Abbott, M. Abolins, B. S. Acharya, I. Adam, D. L. Adams, M. Adams, S. Ahn, H. Aihara, J. Alitti, G. Álvarez, G. A. Alves, E. Amidi, N. Amos, E. W. Anderson, S. H. Aronson, R. Astur, R. E. Avery, A. Baden, V. Balamurali, J. Balderston, B. Baldin, J. Bantly, J. F. Bartlett, K. Bazizi, J. Bendich, and S. B. Beri. Observation of the top quark. *Phys. Rev. Lett.*, 74(14):2632–2637, Apr 1995.
- [16] M. L. Perl, G. S. Abrams, A. M. Boyarski, M. Breidenbach, D. D. Briggs, F. Bulos, W. Chinowsky, J. T. Dakin, G. J. Feldman, C. E. Friedberg, D. Fryberger, G. Goldhaber, G. Hanson, F. B. Heile, B. Jean-Marie, J. A. Kadyk, R. R. Larsen, A. M. Litke, D. Lüke, B. A. Lulu, V. Lüth, D. Lyon, C. C. Morehouse, J. M. Paterson, F. M. Pierre, T. P. Pun, and P. A. Rapidis. Evidence for anomalous lepton production in $e^+ - e^-$ annihilation. *Phys. Rev. Lett.*, 35(22):1489–1492, Dec 1975.
- [17] G. Arnison et al. Experimental observation of isolated large transverse energy electrons with associated missing energy at $\sqrt{s} = 540$ gev. *Phys. Lett.*, B122:103–116, 1983.
- [18] M. Banner et al. Observation of single isolated electrons of high transverse momentum in events with missing transverse energy at the cern anti-p p collider. *Phys. Lett.*, B122:476–485, 1983.
- [19] G. Arnison et al. Experimental observation of lepton pairs of invariant mass around 95 gev/ c^2 at the cern sps collider. *Phys. Lett.*, B126:398–410, 1983.
- [20] P. Bagnaia et al. Evidence for $z^0 \rightarrow e^+e^-$ at the cern anti-p p collider. *Phys. Lett.*, B129:130–140, 1983.

BIBLIOGRAPHY

- [21] CDF Collaboration. The CDF II detector: Technical design report. 1999. FERMILAB-Pub-96/390-E.
- [22] L. Balka. The CDF central electromagnetic calorimeter. *Nucl. Instrum. Methods. Phys. Res., Sect. A*, 267:271, 1988.
- [23] L. Balka. The CDF central and endwall hadron calorimeter. *Nucl. Instrum. Methods. Phys. Res., Sect. A*, 267:301, 1988.
- [24] H. Frisch et al. Conceptual design of a deadtimeless trigger for the CDF trigger upgrade. *CDF Note*, 2038, 1994.
- [25] E. Thomson et al. Online track processor for the CDF upgrade. *IEEE Transactions on Nuclear Science*, 49(3), 2002.
- [26] W. Badgett. The CDF Run II Run Database and Online Java API. *CDF Note*, 5672, 2001, CDF/DOC/ONLINE/PUBLIC/5672.
- [27] K. Anikeev, P. Murat, and Ch. Paus. Description of BGenerator II. *CDF Note*, 5092, 1999, CDF/PHYS/BOTTOM/CDFR/5092.
- [28] C. Peterson, D. Schlatter, I. Schmitt, and Peter M. Zerwas. Scaling violations in inclusive e^+e^- annihilation spectra. *Phys. Rev.*, D27:105, 1983.
- [29] D. J. Lange. The evtgen particle decay simulation package. *Nucl. Instrum. Meth.*, A462:152–155, 2001.
- [30] R. Brun et al. Geant: Simulation program for particle physics experiments. 1978. CERN-DD-78-2-REV, CERN-DD-78-2.
- [31] J. C. Anjos et al. A Dalitz plot analysis of $D \rightarrow K\pi\pi$ decays. *Phys. Rev.*, D48:56–62, 1993.
- [32] E. M. Aitala et al. Dalitz plot analysis of the decay $D^+ \rightarrow K^-\pi^+\pi^+$ and study of the $K\pi$ scalar amplitudes. *Phys. Rev. Lett.*, 89:121801, 2002, hep-ex/0204018.
- [33] A. Cerri and R. Miquel. Studying the SVT Efficiency and Resolution with J/Ψ Data. *CDF Note*, 5838, 2002, CDF/DOC/TRIGGER/CDFR/5092.
- [34] S. Dobbs et al. Measurement of absolute hadronic branching fractions of D mesons and $e^+e^- \rightarrow D\bar{D}$ cross sections at the $\psi(3770)$. *Phys. Rev.*, D76:112001, 2007.
- [35] E. Baracchini and G. Isidori. Electromagnetic corrections to non-leptonic two-body B and D decays. *Phys. Lett.*, B633:309–313, 2006.